Signal Integrity Challenges and Solutions at Cryogenic Temperatures

by

Bhargav Yelamanchili

A dissertation submitted to the Graduate Faculty of
Auburn University
in partial fulfillment of the
requirements for the Degree of
Doctor of Philosophy

Auburn, Alabama
August 5, 2023

Keywords: Superconductor, resonators, signal integrity, interconnect, irradiation, quantum

Approved by

Michael C. Hamilton, Chair, James B. Davis Professor of Electrical and Computer Engineering
Mark L. Adams, Associate Professor of Electrical and Computer Engineering
Masoud Mahjouri-Samani, Assistant Professor of Electrical and Computer Engineering
Minseo Park, Professor of Physics
Wencan Jin, Assistant Professor of Physics

Abstract

The field of electronics is rapidly evolving and expanding into new frontiers, including cryogenic environments. Cryogenic temperatures below 10 K have become increasingly important in various applications such as quantum computing, superconducting electronics, and space exploration. However, the unique physical properties of materials at these extremely low temperatures present significant challenges for signal integrity in electronic systems.

The dissertation addresses critical signal integrity challenges encountered in the transmission of high-speed digital signals in extremely low-temperature environments. The initial research focuses on the design and implementation of a face-to-face cable connection scheme using flexible thin-film superconducting stripline cables. The work encompasses the mitigation of signal integrity issues, including impedance discontinuities, crosstalk, signal loss, and power dependency. Through extensive simulations using Ansys HFSS and Keysight PathWave ADS and experimental measurements, the dissertation presents an effective interconnect scheme for cryogenic and quantum technology applications. The findings contribute to the advancement of dense signal integration, ensuring reliable and efficient signal transmission in demanding low-temperature environments. The insights gained from this research provide a foundation for the development of robust signal pathways and hold significance for the design and optimization of future cryogenic systems and quantum technologies.

This dissertation also investigates signal integrity challenges at cryogenic temperatures, with a specific focus on the impact of gamma radiation on superconducting microstrip resonators. The work explores the behavior of Nb and Al/Nb/Al embedded resonators before and after exposure to gamma radiation, quantifying changes in their quality factor (Q) values. The Q values of the resonators were extracted and compared at various cryogenic temperatures below 4.2 K after one and four weeks of gamma radiation corresponding to

152 kGy and 608 kGy, respectively. The findings reveal the resilience of these resonators to radiation, with minimal degradation observed in the dielectric loss tangent values.

The research also focused on utilizing very long resonators to characterize material losses and optimize fabrication procedures for superconducting structures for quantum applications. By employing these resonators, a detailed analysis of losses at different frequencies is achieved, enabling the identification of the most suitable fabrication techniques for quantum computation applications. The work addresses signal integrity challenges by investigating losses and frequency-dependent behaviors of superconducting structures. The Q values as high as 1.2 million were measured. Through rigorous measurements and analysis, this research contributes to the understanding and mitigation of signal integrity issues at cryogenic temperatures, paving the way for the development of more efficient and reliable systems for quantum computation.

The experimental investigation is a crucial aspect of this research, as it allows for the validation of theoretical and simulation results and provides insight into the effectiveness of proposed solutions. The results of this research contribute to the development of reliable electronic systems for cryogenic applications. The proposed solutions include the use of special low-temperature cables and connectors to minimize signal attenuation and noise and the selection of appropriate materials with low loss tangent and high thermal conductivity. These solutions are demonstrated through experimental validation and simulation, providing a basis for their application in real-world electronic systems.

Acknowledgments

First and foremost, I am extremely grateful to my academic advisor Dr. Michael C. Hamilton for his invaluable advice, continuous assistance, financial support, and patience during my Ph.D. study and research at Auburn University. He has consistently given me the proper amount of inspiration and zeal, which has aided my success, commitment to hard work, and personal development.

I am extremely grateful to my dissertation committee: Dr. Mark L. Adams, Dr. Masoud Mahjouri-Samani, and Dr. Minseo Park for their helpful feedback on my dissertation. I also extend my sincere thanks to Dr. Wencan Jin for serving as University Reader for my Ph.D. work. Their opinions and suggestions are incredibly insightful and beneficial.

The completion of this work could not have been achieved without the support of our laboratory manager, John A. Sellers. His knowledge and great experience have encouraged me in all the time of my academic research and daily life.

I would especially like to thank Dr. David B. Tuckerman and Microsoft Research for their financial and technical help.

I am also grateful to Dr. Vaibhav Gupta for being a friend, a mentor, and a guiding hand throughout my Ph.D. career.

I would like to thank my fellow lab mates and friends, Sherman Peek, Archit Shah, Stephen Bankson, Harshil Goyal, Dr. Uday Goteti, and Dr. Simin Zou for their assistance and discussions on various scholarly topics.

I also would like to acknowledge the help that I received from undergraduate students, Chase Tillman, Jacob Ward, and Grant Gleason.

I would like to acknowledge the Alabama Micro/Nano Science and Technology Center (AMNSTC) for providing access to fabrication and characterization facilities used in this work.

I would like to thank my parents Venkata Ramana Rao Yelamanchili and Krishna Kumari Yelamanchili, my brother Dheeraj Sai Yelamanchili, and my dearest friend Vani Madhuri for their love and support, especially within my last three months of graduate studies. Without them, this day would not have been possible.

Table of Contents

List of Figures

List of Tables

List of Abbreviations

$(\mu_{en}/\rho)_{air}$ Mass energy-absorption coefficient of air

$(\mu_{en}/\rho)_{material}$ Mass energy-absorption coefficient of material

ϵ_0 Permittivity of free space

λ_L London Penetration Depth

μ_0 Permeability of free space

ω_p Plasma frequency

σ_0 DC conductivity

τ Mean collision time

B_{c1} Lower critical magnetic field

B_{c2} Higher critical magnetic field

C_c Contact pad capacitance

D_{air} Dose rate to air

$D_{material}$ Dose rate to material

L_k Kinetic inductance

n_n Classical electrons

n_s Superconductive electrons

Q_c Q-factor associated with conductor loss

Q_d Q-factor associated with dielectric loss

Q_l Loaded quality factor

Q_r Q-factor associated with radiation loss

$Q_{coupling}$ Q-factor associated with radiation loss

R_c Contact resistance

ϵ_r Relative permittivity

ADS Advance Design System

BCS Bardeen Cooper Schrieffer

CNC Computerized Numerical Control

CPW Coplanar waveguide

CT Connector tester

DC Direct current

EM Electromagnetic

HAR High aspect ratio

HFSS High Frequency Structure Simulator

Ic Critical Current

I/O Input Output

LB Loop-back

LHe Liquid helium

PI Ploymide

PLTS Physical Layer Test System

PNA Performance Network Analyzer

Q Quality factor

RCA Radio Corporation of America

SEM Scanning electron microscope

SFQ Single Flux Quantum

SMA Subminiature version A

SNP S-parameters for N-port networks

Tc Critical Temperature

TDR Time domain reflectometry

TLS Two level system

UBM Under bump metal

VtPRBS Voltage source pseudo random bit sequence

Chapter 1

Introduction

1.1 Background and Motivation

Electronic systems have become an integral part of our modern world, enabling advancements in various fields such as communication, sensing, and high-level data computing and analyzing. As technology continues to advance, electronic systems are being pushed to operate under increasingly demanding conditions, including extreme temperatures. Cryogenic temperatures, in particular, have gained significant attention due to their relevance in emerging fields such as quantum computing, superconducting electronics, and space exploration [1, 2, 3, 4, 5, 6].

Cryogenic temperatures, typically below 100 K, present unique challenges for the operation of electronic systems. At such extremely low temperatures, the physical properties of materials undergo substantial changes that affect the behavior of electronic signals. These changes include an increase in the conductivity of metals and changes in dielectric properties in insulators, such as dielectric constant and dissipation factor. These alterations can lead to signal integrity issues, such as impedance mismatches, and changes in signal propagation speed, which can cause signal distortion, reflection of incident signal, crosstalk between adjacent signal lines, and power loss, ultimately impacting the performance and reliability of electronic systems [7, 8, 9].

The motivation behind this dissertation stems from the need to bridge the knowledge gap surrounding signal integrity at cryogenic temperatures, specifically to solve the problem of how to transmit and receive many RF and microwave signals efficiently for cryogenic and quantum applications. Dilution refrigerators have been widely used for cryogenic and quantum applications to provide continuous cooling to temperatures as low as 2 mK, with

no moving parts in the low-temperature region [10, 11, 12]. Dilution refrigerators usually have limited physical volume and cooling capacity for superconducting circuitry and coaxial data cables used to carry electrical signals between different temperature stages. These bulky coaxial cables add to the thermal load and are likely to cause thermal leaks between various temperature stages inside the dilution refrigerator. In recent times, densely integrated superconducting interconnects and connector technologies have been presented to replace coaxial cables [13, 14, 15, 16]. The existing literature provides some insights into the topic, but further investigation is required to explore the unique characteristics and complexities associated with signal propagation and degradation in extreme low-temperature conditions. When these challenges are understood more thoroughly, novel solutions can be developed to mitigate adverse effects on signal quality and enhance the performance of electronic systems in cryogenic environments.

1.2 Superconductors

Superconductors are materials that possess the unique property of zero electrical resistance when cooled below a certain temperature. This remarkable phenomenon was first observed in 1911 by the Dutch physicist Heike Kamerlingh Onnes, who discovered that mercury, when cooled to a temperature of 4.15 K, suddenly lost all electrical resistance [17, 18, 19].

Since then, researchers have discovered many other materials that exhibit superconductivity, including metals, alloys, ceramics, and even some organic compounds. The critical temperature (Tc) at which a material becomes a superconductor varies depending on the specific material, but it is typically very low, ranging from just a few degrees above absolute zero to around 173 K [20].

In a superconductor, an electric current can last forever. The temperature at which the electrical resistance goes to zero is called the critical transition temperature of the superconductor (Fig. 1.1) [21]. The BCS theory, which was developed by John Bardeen, Leon Cooper,

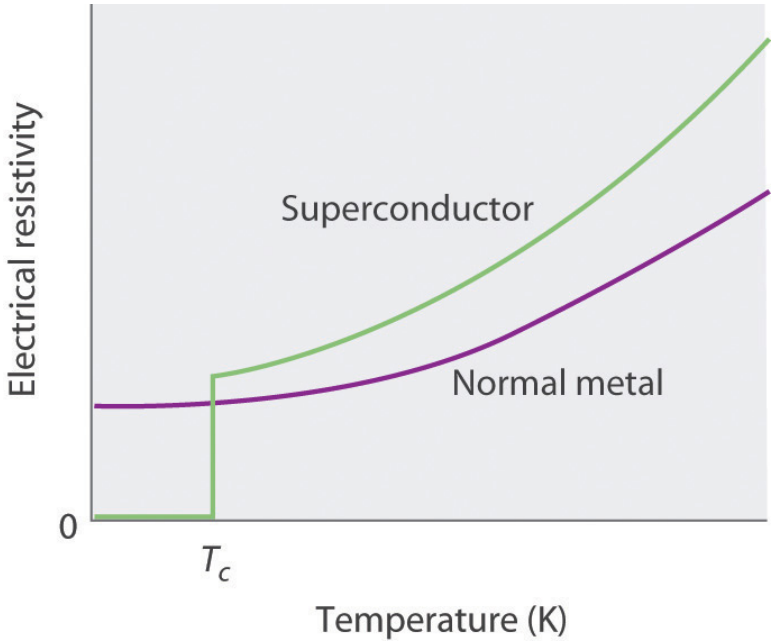

Figure 1.1: The electrical resistivity of a normal metal and a superconductor vs. temperature. Adapted from [21].

and Robert Schrieffer to understand the behavior of a superconducting material, provides a comprehensive explanation for this drastic reduction in resistance.

1.2.1 Types of Superconductors

Superconductors can be broadly classified into two categories: Type I and Type II. The classification is based on the behavior of the superconductor in the presence of a magnetic field [22, 23, 24].

Type I superconductors are characterized by a sudden and complete expulsion of the magnetic field from their interior (the Meissner effect) when cooled below their critical temperature. They have a relatively low critical magnetic field (H_c) strength, above which the superconductivity is destroyed. Type I superconductors are typically pure metals, such as lead, mercury, and aluminum, and exhibit relatively low critical temperatures.

Type II superconductors, on the other hand, can tolerate much stronger magnetic fields before their superconductivity is destroyed. They also exhibit a mixed state in which some of the magnetic fields penetrate into the superconductor, forming quantized vortices. They will

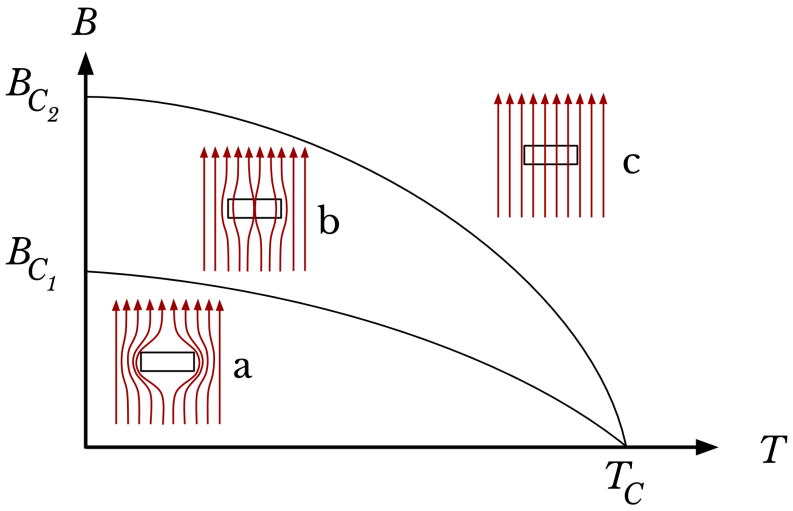

Figure 1.2: Image showing the behavior of type-II superconductor in the presence of an external magnetic field.

start to lose their superconductivity at a lower critical magnetic field (B_{c1}) and at a higher magnetic field (B_{c2}), they will completely lose it as shown in Fig. 1.2. Type II superconductors are typically complex materials such as alloys and ceramics, and have critical temperatures higher than those of Type I superconductors. This is best illustrated by NbN.

The mixed state of Type II superconductors has led to the discovery of many interesting phenomena, such as the formation of Abrikosov vortices, flux pinning, and the flux-flow state. These phenomena have important implications for the potential applications of Type II superconductors, such as in high-field magnets and power transmission lines.

Although both Type I and Type II superconductors have unique properties and applications, the focus of current research is mainly on Type II superconductors because of their higher critical temperatures and potential for practical applications.

1.3 Drude Model

The Drude model is a classical theory that was originally developed to describe the behavior of electrical conductivity in normal metals. It is based on the assumption that the free electrons in a metal are subject to collisions with ions and other electrons, which

cause them to scatter and lose energy. The complex conductivity is a simple result of the classical Drude model and is typically represented as shown in 1.1, where the real part of the conductivity represents the conventional conductive loss and the imaginary part represents the phase velocity and propagation.

$$\widetilde{\sigma(\omega)} = \sigma_{re}(\omega) - i\sigma_{im}(\omega) \tag{1.1}$$

The real and imaginary components of the conductivity for the Drude Model are illustrated below in terms of DC conductivity, σ_0, and mean collision time, τ.

$$\sigma_{re}(\omega) = \frac{\sigma_0}{1+\omega^2\tau^2} \qquad \sigma_{im}(\omega) = \frac{\sigma_0\omega\tau}{1+\omega^2\tau^2} \tag{1.2}$$

The mean collision time of electrons can also be defined in terms of plasma frequency, ω_p, and DC conductivity, σ_0, as shown in equation 1.3, where ϵ_0 is the permittivity of free space.

$$\tau = \frac{\sigma_0}{\omega_p^2\epsilon_0} \tag{1.3}$$

1.4 Generalized Model for Superconductors

In the context of superconductors, the Drude model has been extended to include the effects of superconductivity. In this modified version of the Drude model, the superconducting state is described as a state in which the electrons are able to move freely without any resistance, resulting in zero electrical resistance.

The key to the success of the modified Drude model lies in its ability to account for the coherence of the superconducting state, which is characterized by the formation of Cooper pairs-bound states of two electrons with opposite spins. These pairs are formed due to the

attractive interactions between the electrons, which overcome the repulsive Coulomb interactions.

The modified Drude model for superconductors predicts that the electrical conductivity should exhibit a sudden drop to zero below the critical temperature, as the Cooper pairs begin to condense and form a macroscopic quantum state. The model also predicts that there should be a sharp increase in the heat capacity of the superconductor below the critical temperature, due to the energy required to break up the Cooper pairs.

While the Drude model for superconductors is a simplified model that neglects many of the quantum mechanical effects that are important in real superconductors, it provides a useful starting point for understanding the behavior of superconducting materials and has been the basis for much of the theoretical work in the field of superconductivity.

The common model used to describe the dispersive electrical effects of a superconductor derives itself from this '2 body fluid' model discriminating the electrons as such. This model also represents the electrical effects of a superconductor with a complex conductivity that is a function of temperature and frequency. If the temperature is above the critical temperature, it will behave as the classical conductor, whether a semiconductor or metal. If the temperature is equal to or below the critical temperature, the behavior changes markedly to demonstrate many of the classical superconducting effects. For the 2-fluid superconductor model, the complex conductivity is as shown below:

$$\sigma_{re} = \frac{n_n}{n_s}\frac{\tau}{\Lambda}[\frac{1}{1+\omega^2\tau^2}] \qquad \sigma_{im} = \frac{1}{\Lambda\omega}[1+\frac{n_n}{n_s}\frac{\omega^2\tau^2}{1+\omega^2\tau^2}] \tag{1.4}$$

where n_n/n_s is the ratio of classical electrons to superconductive electrons and is a function of temperature:

$$\frac{n_n}{n_s} = [\frac{T}{T_c}]^4 \tag{1.5}$$

Λ is a function of the London Penetration Depth, λ_L:

$$\Lambda = \mu_0 \lambda_L^2 \tag{1.6}$$

1.5 Quantum Computing

Over the past few years, despite the fact that computer technology has advanced significantly, there are still a lot of computational issues in physics and other fields of study that are too big to be solved on a traditional computer leading to a growing interest in quantum computing. Many academic and industrial research groups have selected quantum computing as their major route to developing scalable quantum information processing systems. Quantum computers take advantage of quantum physics' unique properties, such as superposition, entanglement, and quantum interference, and apply them to computing. The fundamental unit of information in quantum computing is a qubit. Qubits serve a similar function in quantum computing as bits do in classical computing, but they act considerably differently. Classical bits are binary and can only carry the values 0 or 1, whereas qubits can hold a superposition of all conceivable states, which can be represented as any point on the surface of a 3D sphere - the "Bloch Sphere" (shown in Fig 1.3) [25]. Each qubit can exist in such a superposition state. Still, the system as a whole is also capable of being in a superposition of every possible combination of all the qubits' distinct states. Because every potential state may be stored and processed simultaneously with all the other possible states, a quantum computer could be potent. If we have N qubits, then there are 2^N potential states in the superposition, making the number of possible states that could be present extremely large. In keeping with the comparison between qubits and classical bits, qubits can be excited by microwaves and magnetic fields while classical bits can be excited and controlled by DC voltage.

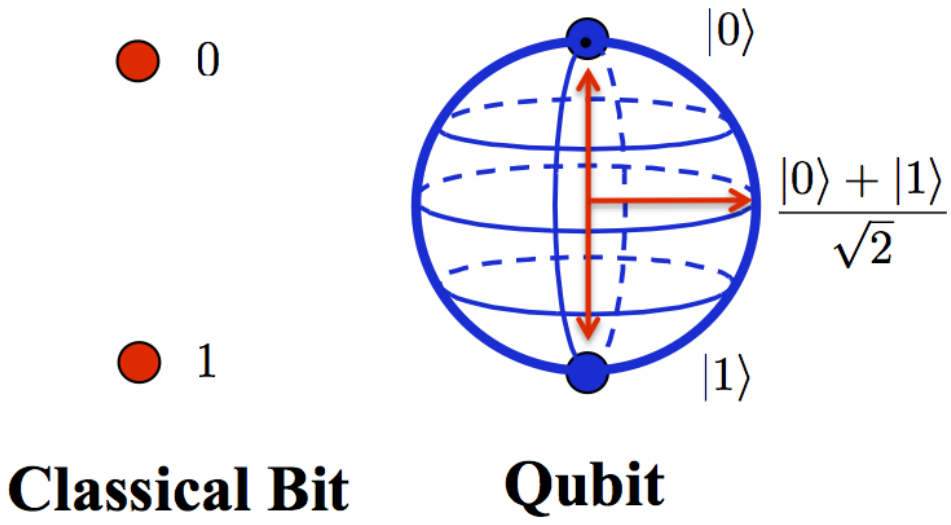

Figure 1.3: Image showing the comparison of different states in a classical bit and qubit.

The quantum computer is far more susceptible to faults than a classical computer would be due to the utilization of quantum states. Decoherence, a process in which the environment interacts with the qubits, changes their quantum states unpredictably, and results in the loss of information stored by the quantum computer, is the cause of these errors. Decoherence could result from a variety of environmental factors, including changing magnetic and electric fields, radiation from hot things nearby, and qubit crosstalk. Cryogenic temperatures are needed to slow down the atomic motion, provide a vibration-free environment, decrease error rates and provide longer qubit coherence times. A cryogenic system can require temperatures as low as 10 mK, which can be maintained in a dilution refrigerator.

1.6 Superconducting Quantum Computing

Many different quantum systems, such as trapped ions [26, 27, 28], superconducting qubits [29, 30, 31, 32], photons [33, 34, 35], and silicon [36, 37], can be used to create quantum computers. Superconducting qubits in particular have emerged as a major possibility for scalable quantum processor architecture. Superconducting quantum computing employs superconducting electrical circuits to implement quantum computing. In 1999, a simple qubit

for superconducting computing was developed [38]. The quality and quantity of qubits have been scaling up quickly in recent years.

One of the key advantages of superconducting qubits is their ability to be fabricated using standard microfabrication techniques, which makes them relatively easy to manufacture and scale up. Another advantage is their relatively long coherence times, which is the amount of time a qubit can remain in a superposition state before decoherence occurs. This makes them suitable for use in complex quantum algorithms.

1.7 Research Goal

Typically, precisely timed and shaped microwave pulses of particular frequencies are sent into groups of qubits or individual qubits to execute quantum computational operations on their states. Limited attention has been given to solving the problem of how to transmit and receive a large number of RF and microwave signals efficiently for cryogenic and quantum applications. As the number of qubits increase, the circuitry required for qubit readout increases inside a dilution refrigerator. Dilution refrigerators usually have limited physical volume and cooling capacity for the superconducting circuitry and coaxial data cables. These bulky coaxial cables add to the thermal load and are likely to cause thermal leaks between various temperature stages inside the dilution refrigerator making it impractical to use these cables in the long run. In recent times, a lot of work has gone into developing thin-film flexible superconducting cables as a potential alternative for coaxial cables [13, 14, 39, 40].

However, the impedance mismatches are currently high in these flexible superconducting cables introducing the need for better impedance matching of cables. Changing temperature can change the performance of the materials (i.e. dielectric and conductor properties). The dielectric properties such as loss tangent need to be characterized as a function of frequency at cryogenic temperatures. Therefore, it is not only necessary to select various materials with excellent temperature stability, but also to consider issues such as signal integrity at long

transmission. In this dissertation, I discuss the major signal integrity issues for these thin superconducting structures and suitable solutions to these challenges.

1.8 Dissertation Structure

Chapter 2 presents a new interconnect and connector technology between different temperature stages inside a dilution refrigerator using flexible stripline cables. Design, fabrication, mechanical assembly, and results are discussed. I performed direct current (DC) and time-domain reflectometry (TDR) measurements on the assembly to evaluate the superconductivity of the assembly and impedance mismatch at the connector region, respectively. I implemented a distributed element model for the connection region using Advance Design System (ADS) circuit-level schematic simulations and matched the measured results.

In **Chapter 3**, I discuss the effect of gamma radiation on superconducting microwave resonators with different material stack-ups and superconducting metals. The resonators were subjected to different doses of radiation and the quality factor of the resonators was measured and compared to see the amount of degradation if there was any. Resonator design, layout, simulation, fabrication techniques, sample assembly procedures, and experimental setup are among the experimental approaches mentioned in this chapter.

In **Chapter 4**, I investigate the characterization of material losses in superconducting structures at cryogenic temperatures using very long microstrip resonators. This study intends to shed light on the losses related to various materials and fabrication methods through a thorough investigation of the resonance frequency spectrum. Nb and Al conductor resonators fabricated using liftoff and etching processes were characterized and compared at cryogenic temperatures. Researchers can make significant progress in building high-performance quantum computers that can fully utilize quantum physics by determining the most advantageous production techniques.

In **Chapter 5**, I summarize the main results of this dissertation and in **Chapter 6**, I discuss the related future research.

Chapter 2

Face-to-face Connector Scheme For Flexible Cables

Interconnects and connectors play a crucial role in cryogenic systems, which are used to operate devices at extremely low temperatures, typically below 77 K (liquid nitrogen temperature) and even down to a few mK temperatures. These low temperatures are required to achieve and maintain superconductivity in certain materials, which enables the development of high-performance electronic devices, such as quantum computers.

In cryogenic systems, interconnects and connectors are essential for transmitting electrical signals between various components, such as sensors, filters, amplifiers, and power supplies. These components are typically housed in separate cryogenic environments and need to be connected to each other via cables, wires, or other types of interconnects. However, at cryogenic temperatures, the electrical properties of materials change significantly, leading to increased signal transmission losses, and increased noise. Therefore, it is important to carefully design and select interconnects and connectors that can maintain reliable signal transmission and minimize losses and noise [41, 42, 43].

Moreover, cryogenic systems often operate in harsh environments, such as high vacuum, strong magnetic fields, and extreme vibrations, which can aggravate minor imperfections, compromise strength, and increase stress. These stresses can lead to deformation, breakage, or loss of electrical contact, which can significantly affect the performance and reliability of the system. Therefore, interconnects and connectors need to be designed to withstand these harsh conditions and maintain stable and reliable electrical contact.

So, engineering efficient and reliable densely integrated interconnects and connectors for quantum and cryogenic information processing systems is a key challenge in achieving practical packaging and integration technologies. Over the past several years, there has been

a greater demand for solutions to various interconnect problems at cryogenic temperatures such as minimizing interconnect cross-sections, reliability and repeatability of interconnects. The conventional solution in current integrated cryogenic and quantum electronic systems has been to install many individual coaxial cable segments into a radio frequency assembly, using standard microwave connectors [44, 45, 46, 47, 48]. Because of system limits such as volume and thermal load, these rigid or hand-formable co-axial cables are bulky and typically hinder the integration of high-density I/O signals into a cryogenic environment.

Polyimide thin films offer the advantages of lower thermal load, and faster cooling, and provide high-density multi-signal transmission lines with very low dielectric crosstalk [49, 50, 40]. Cryogenic interconnect issues have been addressed by several research groups and multiple solutions have been developed regarding cryogenic interconnect challenges for thin-film flexible cables [51, 52, 13, 53, 54, 14, 55, 56, 57]. However, there are still some issues to be resolved, such as the density of the commercially available connectors used for interfacing flexible thin films, impedance mismatch, and ground discontinuities.

Previous research studies on connectors [15, 58] showed promising results using a connector to form a bridge connection between two superconducting flexible cables. In this work, I implemented an interconnection scheme between two flexible cables by a direct face-to-face connection of contact pads present on one of the ends of each cable. This cable-to-cable connection approach for flexible superconducting cables shows great promise as an interconnect scheme for future superconducting and cryogenic electronics systems, including superconducting quantum computing applications.

2.1 Design

This face-to-face connection approach consisted of two flexible superconducting stripline cables, bottom, and top Mo pieces as shown in Fig. 2.1. Two different flexible stripline cable designs were used in this work. The cables were designed to have a characteristic impedance of 20 Ω. Low-impedance transmission lines have several advantages for quantum circuits,

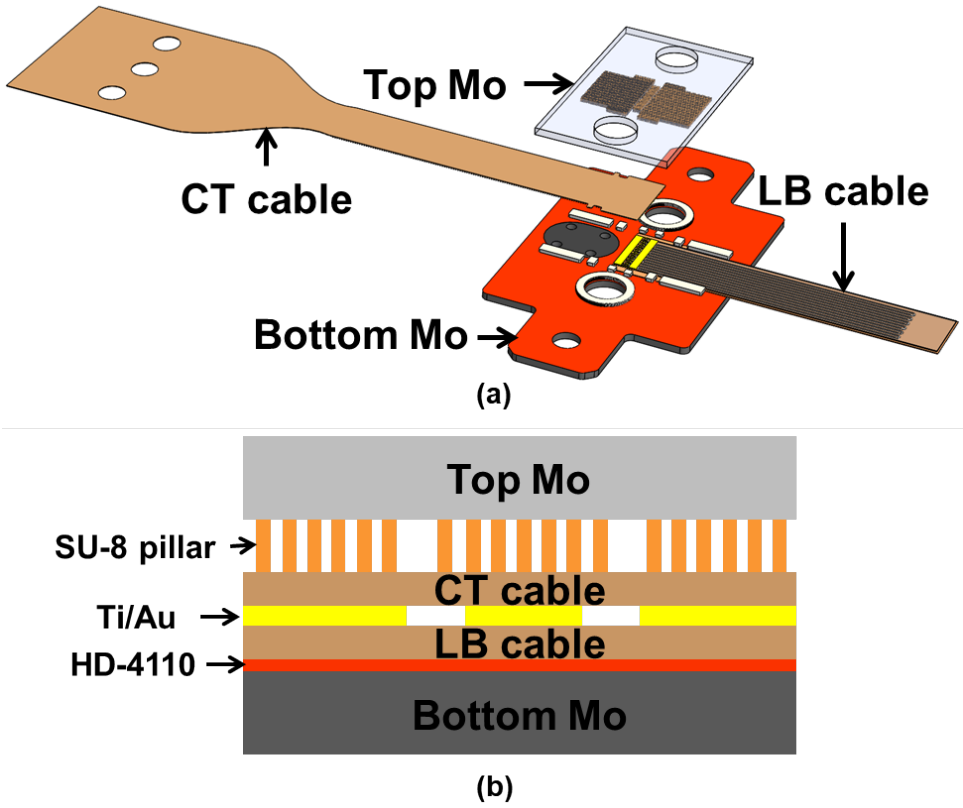

Figure 2.1: (a) 3-D view of disassembled connector assembly showing the components and assembly order. (b) Cross-section view in the connection region of the cables.

including reduced noise and thermal fluctuations, lower energy dissipation, and improved coupling with other components [59, 60]. Each cable consisted of 86 µm wide 12 parallel Nb signal lines with 300 µm pitch and contact pads on one of the ends to accomplish a direct face-to-face connection. The other end of signal lines on one of the cables denoted the "connector tester" (CT) cable, were routed to a wider pitch (750 µm) to be able to make the connection to a flip-chip bonded commercially available PCBeam™ connector from Neoconix. The other cable denoted the "loop-back (LB)" cable, had 12 signal lines, each looped back to an adjacent signal line, making a total of 6 loop-backs. Fig. 2.2 shows the ADS layout of the CT and LB cable.

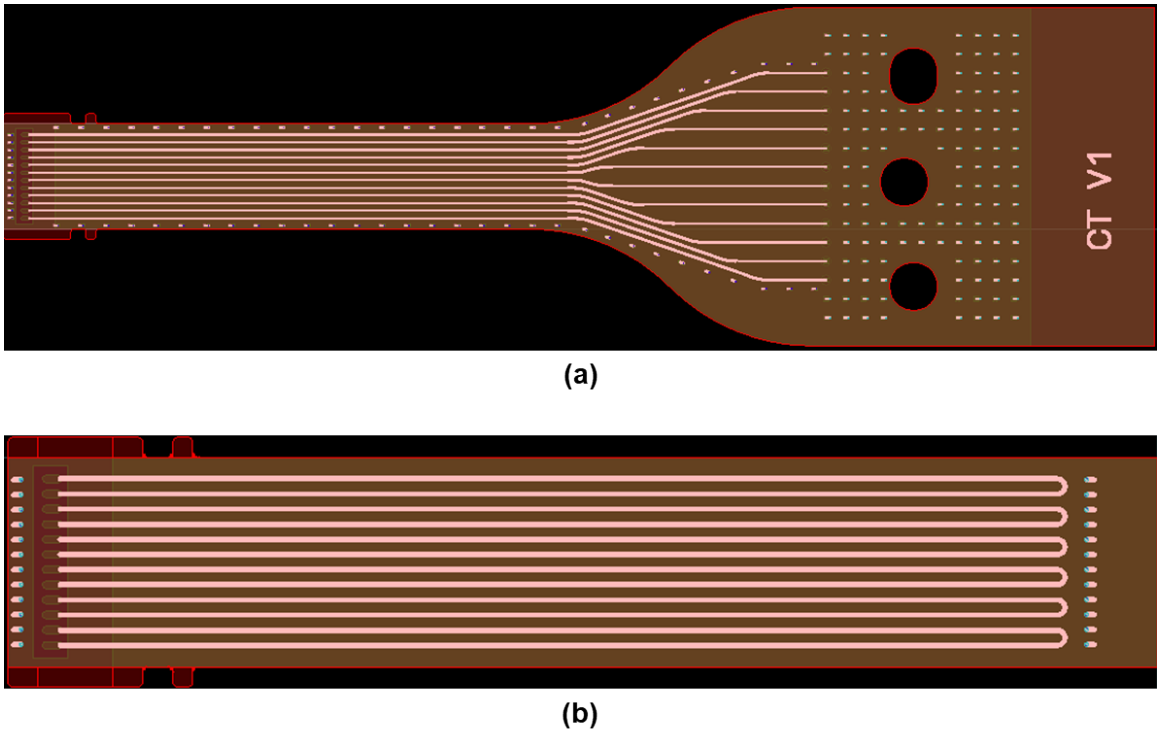

Figure 2.2: ADS layout design of (a) Connector tester cable (b) Loop-back cable.

2.2 Simulations

2.2.1 3D EM Simulations

Ansys HFSS electromagnetic simulations were performed to optimize the design and to determine how to perform an efficient and reliable transfer of electrical signal through the connector. The performance of these lines can be affected by various factors such as the geometry, the materials used, and the environment they are installed in. HFSS simulations with stripline structures were performed by varying the signal width and pitch between the signal lines to check the characteristic impedance and to look at the cross-talk values, respectively. Based on the simulation results, 86 μm of signal width and 300 μm of the pitch gave optimum results based on the initial goals, such as a characteristic impedance of 20 Ω, an insertion loss of less than 1dB/cm, and crosstalk of less than -30 dB up to 60 GHz. The length of the stripline structure simulated in HFSS was 5 mm. S-parameters from simulations of this shorter segment of the stripline structure were saved in the SNP

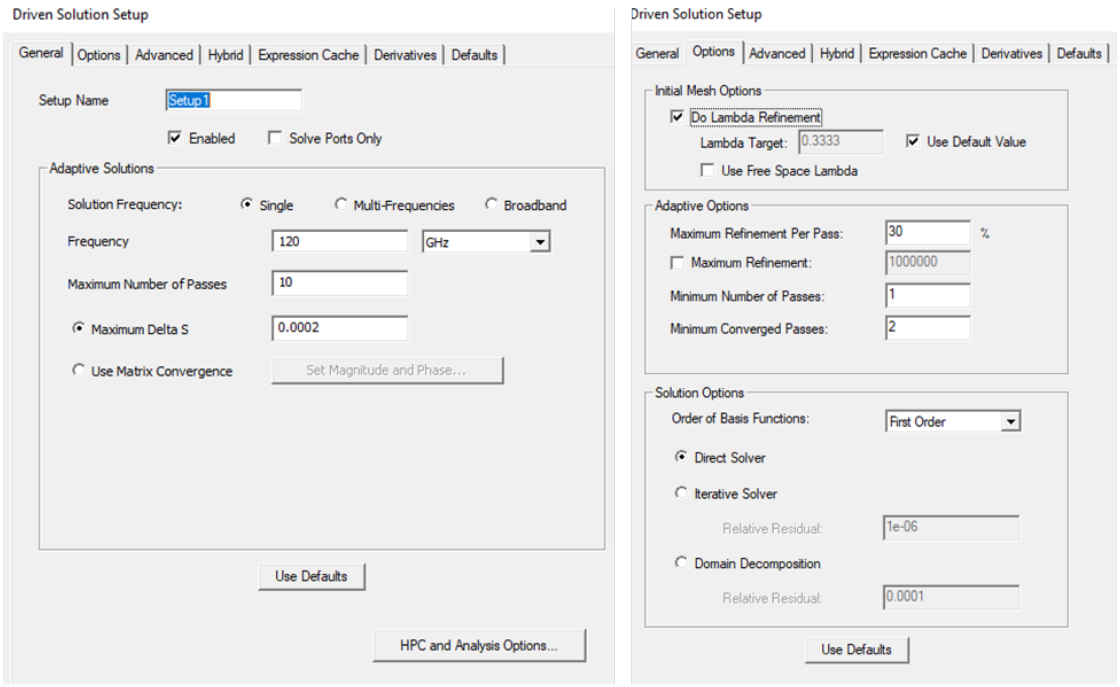

Figure 2.3: Solution set-up parameters used in HFSS. The solution setup parameters mainly help in determining the meshing parameters at solution frequency.

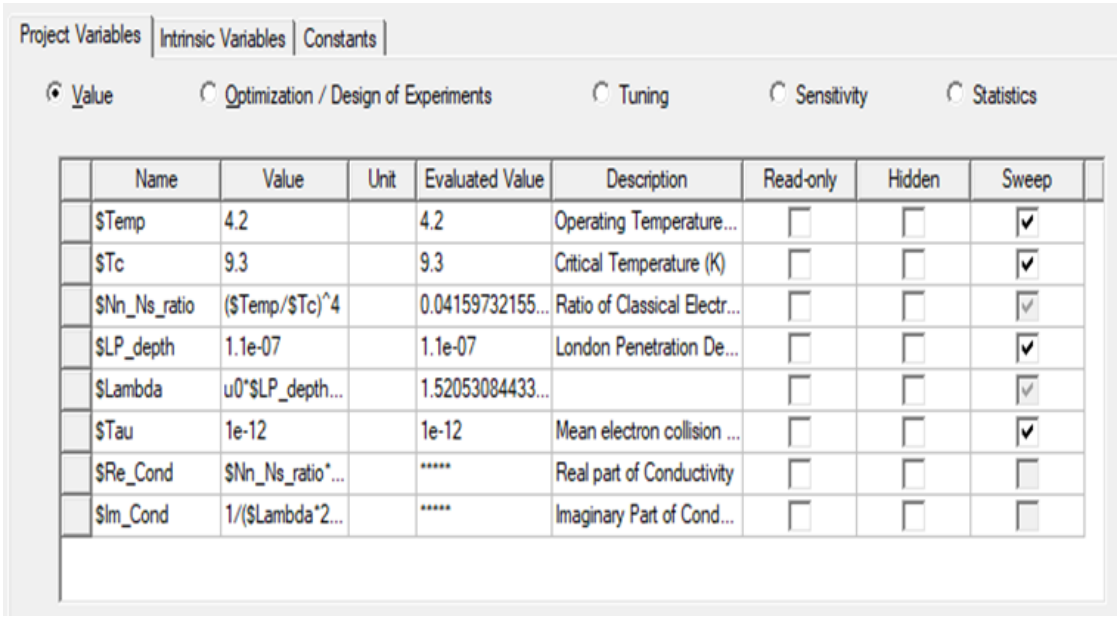

Figure 2.4: Simulation set-up to model the conductors as superconductors. $Temp is the simulation temperature, $Tc is the critical temperature, $Nn_Ns_ratio is the ratio of classical electrons to superconductive electrons, $Lambda is a function of λ_L, $Tau is mean electron collision time of classical conductor, $Re_Cond and $Im_Cond are real and imaginary part of conductivity, respectively.

Table 2.1: Project variables to model a conductor as a superconductor in ANSYS HFSS.

Variable name	Value
$Temp	4.2
$Tc	9.3
$Nn_Ns_ratio	($Temp/$Tc)^4
$LP_depth	1.1e-07
$Lambda	u0*$LP_depth^2
$Tau	1e-12
$Re_Cond	Nn_Ns_ratio*Tau/$Lambda* (1/(1+(2*pi*Freq*$Tau)^2))
$Im_Cond	1/($Lambda*2*pi*Freq)* (1+$Nn_Ns_ratio * (2*pi*Freq*$Tau)^2/(1 + (2 ∗ pi ∗ $Freq$ ∗ $\$Tau$)^2))

file format. The saved files were imported into ADS schematic simulations to concatenate and obtain the S-parameters of longer structures. Fig. 2.3 shows the solution set-up for the HFSS simulations. The solution frequency is used by HFSS to determine the maximum initial tetrahedra size and is the frequency at which HFSS explicitly solves the given model. The solution setup parameters mainly help in determining the mesh size. Fig. 2.4 shows the parameters used to model the conductors as superconductors in Ansys HFSS based on equations 1.3 and the same parameters has been reported in table 2.1. Fig. 2.5 and Fig. 2.6 show the return loss and insertion loss vs. frequency for the simulated 5mm long HFSS stripline structure. The return loss shows a good match to a 20 Ω characteristic impedance and the insertion loss is less than 1 dB/cm. Fig. 2.7 and Fig. 2.8 show the nearest neighbor crosstalk and Fig. 2.9 and Fig. 2.10 show the next-to-next neighbor crosstalk. The crosstalk plots show very minimal to no crosstalk between the signal lines with a pitch of 300 µm up to 60 GHz. Note that these crosstalk values are exceptionally low crosstalk due to the short length of the simulated stripline structure (5 mm).

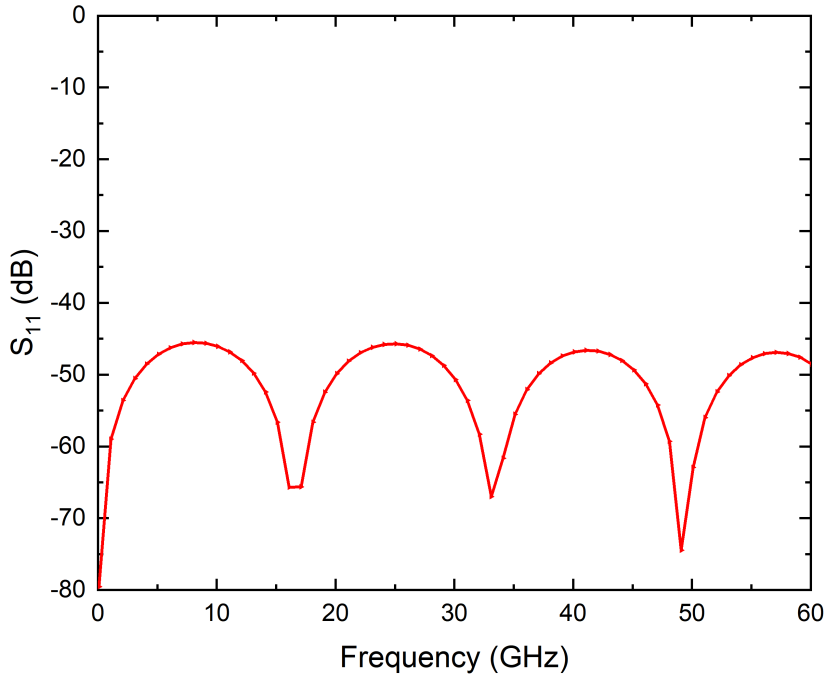

Figure 2.5: Return loss vs. frequency of 5 mm long stripline structure simulated in Ansys HFSS, which indicates a good match to 20 Ω characteristic impedance.

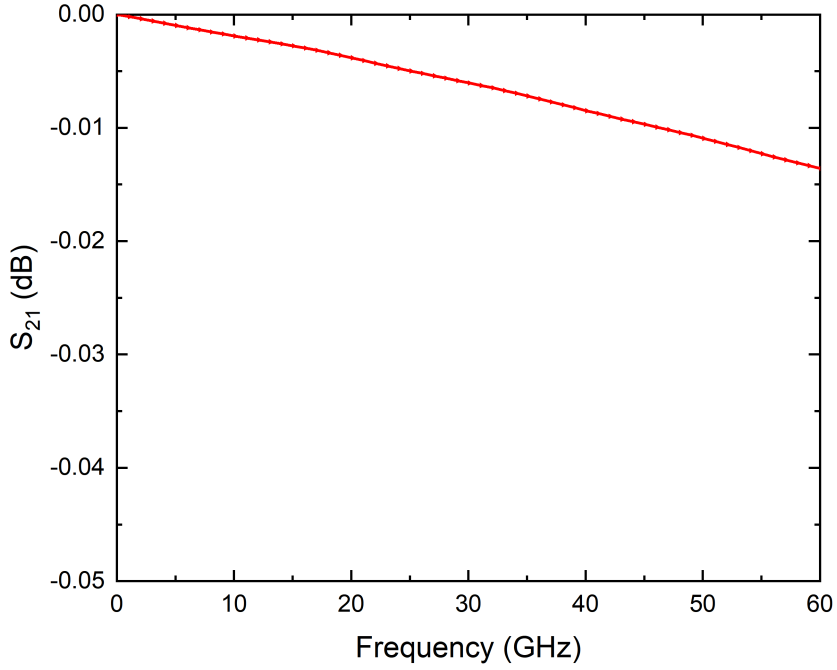

Figure 2.6: Insertion loss vs. frequency of 5 mm long stripline structure simulated in Ansys HFSS. The insertion loss is less than 1 dB/cm.

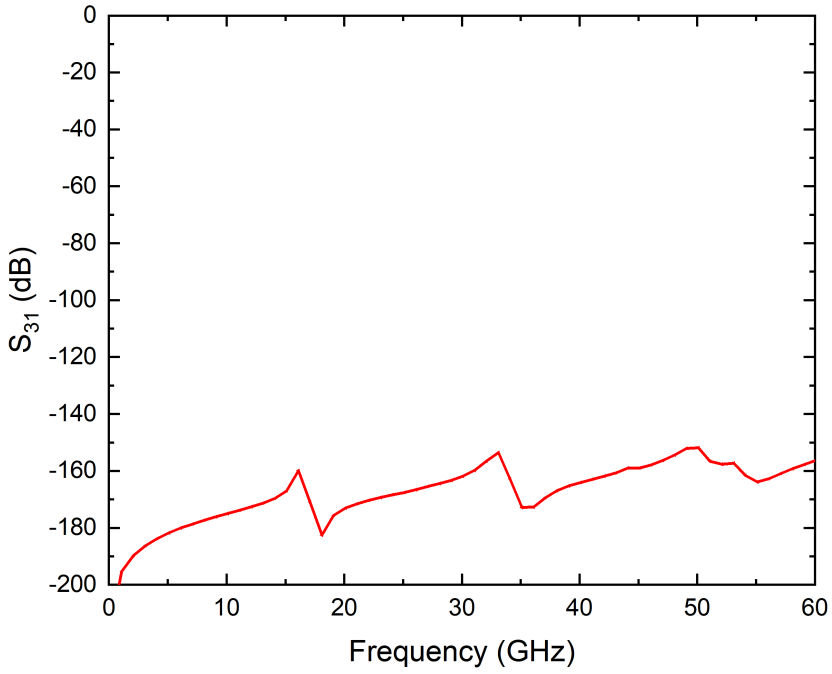

Figure 2.7: Nearest neighbor near-end crosstalk vs. frequency of 5 mm long stripline structure simulated in Ansys HFSS. Note: This is exceptionally low crosstalk due to the short length of the simulated stripline structure (5 mm).

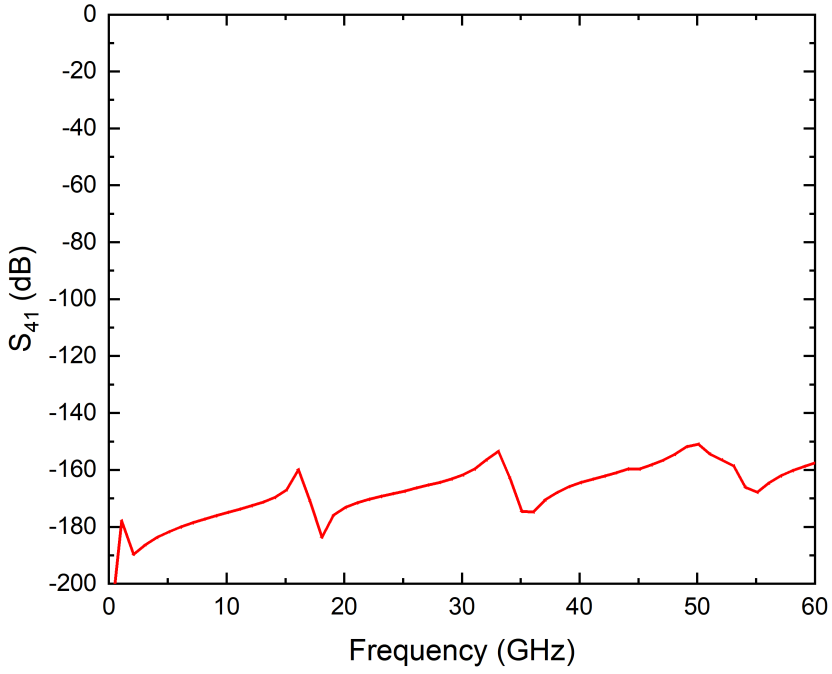

Figure 2.8: Nearest neighbor far-end crosstalk vs. frequency of 5 mm long stripline structure simulated in Ansys HFSS. Note: This is exceptionally low crosstalk due to the short length of the simulated stripline structure (5 mm).

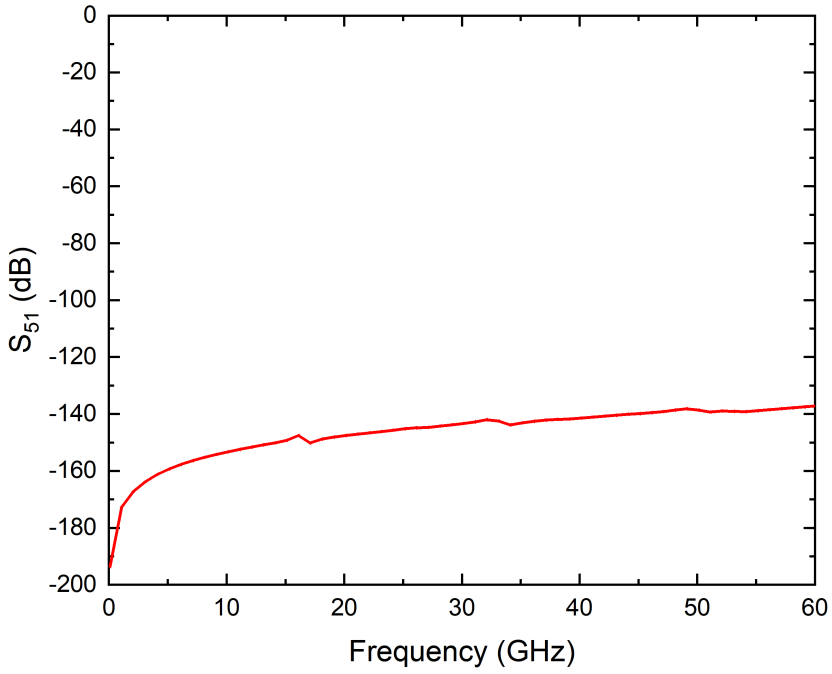

Figure 2.9: Next-to-next neighbor near-end crosstalk vs. frequency of 5 mm long stripline structure simulated in Ansys HFSS. Note: This is exceptionally low crosstalk due to the short length of the simulated stripline structure (5 mm).

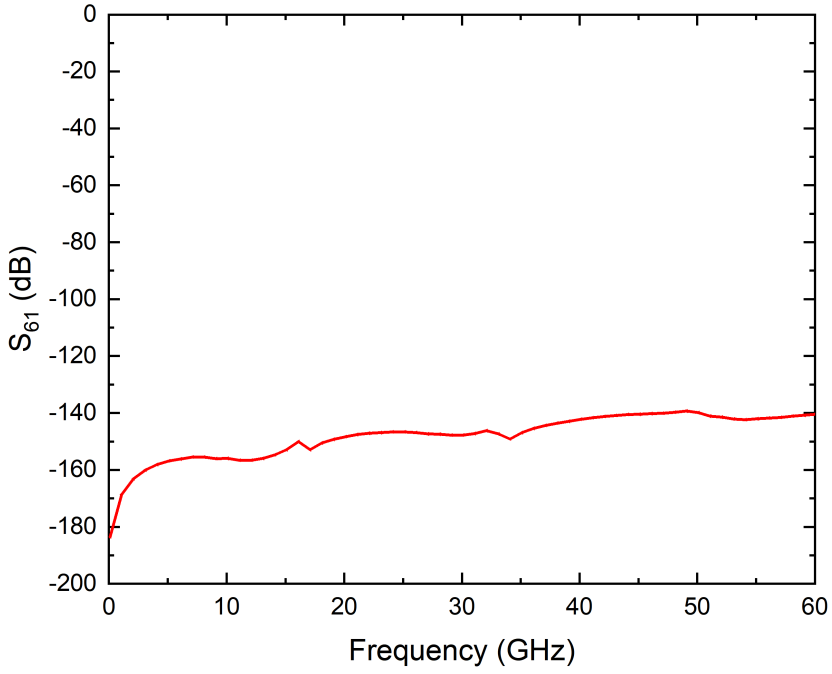

Figure 2.10: Next-to-next neighbor far-end crosstalk vs. frequency of 5 mm long stripline structure simulated in Ansys HFSS. Note: This is exceptionally low crosstalk due to the short length of the simulated stripline structure (5 mm).

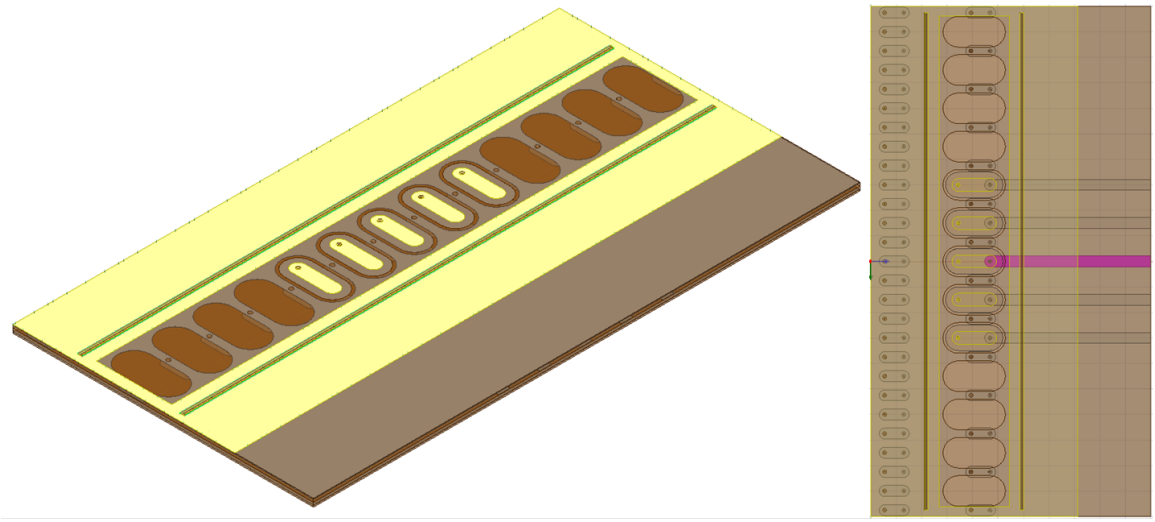

Figure 2.11: HFSS design of a single cable with connector region. (a) isometric view (b) top view with the central signal line selected.

3D EM simulations for the connector region were also performed using HFSS. Various design parameters were parameterized to be able to optimize the transition to have a better impedance match and less lossy. Fig. 2.11 shows the isometric view of the HFSS design of a single stripline used in simulations and the top view with the central signal line. Fig. 2.12 shows the simulated structure in HFSS. Various iterations of simulations showed that the transition is sensitive to a few parameters. These parameters are shown in Fig. 2.13. Parameter 1 is the signal pad width on the top ground layer and parameter 2 is the signal pad width on the contact layer.

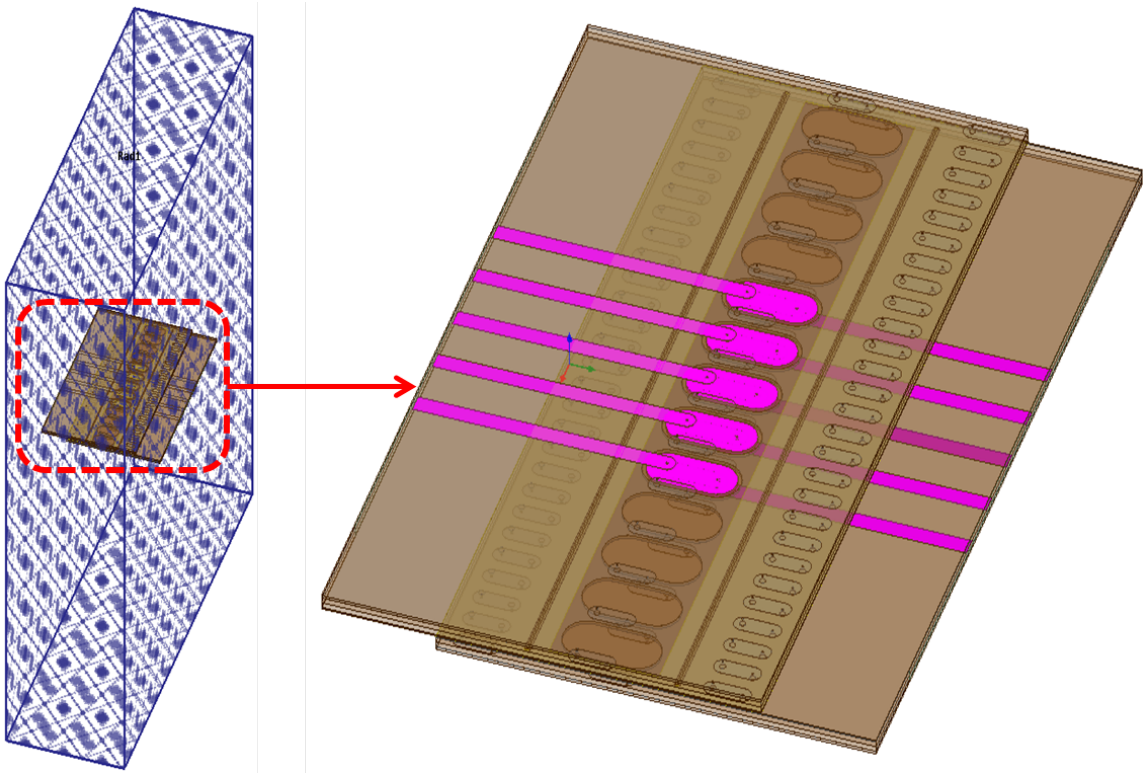

Figure 2.12: Simulated HFSS design of the connector region.

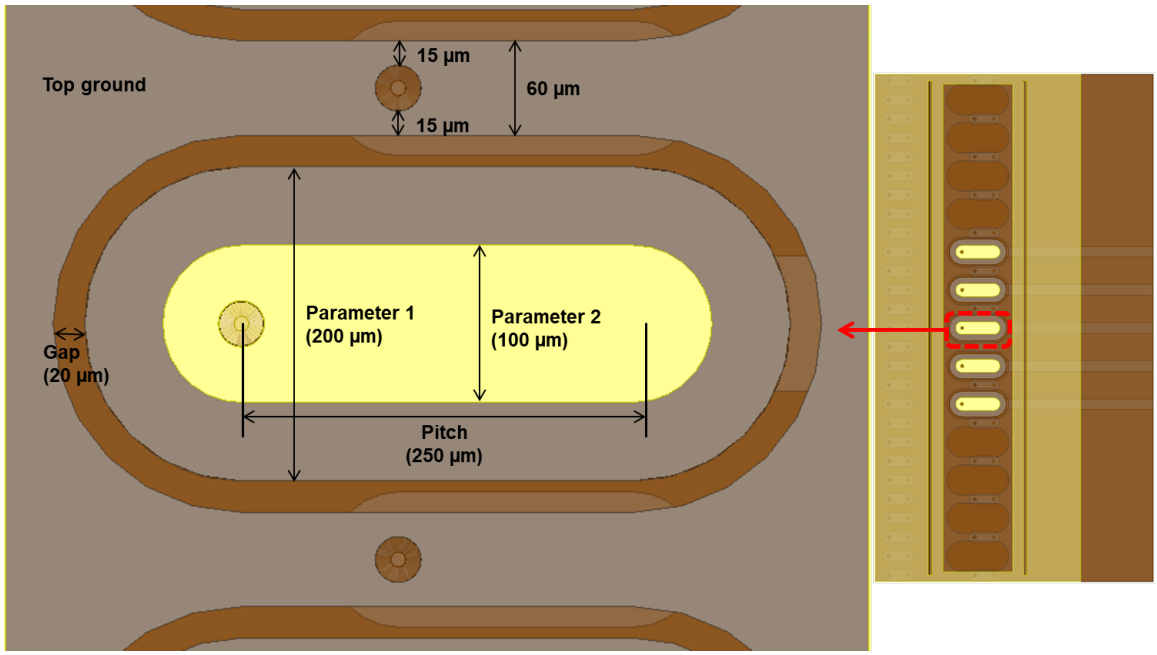

Figure 2.13: Signal transition region of the connector configuration showing the critical parameters in the design.

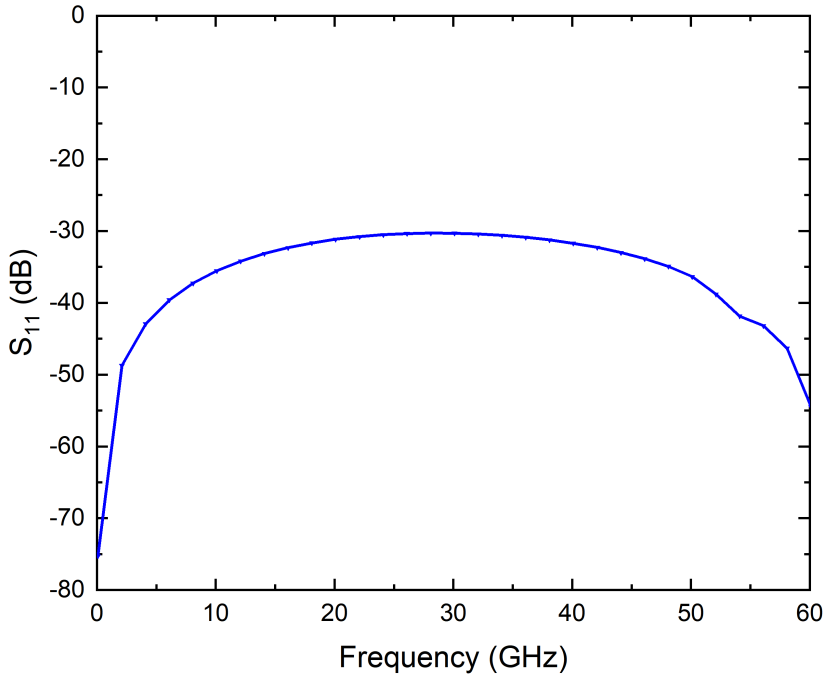

Figure 2.14: Return loss vs. frequency of the connector region simulated in Ansys HFSS.

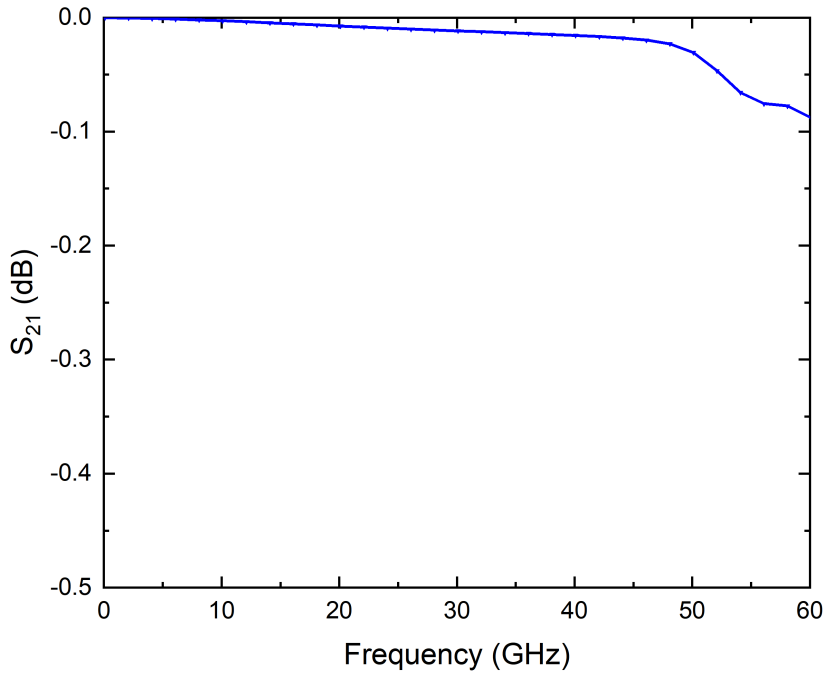

Figure 2.15: Insertion loss vs. frequency of the connector region simulated in Ansys HFSS.

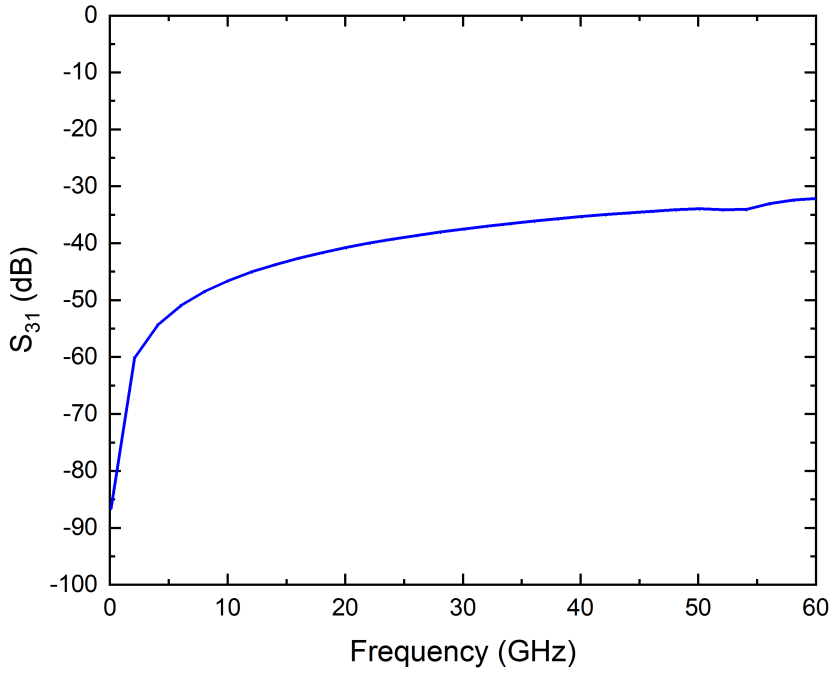

Figure 2.16: Nearest neighbor near-end crosstalk vs. frequency of the connector region simulated in Ansys HFSS.

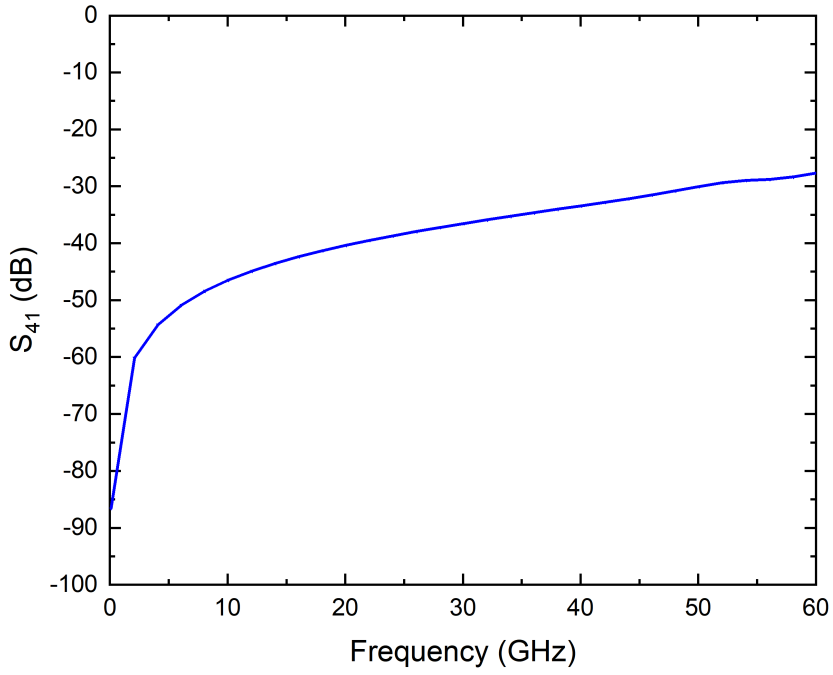

Figure 2.17: Next-to-next neighbor near-end crosstalk vs. frequency of the connector region simulated in Ansys HFSS.

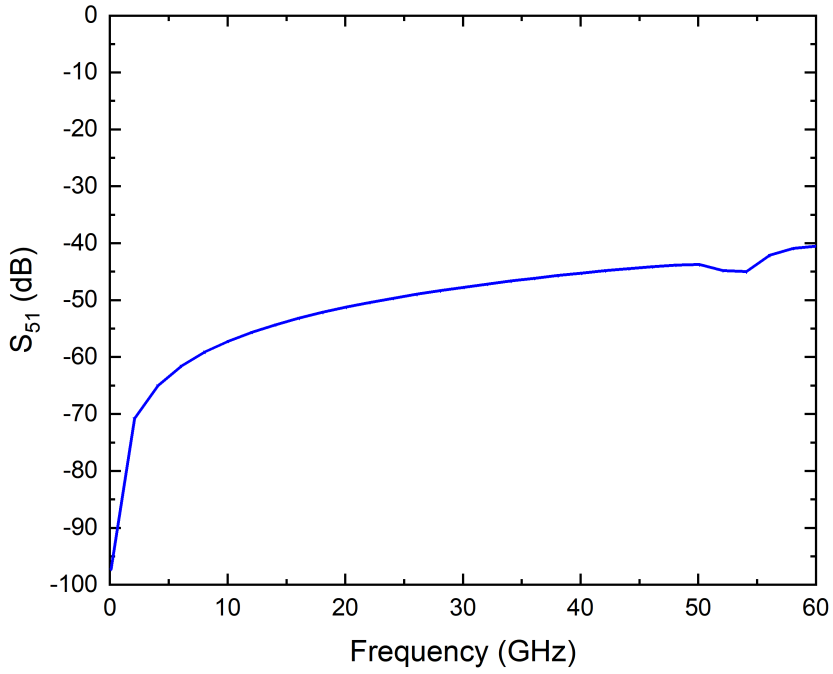

Figure 2.18: Next-to-next neighbor crosstalk vs. frequency of the connector region simulated in Ansys HFSS.

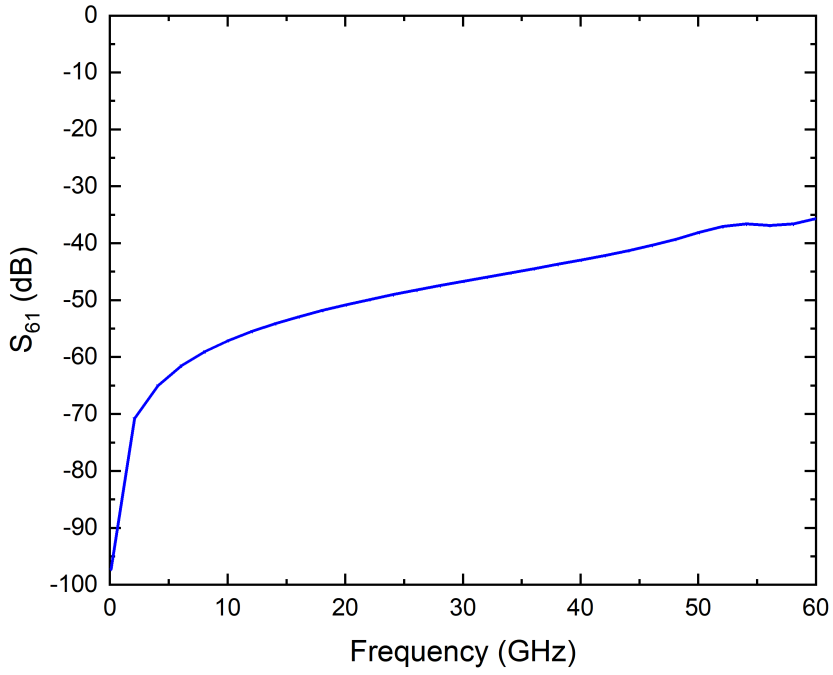

Figure 2.19: Next-to-next neighbor far-end crosstalk vs. frequency of the connector region simulated in Ansys HFSS.

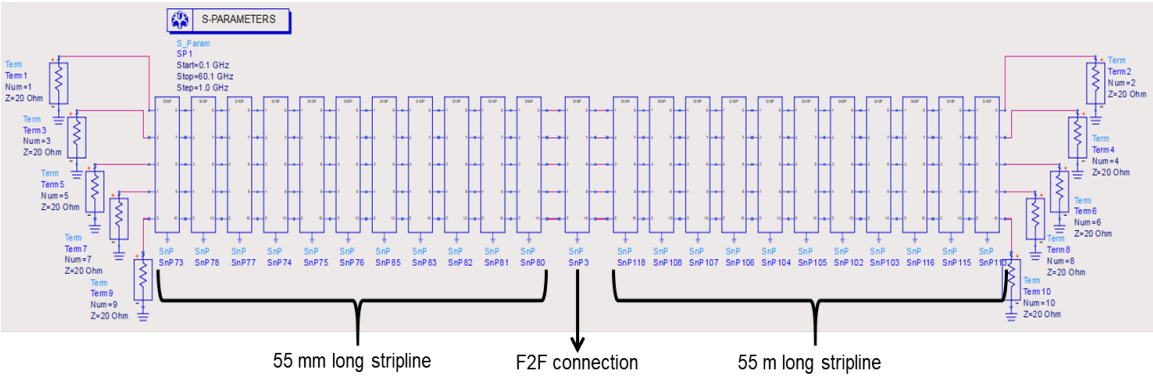

Figure 2.20: ADS Schematic of the concatenated SNP blocks for frequency domain simulations. The schematic consists of two 55 mm long striplines connected to each other with a connector region.

Fig. 2.14 and Fig. 2.15 show the return loss and insertion loss vs. frequency for the connector region simulated in HFSS. The return loss shows a good match to a 20 Ω characteristic impedance and the insertion loss is less than 1 dB/cm. Fig. 2.16 and Fig. 2.17 show the nearest neighbor crosstalk and Fig. 2.18 and Fig. 2.19 show the next-to-next neighbor crosstalk.

2.2.2 ADS Schematic Simulations

The SNP files saved from the HFSS simulations were imported into ADS and schematic simulations were performed on the concatenated S-parameter blocks. Fig. 2.20 shows the concatenated SNP blocks in the ADS schematic. The schematic consists of two 55 mm long stripline connected to each other with a connector region. The concatenated SNP blocks were simulated from 0.1 GHz to 60.1 GHz with a step size of 1 GHz. Fig. 2.21 and Fig. 2.22 show the return loss and insertion loss vs. frequency of the whole assembly. Fig. 2.23 and Fig. 2.24 show the nearest neighbor crosstalk and Fig. 2.25 and Fig. 2.26 show the next-to-next neighbor crosstalk. Fig. 2.27 through Fig. 2.32 show the consolidated S-parameters of the stripline (5 mm), connector, and assembly.

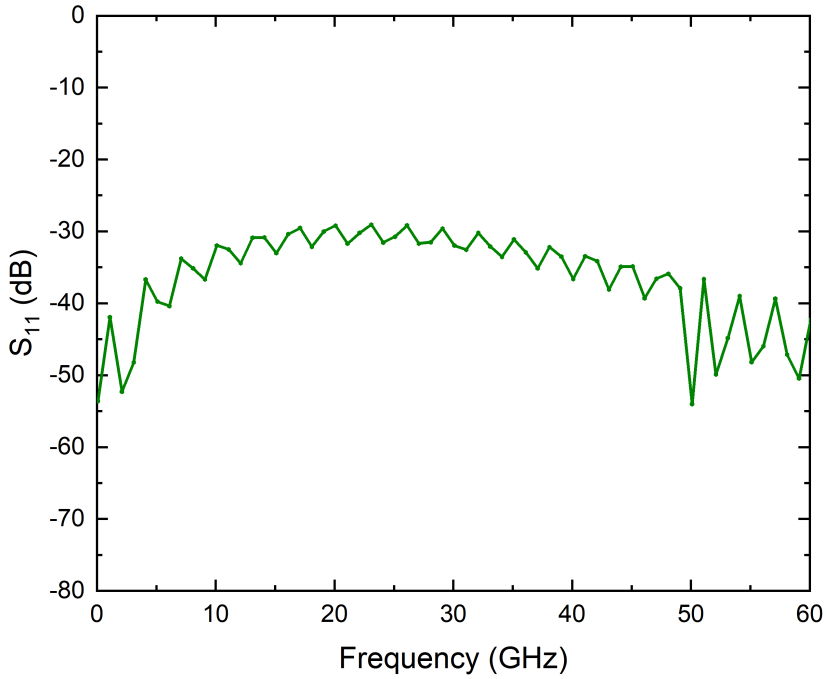

Figure 2.21: Return loss vs. frequency of the assembly. S-parameters saved from HFSS were concatenated in ADS schematic simulations.

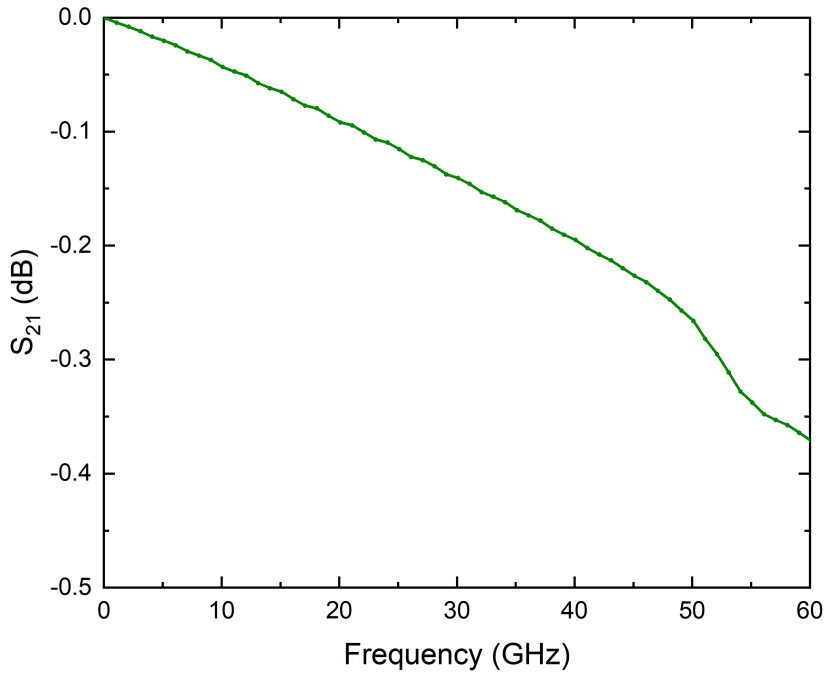

Figure 2.22: Insertion loss vs. frequency of the assembly. S-parameters saved from HFSS were concatenated in ADS schematic simulations.

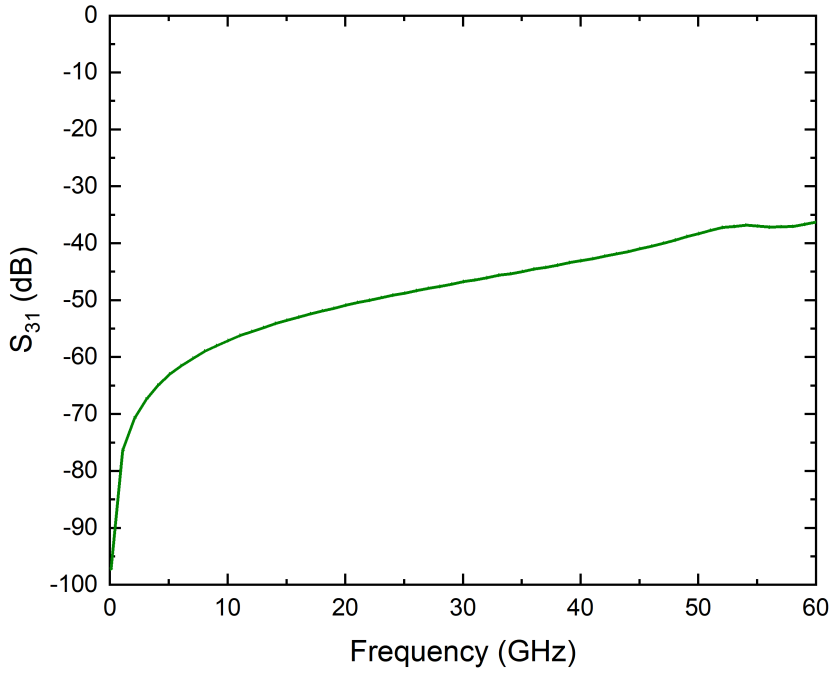

Figure 2.23: Nearest neighbor near-end crosstalk vs. frequency of the assembly. S-parameters saved from HFSS were concatenated in ADS schematic simulations.

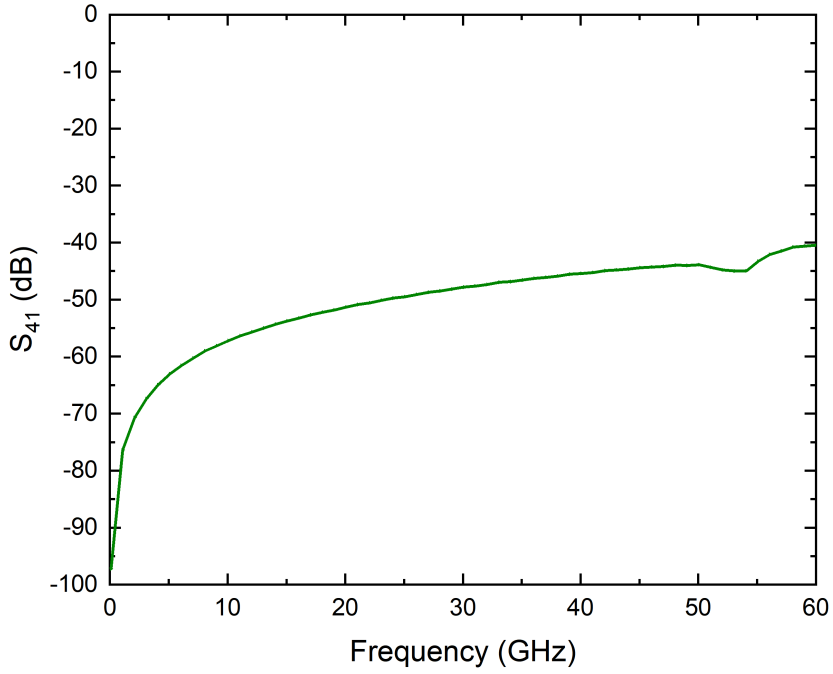

Figure 2.24: Next-to-next neighbor near-end crosstalk vs. frequency of the assembly. S-parameters saved from HFSS were concatenated in ADS schematic simulations.

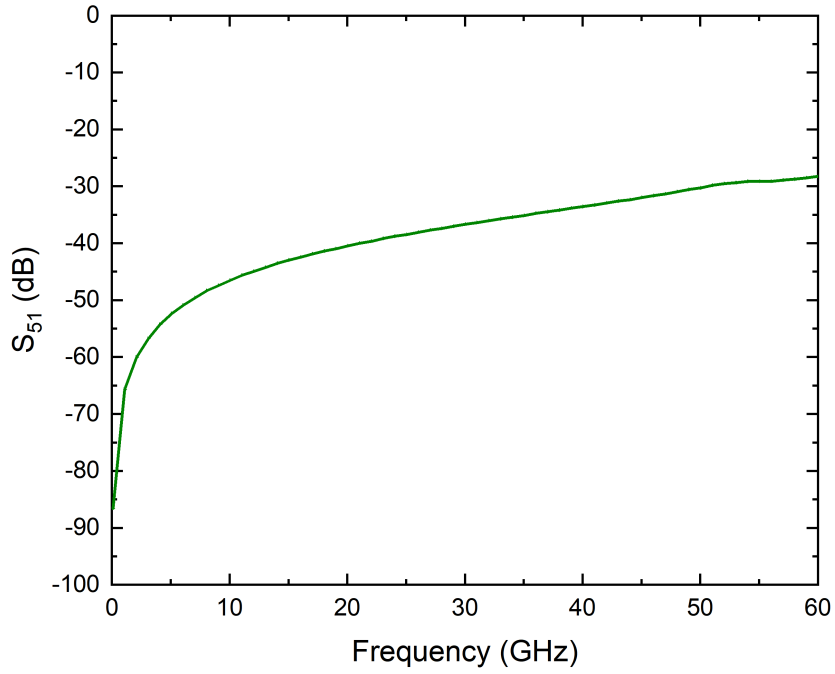

Figure 2.25: Next-to-next neighbor crosstalk vs. frequency of the assembly. S-parameters saved from HFSS were concatenated in ADS schematic simulations.

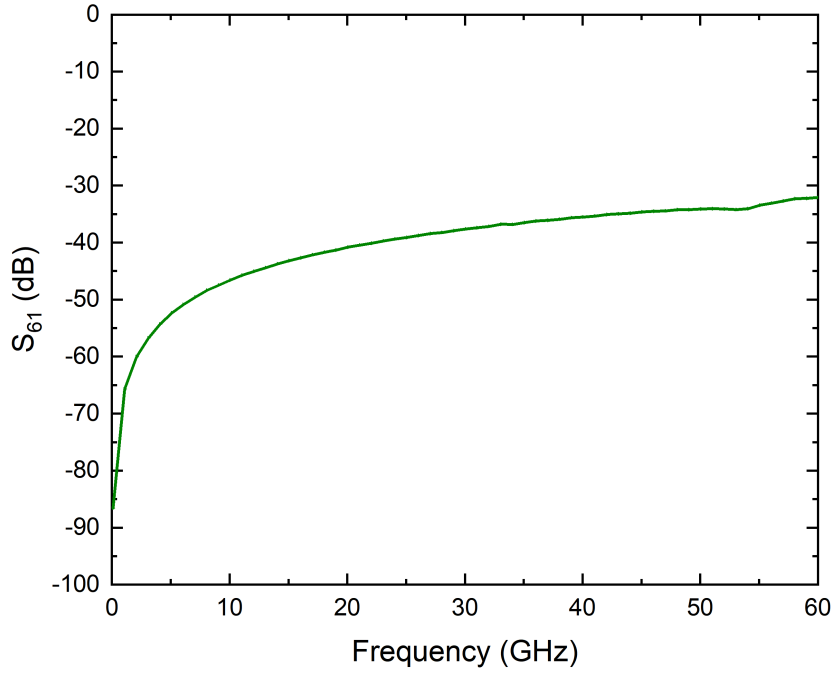

Figure 2.26: Next-to-next neighbor far-end crosstalk vs. frequency of the assembly. S-parameters saved from HFSS were concatenated in ADS schematic simulations.

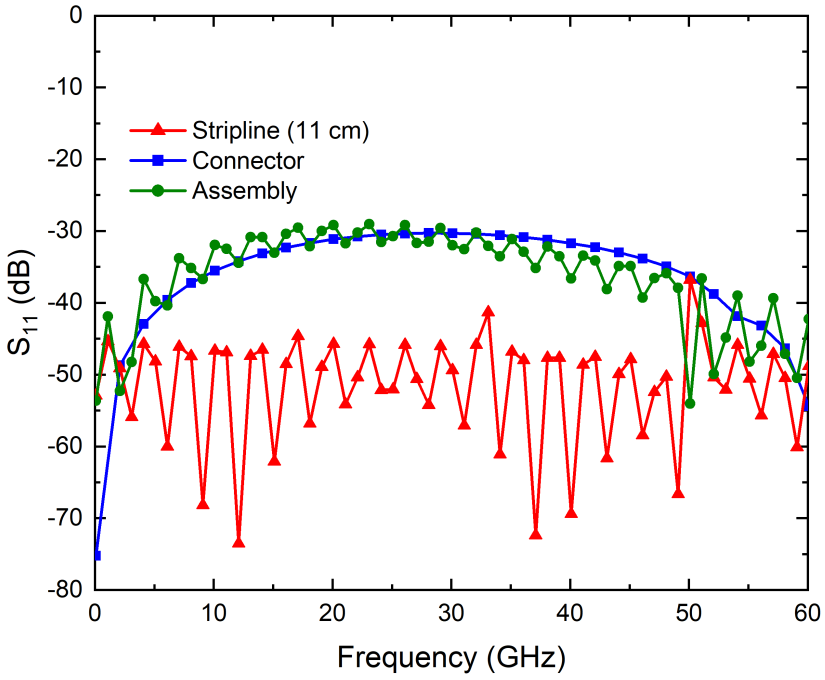

Figure 2.27: Consolidated plot showing return loss vs. frequency of 11 cm long stripline, connector, and assembly from ADS schematic simulations.

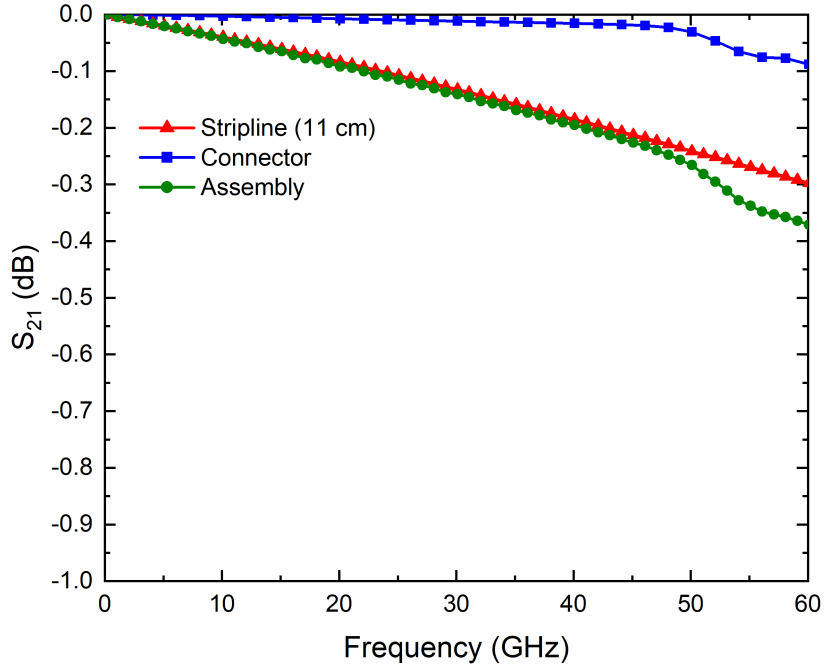

Figure 2.28: Consolidated plot showing insertion loss vs. frequency of 11 cm long stripline, connector, and assembly from ADS schematic simulations.

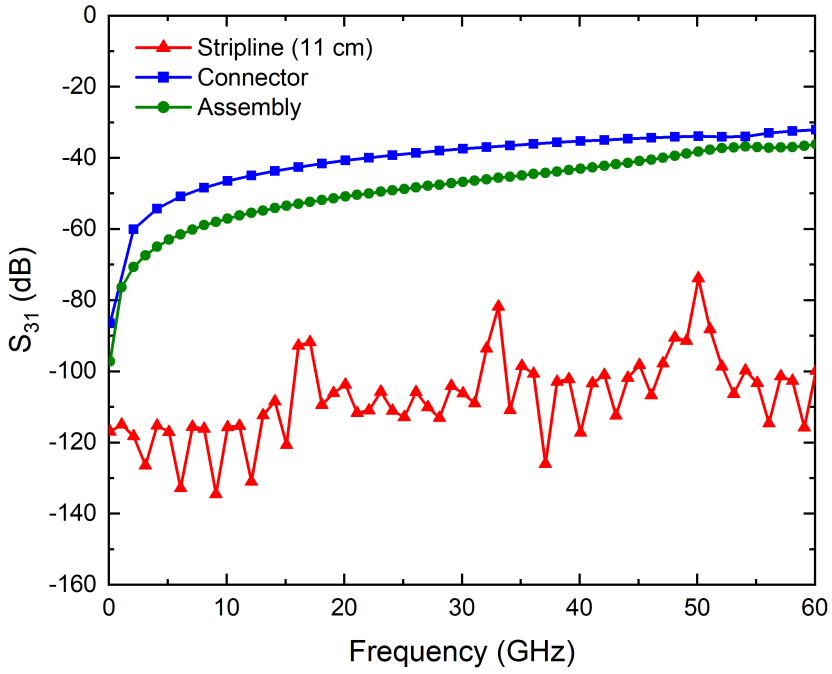

Figure 2.29: Consolidated plot showing nearest neighbor near-end crosstalk vs. frequency of 11 cm long stripline, connector, and assembly from ADS schematic simulations.

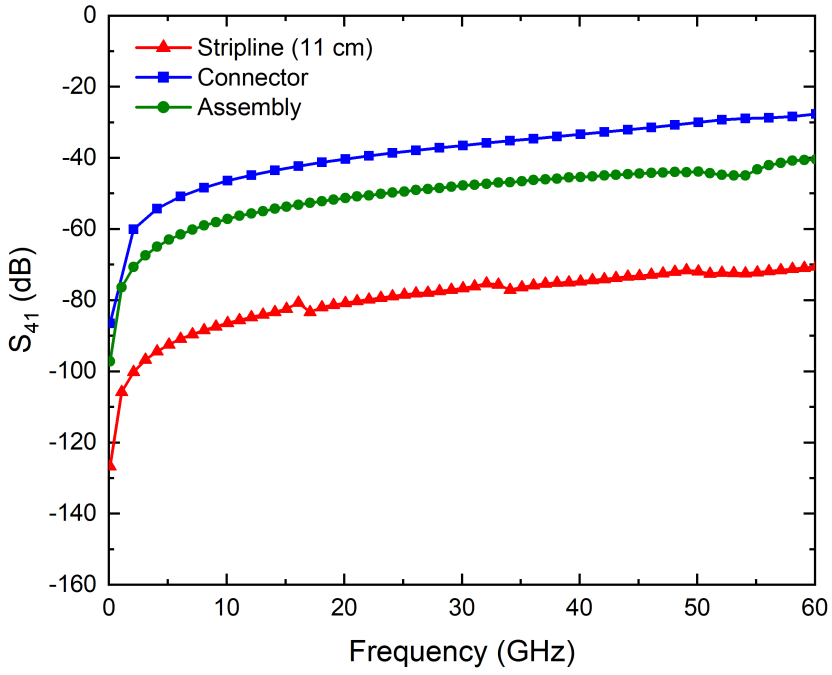

Figure 2.30: Consolidated plot showing nearest neighbor far-end crosstalk vs. frequency of 11 cm long stripline, connector, and assembly from ADS schematic simulations.

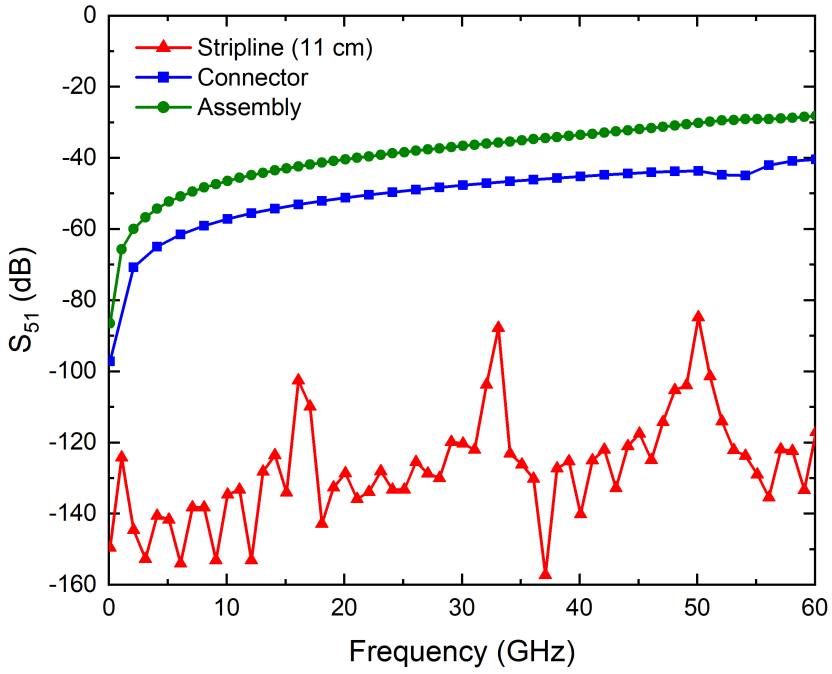

Figure 2.31: Consolidated plot showing next-to-next neighbor near-end crosstalk vs. frequency of 11 cm long stripline, connector, and assembly from ADS schematic simulations.

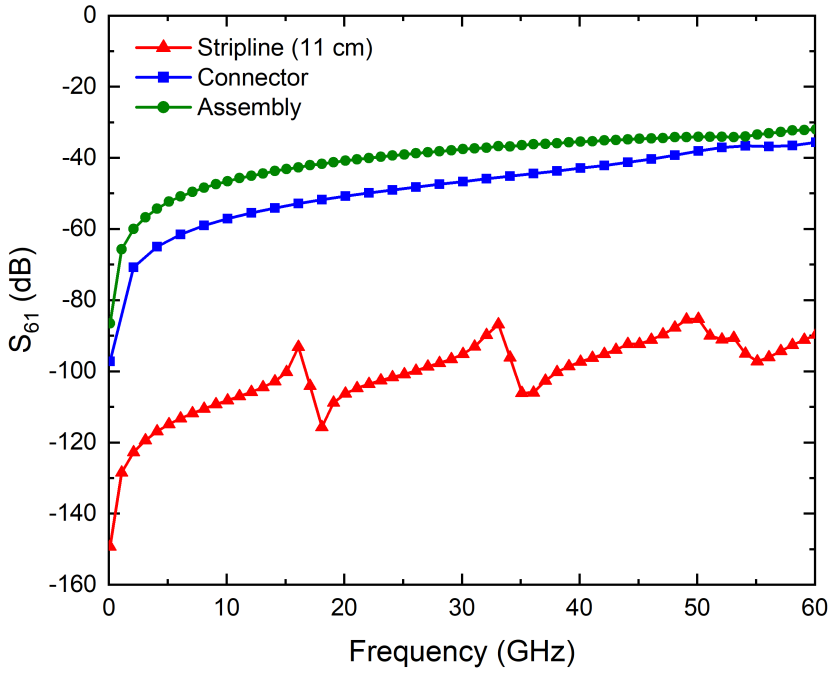

Figure 2.32: Consolidated plot showing next-to-next neighbor far-end crosstalk vs. frequency of 11 cm long stripline, connector, and assembly from ADS schematic simulations.

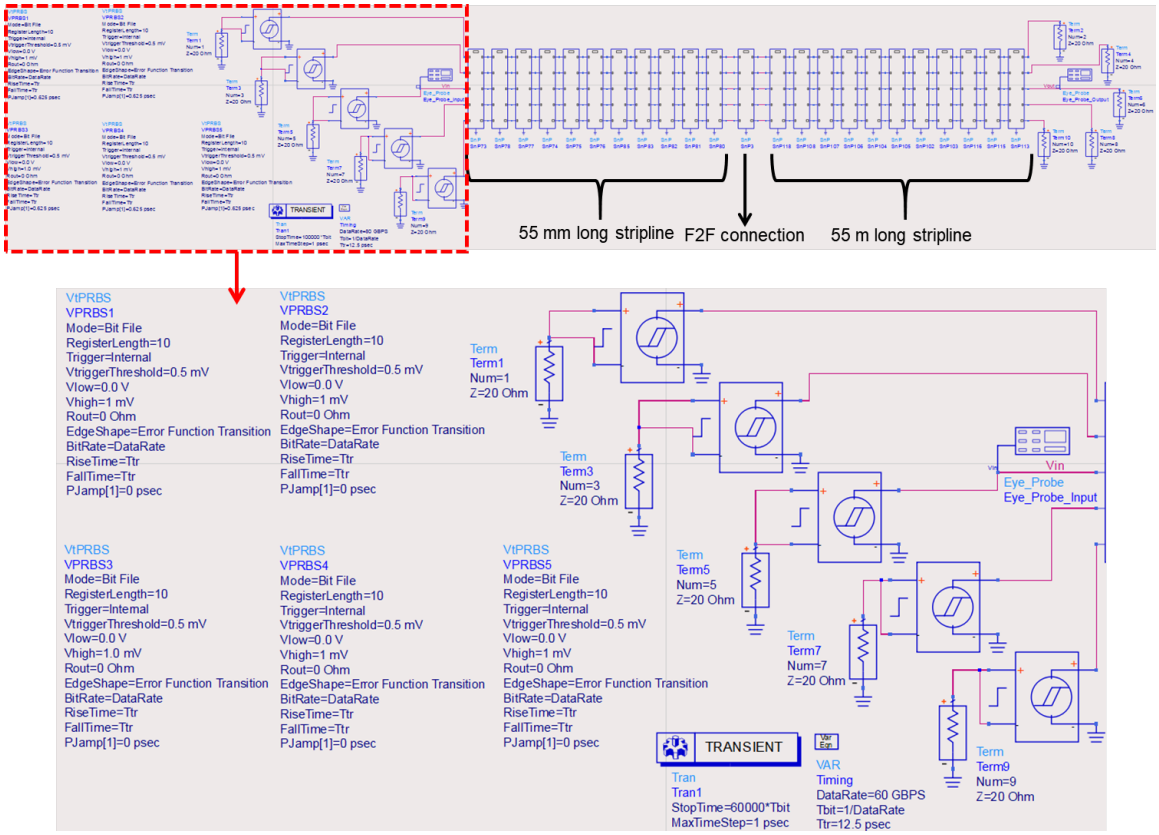

Figure 2.33: ADS Schematic of the concatenated SNP blocks for time domain simulations.

Time domain simulations are essential for signal integrity measurements as they provide a comprehensive view of the behavior of the transmission line, which helps to optimize the layout and termination of the line and identify and locate faults. Time domain simulations were performed on the assembly link to look at the eye diagrams and various parameters of it. Eye diagrams are an important tool for analyzing signal integrity in modern electronic systems. They provide a visual representation of the signal quality and help to identify and diagnose issues that can affect the performance of the system. They can help determine important signal characteristics such as signal rise time, fall time, and jitter. They can also identify issues such as noise, distortion, and crosstalk that can degrade signal quality and cause timing errors. Fig. 2.33 shows the set-up for time domain simulations. A large number of bits are run through the link and eye diagrams are investigated to look at the impact of the crosstalk. VtPRBS, a multi-functional time domain voltage source for Signal Integrity

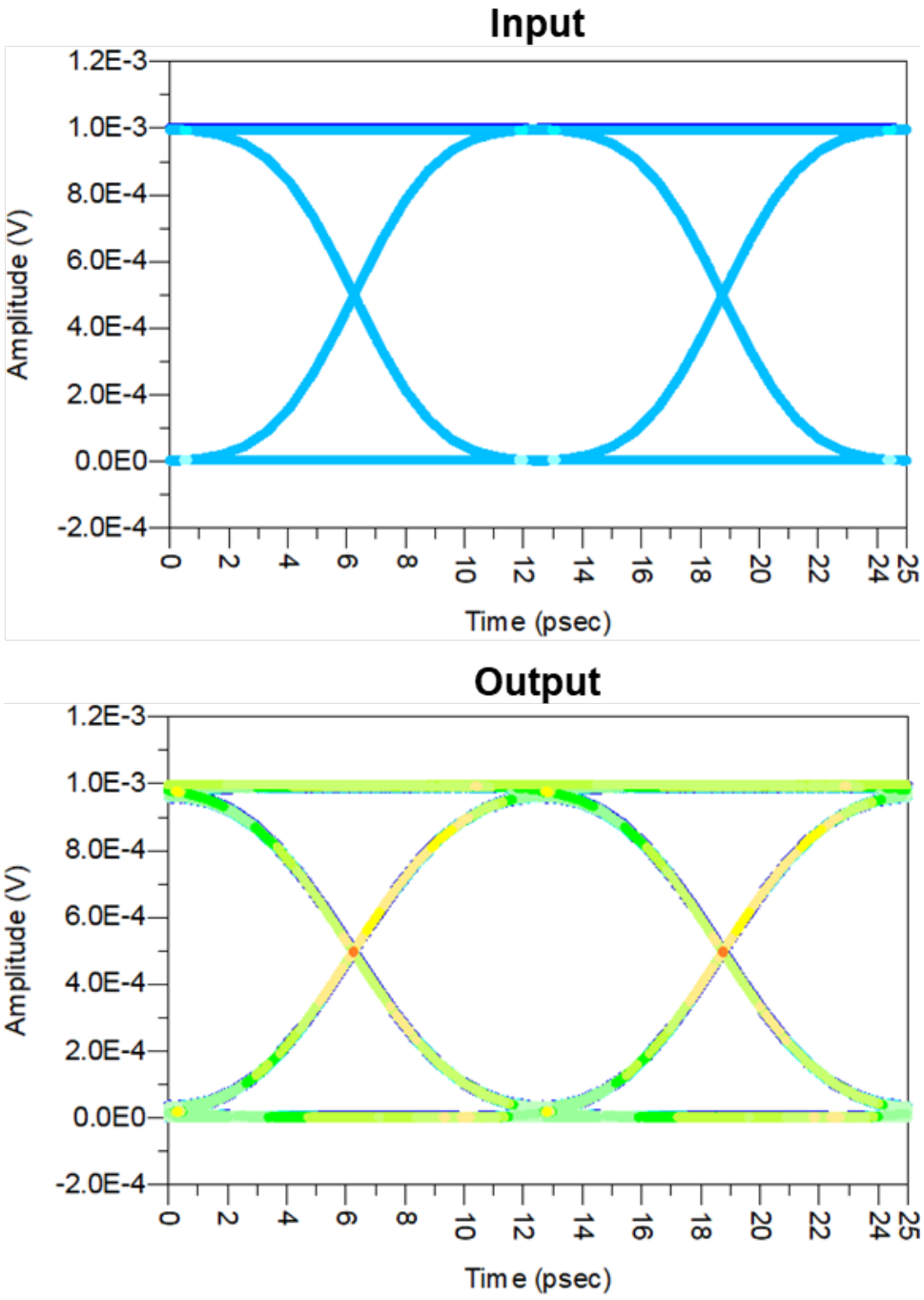

Figure 2.34: Eye diagram at the input and output of the link containing 11 cm long stripline structure. The rise/fall time of the signal was 12.5 psec. The eye height at the input and output were 9.76E-4 V and 8.83E-4 V, respectively.

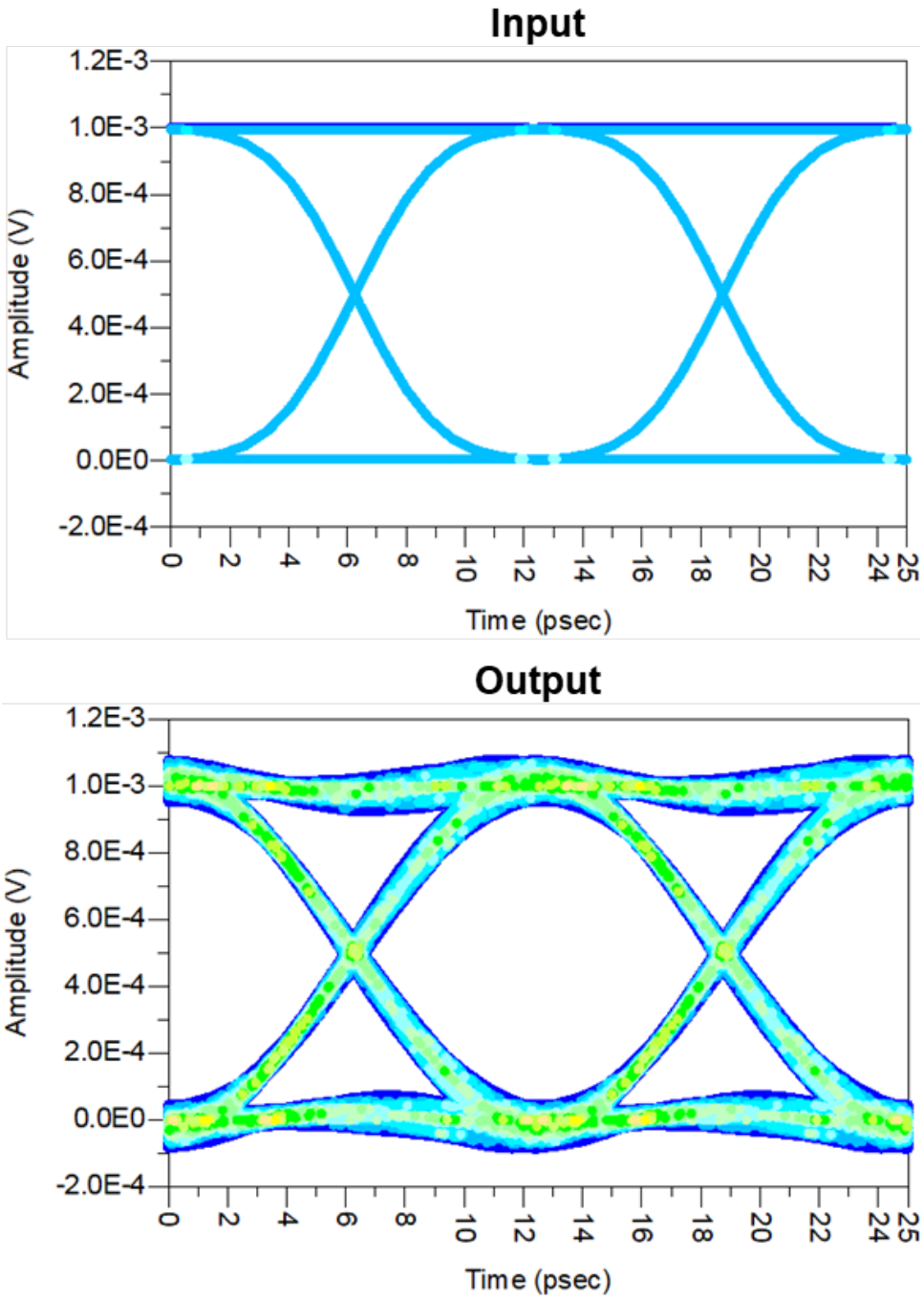

Figure 2.35: Eye diagram at the input and output of the link containing the connector region. The rise/fall time of the signal was 12.5 psec. The eye height at the input and output were 9.76E-4 V and 8.57E-4 V, respectively.

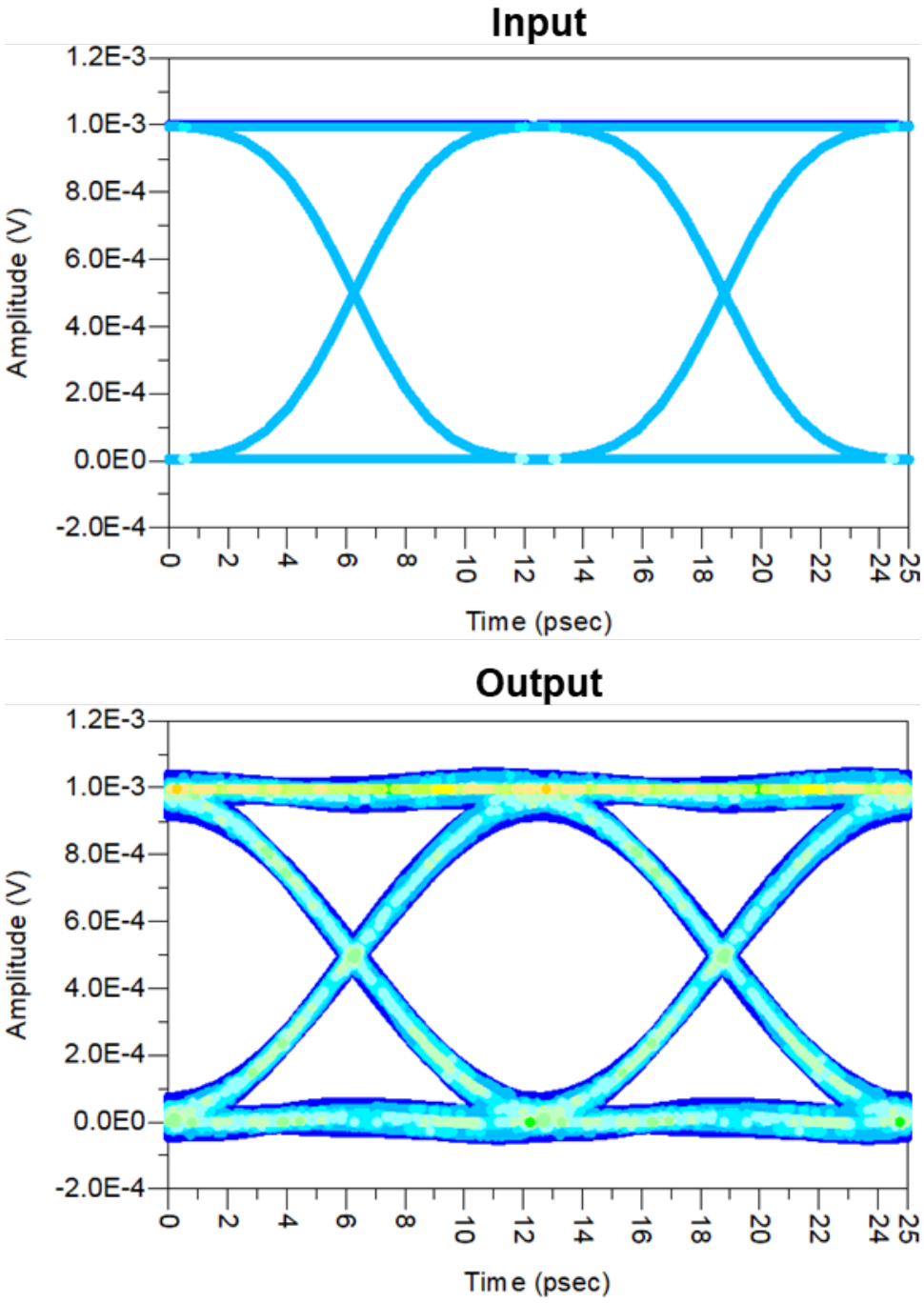

Figure 2.36: Eye diagram at the input and output of the link containing the whole assembly (11 cm stripline structure and connector region). The rise/fall time of the signal was 12.5 psec. The eye height at the input and output were 9.76E-4 V and 7.95E-4 V, respectively.

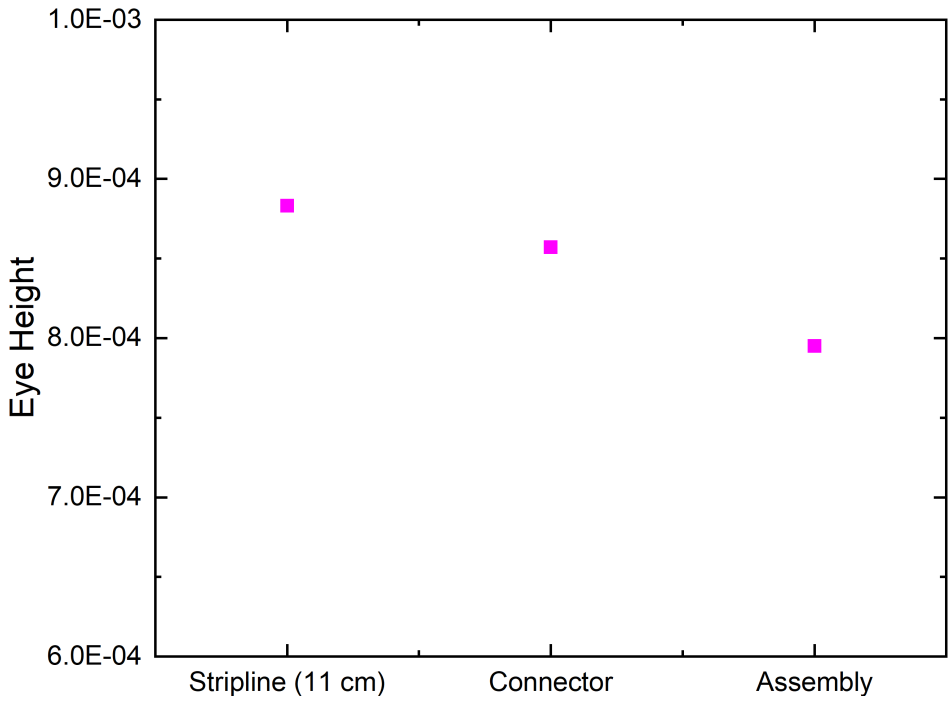

Figure 2.37: Eye height, a vertical opening of an eye diagram, in each of the cases when a stream of 1000 bits was sent at a data rate of 60 GBPS.

applications in ADS schematic was used as a source. Random bit sequences generated using Matlab were used as the input to these instances. The Matlab code used for generating the random bits is given in Appendix A. A bit sequence of 0x1x1x1x1x1x1x... where x represents padded 59 bits ('0') was given as input to all the instances. Padding 59 bits of '0' gives us desired bits for every 1 nsec when the data rate is set to 60 GBPS. To emulate the SFQ pulses usually used in quantum circuitry, an error function transition edge-shaped pulse with a specific rise and fall time was given as the input. For every '1' bit stream, the voltage source instance sends the pulse through the link. Eye measurement probes were placed at the input and output of the central line to display eye diagrams and to extract statistical eye diagram metrics such as width and height. Fig. 2.34 through Fig. 2.36 show the eye diagrams at input and output of different structures through the link.

Fig. 2.37 shows the eye height when a stream of random 1000 bits was sent through different structures. The high-quality eye diagrams indicate that the transmission line has good signal quality, with minimal distortion and noise. This suggests that the transmission

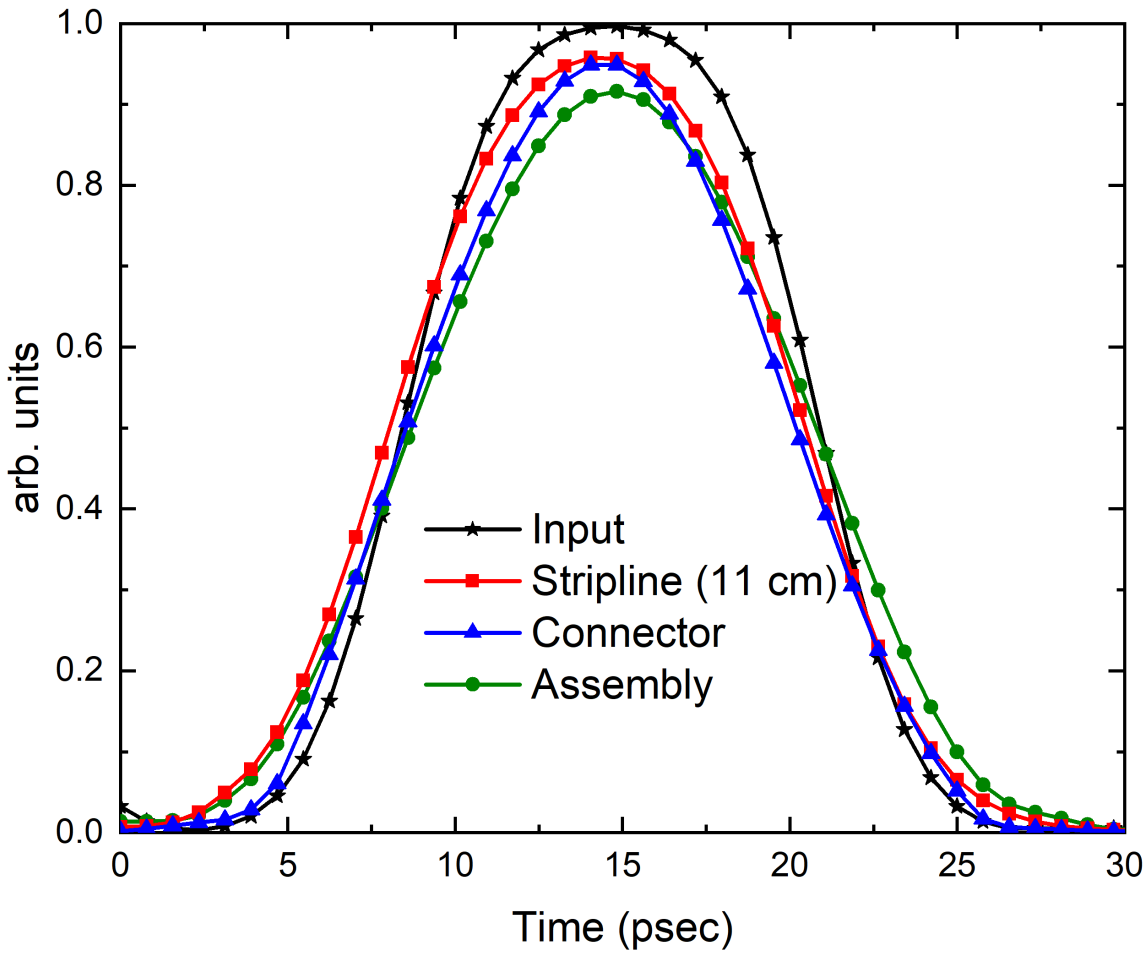

Figure 2.38: Consolidated transient analysis of a single pulse at the input and at the end of 11 cm long stripline cables, connector region, and the whole assembly. The peak of the signal at the output of an 11 cm long stripline cable is 0.956, the connector region is 0.947, and the whole assembly is 0.916. Results show low attenuation of the input signal indicating minimal signal reflections and crosstalk.

line is well-designed and properly terminated, with minimal signal reflections and crosstalk. The rise and fall times of the signals are within the acceptable range, indicating that the transmission line is capable of transmitting high-speed digital signals with minimal timing errors. Overall, the eye diagram results suggest that the transmission line is well-suited for its intended application and meets the required specifications for signal integrity. Fig. 2.38 shows the consolidated transient analysis output of a single pulse in each of the cases with respect to an input pulse.

2.3 Fabrication

2.3.1 Superconducting Flexible Cables

The cables were made up of alternating layers of patterned Nb and spin-on polyimide PI-2611. The total thickness of the fabricated stripline flex cable was $\sim$ 60 μm. Ti(50 nm)/Au(250 nm) was deposited for contact pad metallization to ensure low contact resistance such that a small normal force could be used to make good electrical contact. Based on our tolerances from the mechanical assembly, I estimate the contact area between two signal pads on the cables to be a maximum of 3.3E-8 m^2 and a minimum of 1.3E-8 m^2.

2.3.2 Alignment Structures

Bottom and top alignment pieces were built using molybdenum. Mo, being more ductile than Si which was used in our prior work, increases the robustness of the assembly and packaging processes and lowers the risk of breakage during handling and machining. Moreover, Mo has a close dimensional match to the polyimide PI-2611 when cooled from room temperature to 4.2 K, so that the connector components stay aligned. The top Mo piece contained high aspect ratio (HAR) SU-8, a commonly used epoxy-based negative photoresist, pillars to apply uniform pressure on the signal and ground contact pad areas of the stripline cables. SU-8 pillars on the top Mo piece were 250 μm tall and had a diameter of 37.5 μm with a pitch of 75 μm. A $\sim$ 4 μm thick partially cured (225 °C) HD-4100 polyimide layer was used as an interfacial layer to improve the adhesion of SU-8 pillars with the substrate. This is an important step for cryogenic applications, and test structures with this interfacial layer were found to survive multiple thermal cycles to 4 K.

The bottom alignment Mo piece contained 250 μm tall SU-8 features, which were designed to be used as mechanical self-alignment structures for the stripline ribbon cables. SU-8 features on bottom alignment pieces were larger in area and thus, had a lower aspect ratio compared to SU-8 pillars on the top alignment piece. For SU-8 features on the bottom Mo

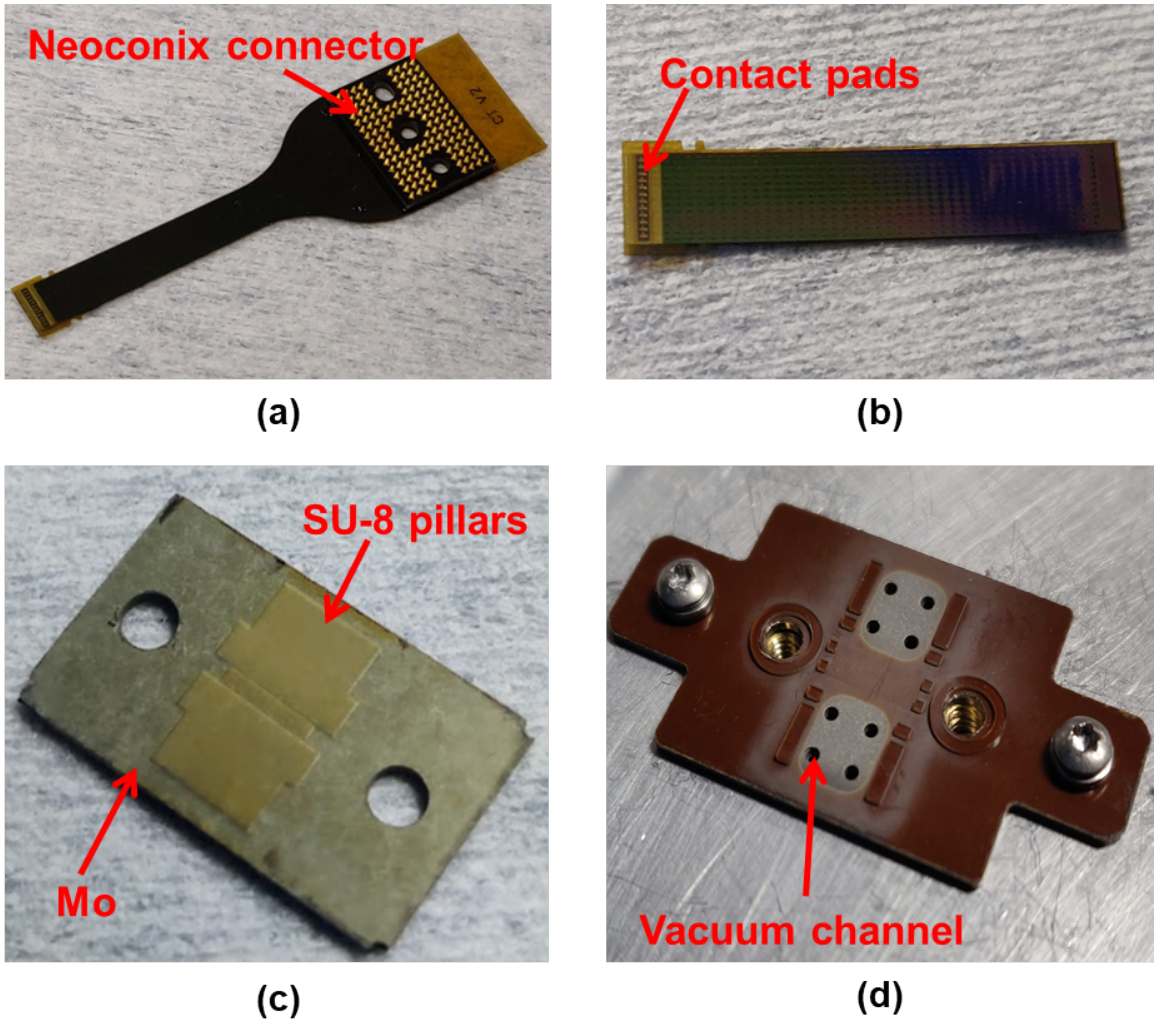

Figure 2.39: (a) Released connector tester cable with bonded Neoconix connector. (b) Released loop-back cable. (c) Top Mo piece with HAR SU-8 pillars. (d) Bottom Mo piece with SU-8 posts screwed down to a vacuum chuck.

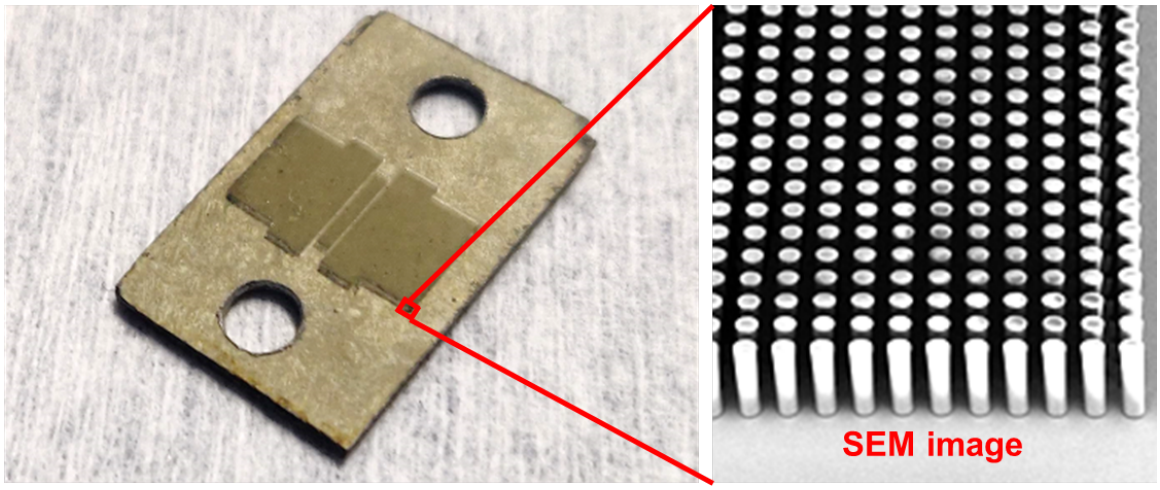

Figure 2.40: Top Mo piece and an SEM image of SU-8 pillars of one of the corners. The SU-8 pillars are 250 µm tall with a planarity of ±1 µm.

piece, ∼ 20 µm thick fully cured HD-4110 polyimide gave better adhesion than the partially cured polyimide during cryogenic reliability studies. SU-8 features (pillars) on the bottom (top) Mo pieces were defined by standard photolithography steps to achieve a nominal height of 250 µm. CNC drilling of fine features in the bottom and top Mo pieces was performed using an LPKF ProtoMat S103. After CNC drilling of the Mo pieces, Mo piece cutouts were accomplished by using laser processing.

Optical profilometry measurements showed planarity of ±1 µm for SU-8 structures. The rigidity of Mo, planarity of SU-8 pillars, and flex cables helped to exert uniform pressure in the connection region. Beryllium copper Belleville spring washers were used in the assembly to help with small dimensional changes of different assembly parts when cooled from room temperature to 4.2 K. Fig. 2.39 shows images of fabricated stripline cables, Mo pieces used in the assembly, and Fig. 2.40 shows the SEM image of the fabricated pillars on top Mo piece.

2.4 Assembly Process

For assembling the connector, a vacuum fixture containing recesses was fabricated to hold the screw nuts and two sets of vacuum channels to hold the stripline cables during

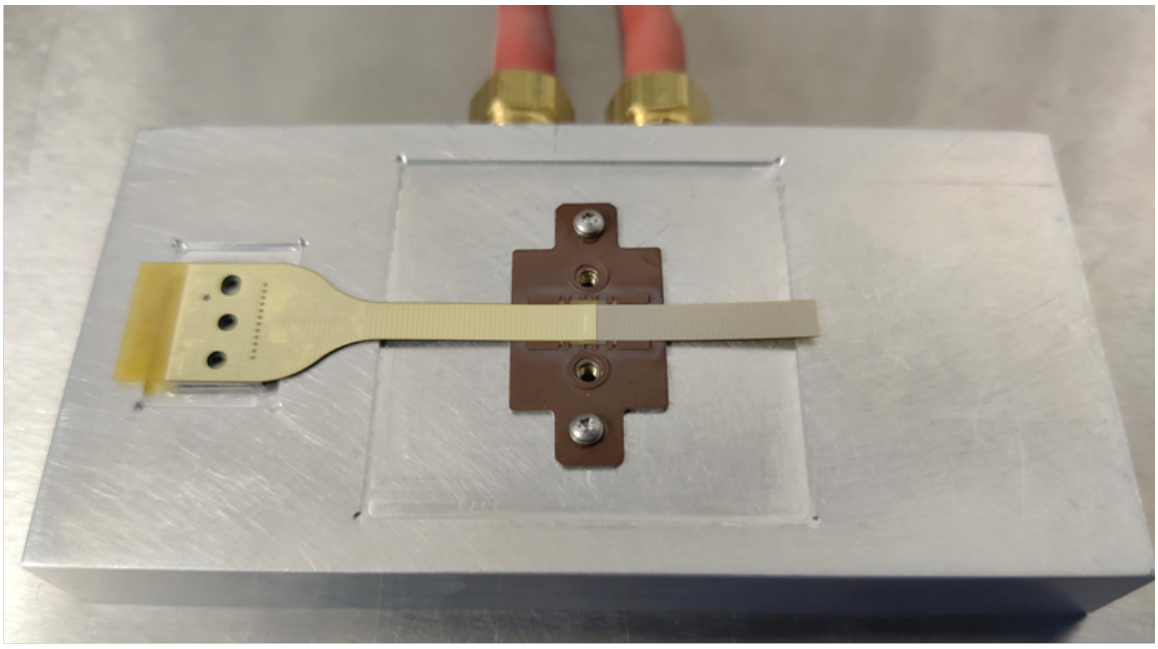

(a)

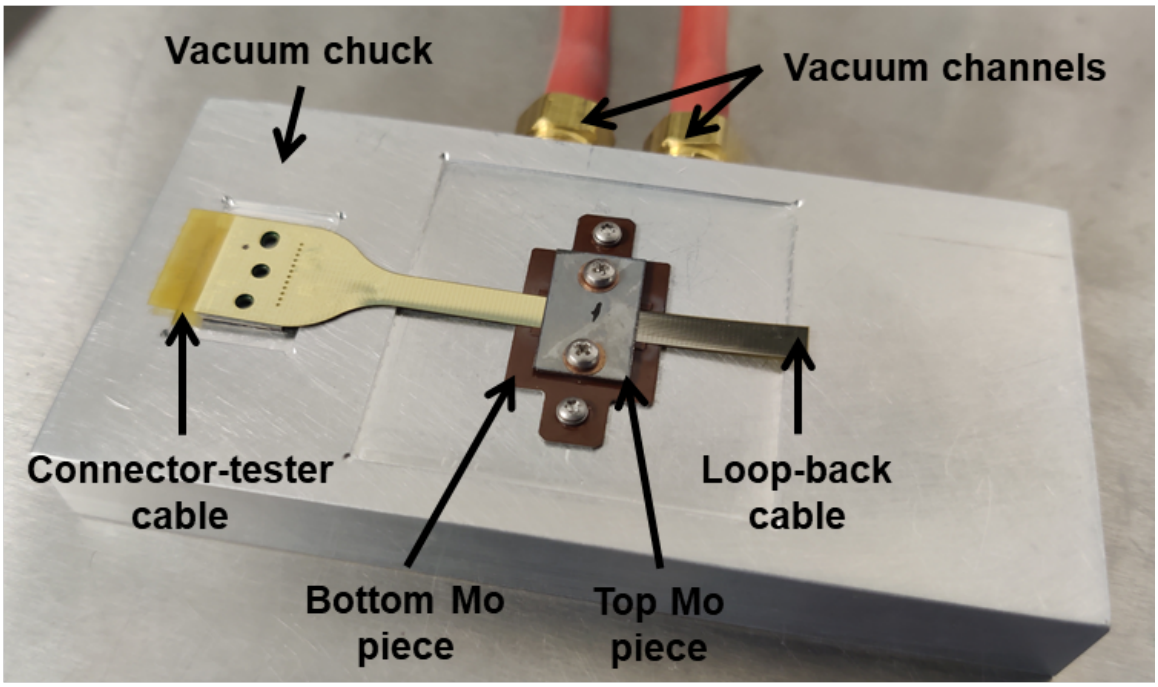

(b)

Figure 2.41: Face-to-face connector assembly (a) after aligning the CT and LB cable (b) after screwing the top Mo piece to provide optimum pressure on the contact pads

assembly. As a first step, the bottom Mo piece with SU-8 features was screwed down to the vacuum chuck. The LB cable was then placed face-up on the bottom Mo piece with the help of SU-8 alignment features, and one set of vacuum channels was turned on. The second vacuum channel set was turned on after the CT cable was placed face down, engaging additional Su-8 alignment features, ensuring that the signal and ground contact pads on both stripline cables were aligned face-to-face. Finally, a top Mo piece was placed over the CT cable with its HAR SU-8 pillars aligned between the bottom SU-8 features and pushing on the signal and ground contact areas of the cables. A digital torque wrench with a 0.6 cN.m torque setting was sufficient to hold the assembly parts in place while also not permanently damaging the SU-8 pillars. Fig. 2.41 shows the face-to-face connector scheme without and with the top Mo piece during the assembly process. This torque also applied optimum pressure on the contact pads, yielding room-temperature resistance values close to the expected values, based on the 4-point probe resistance measurement values of individual cables. Fig. 2.42 shows an assembled face-to-face connector with flexible superconducting stripline cables and alignment Mo pieces.

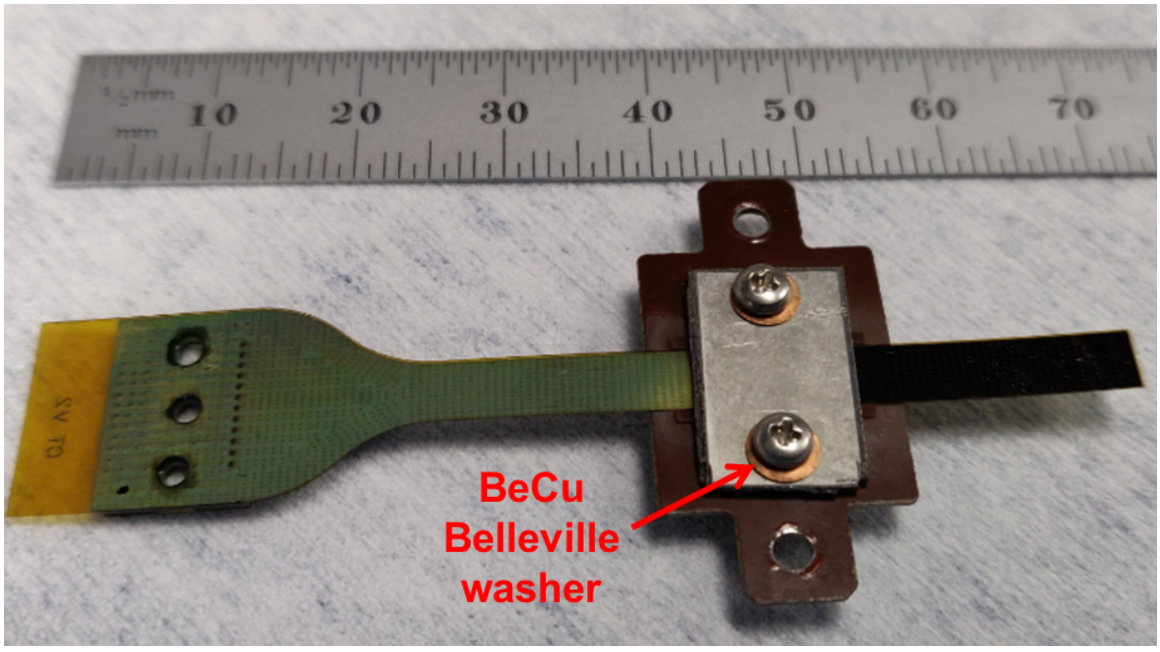

Figure 2.42: Assembled face-to-face connector with flexible superconducting stripline cables and alignment Mo pieces and an SEM image of SU-8 pillars on the top left corner.

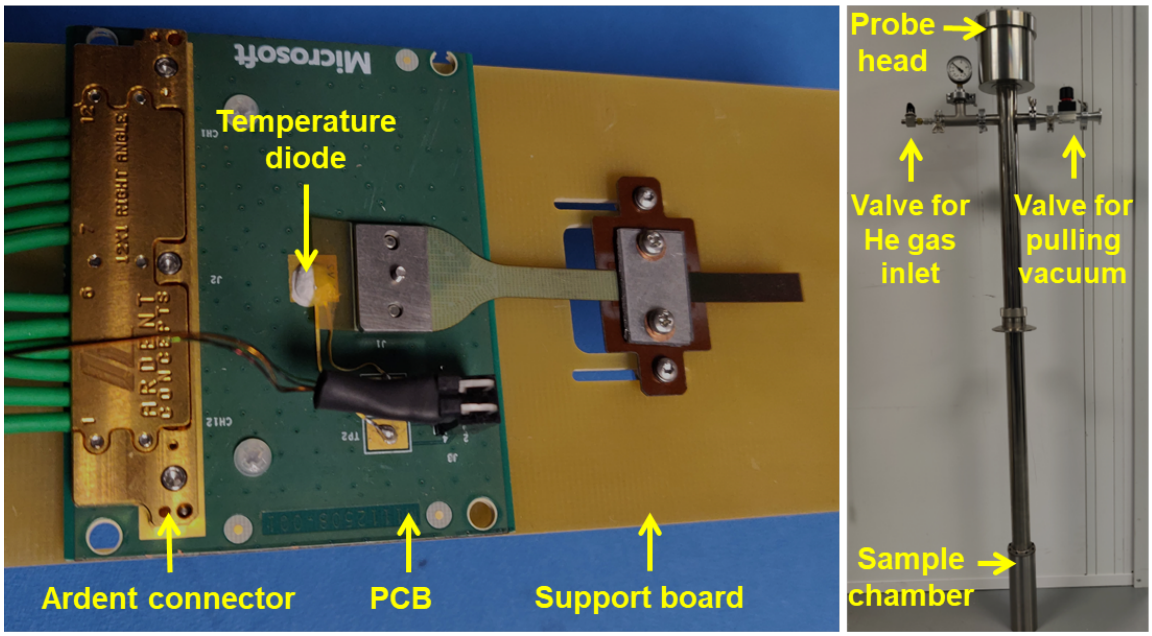

Figure 2.43: Measurement set-up board showing mounted face-to-face cable connector assembly and dip probe used for measurements from room temperature to 4.2 K.

2.5 Measurement Details

Fig. 2.43 shows the measurement setup inside the sample chamber of a liquid helium (LHe) dip (immersion) probe, which was used for carrying out measurements from room temperature to 4.2 K. A printed circuit board (PCB) with a commercial connector footprint was mounted onto a mechanical support board with lateral adjustment grooves to offer a mechanism to sustain assemblies of varying lengths. The Neoconix connector (bonded to the CT cable) was connected to the PCB using the recommended screw and torque. The support board also consisted of adjustment grooves for screwing the bottom Mo piece to avoid any damage to the assembly during measurements. The temperature of the assembly was measured using a temperature diode cemented to the middle of the PCB and monitored using a Lake Shore Model 224 temperature monitor. A high-density high-speed multi-coax connector from Ardent Concepts was used to interface the PCB and RF cables. A can attached over the end of the dip probe was used to seal the assembly and carry out the measurements from room temperature to cryogenic temperatures. The dip probe was installed with two valves,

one for pulling the vacuum and the other for introducing He exchange gas. The probe was filled with He gas at room temperature and was immersed into liquid nitrogen to carry out the measurements from ambient temperature to approximately 80 K, and then into LHe for measurements from 80 K to 4.2 K. Critical current measurements were performed at 4.2 K in LHe, using a Keithley 2400 source meter, by sweeping current (increasing from zero) and sensing the voltage. A compliance voltage of 2 V was set to protect the samples, and resistance was calculated based on the measured voltage. Each line's DC resistance was also measured using a Keithley 2400 source measure unit with a steady test current of 1 mA in separate temperature cycles, i.e., six different cool-downs to 4.2 K were performed in order to acquire the critical transition temperature of each line pair. For RF measurements, due to calibration challenges at cryogenic temperatures, I employed time-domain reflectometry to locate and characterize discontinuities in electrical paths, such as at a connector or along a trace on a PCB. Time-domain measurements were carried out using Keysight Performance Network Analyzer (PNA) N5227A controlled by Physical Layer Test System (PLTS) software, with a rise time of 18 ps and an output power of -20 dBm from the PNA.

2.6 Results and Discussion

The face-to-face connector scheme was assembled using 0.6 cN.m torque value and the 4-point probe resistance measurement values of each line in the assembly were in the range of 1 to 3% of expected values. The DC and time-domain properties of the assembly are discussed in the following sections.

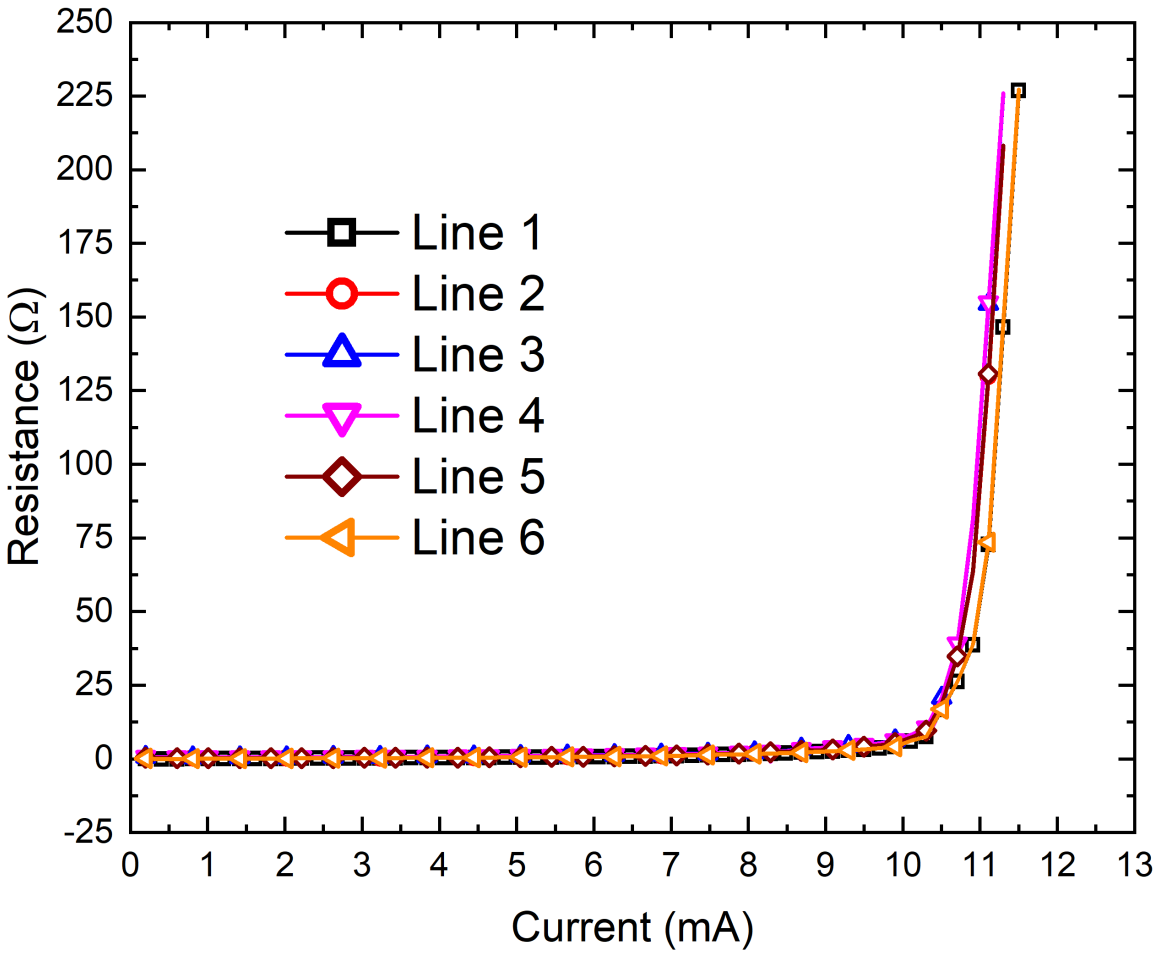

Figure 2.44: Resistance vs. current for all 12 face-to-face signal contacts with loop-backs resulting in 6 testable signal lines of the assembled test structure at 4.2 K.

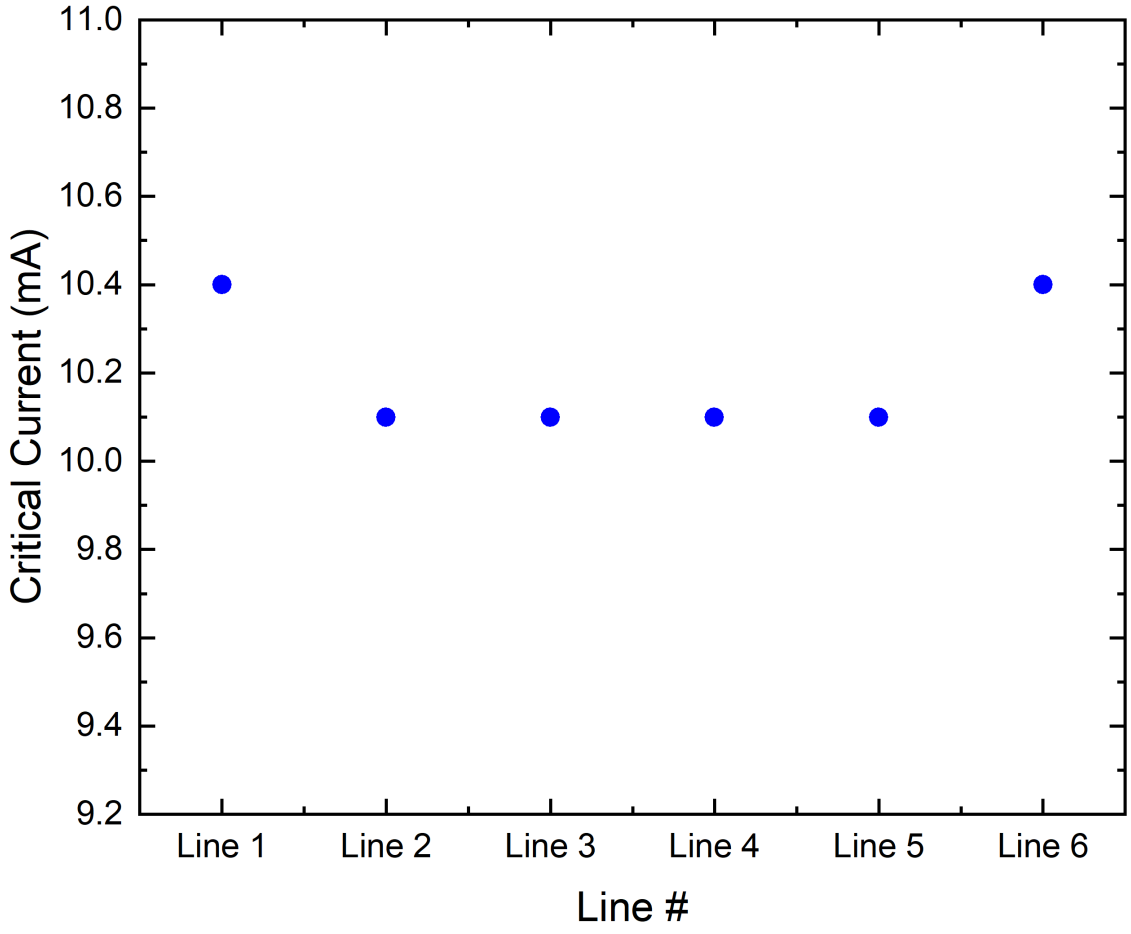

Figure 2.45: Plot shows the measured critical current values of all the six testable lines in the assembly. An average critical current level of at least 10 mA can be observed.

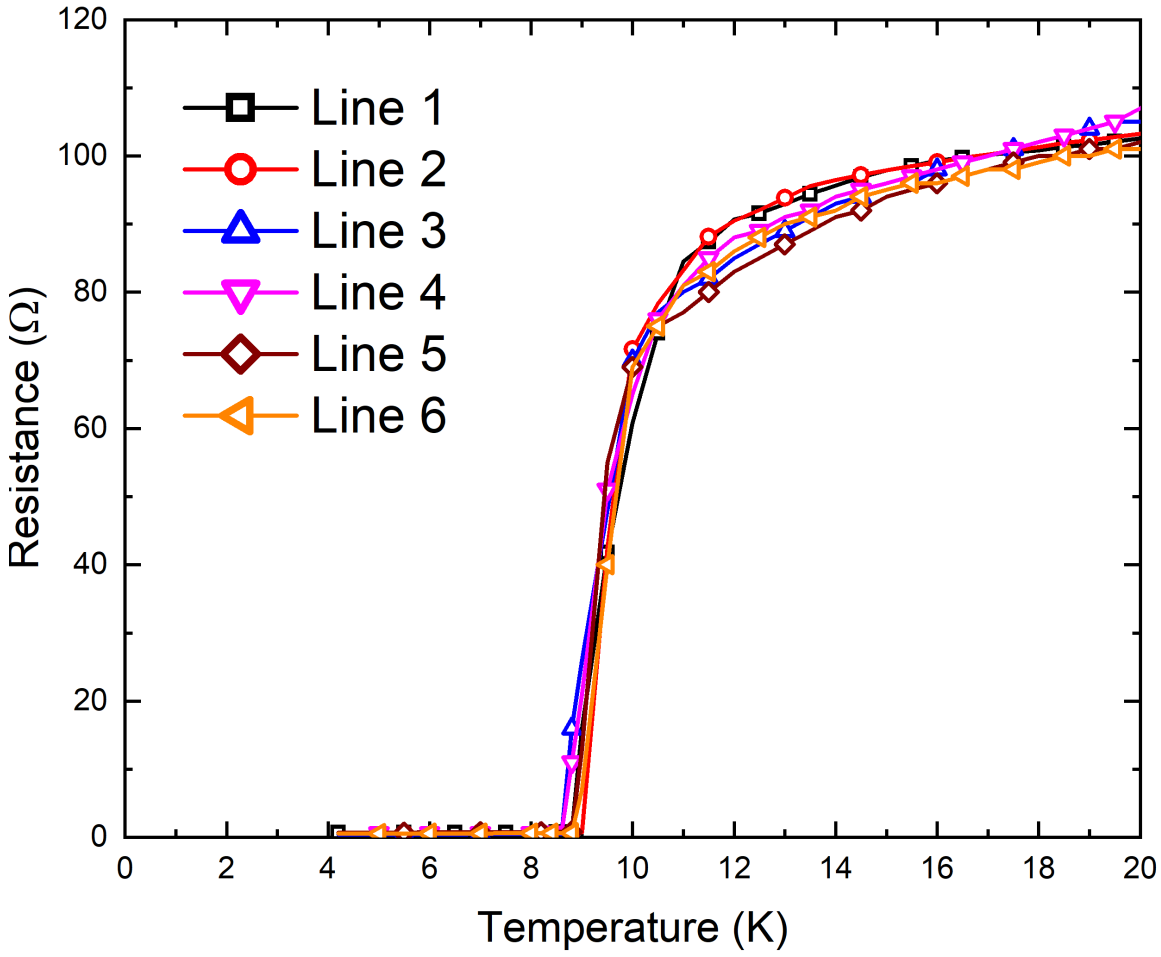

Figure 2.46: DC resistances vs. temperature for all 12 face-to-face signal contacts with loop-backs resulting in 6 testable signal lines of fully assembled test structure from 20 K to 4.2 K using 1 mA test current. Lines were measured individually during separate cool-downs and the immersion probe can was not unsealed between cool-downs.

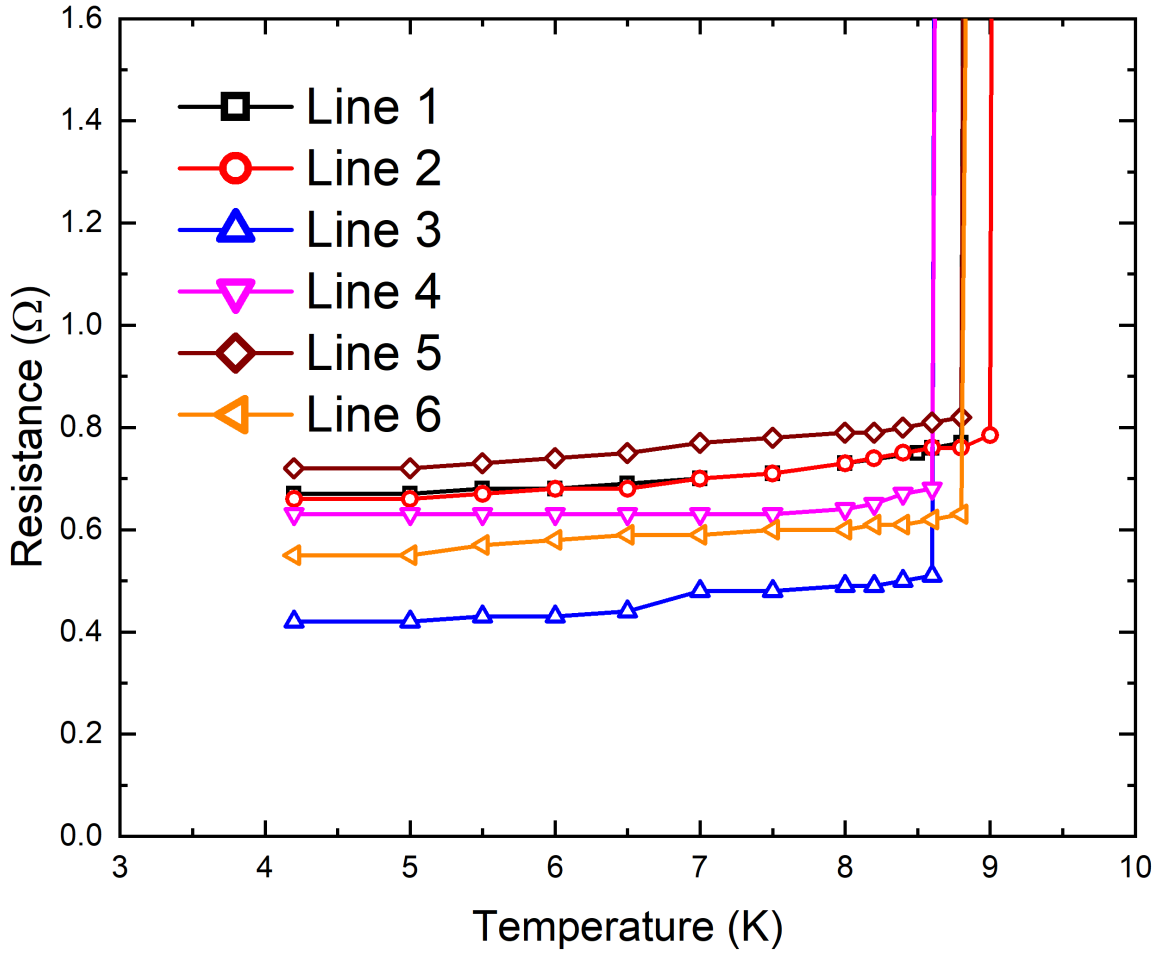

Figure 2.47: DC resistances vs. temperature of each testable line in the assembly when the traces on the flex cables were in a superconducting state.

2.6.1 DC Properties

DC resistance characterization measurements were performed as described in the previous section. Fig. 2.44 shows resistance versus current for all 12 face-to-face signal contacts with loop-backs resulting in 6 testable signal lines of the assembled test structure at 4.2 K. The measurements showed an average critical current of atleast 10 mA for the six testable lines. Fig. 2.46 shows the resistance versus temperature of all 6 testable signal lines in the assembly. Fig. 2.47 shows the resistance versus temperature when all the lines are superconducting highlighting the residual resistance in each line. DC resistance of each line was measured using a Keithley 2400 source measure unit where the test current was kept constant

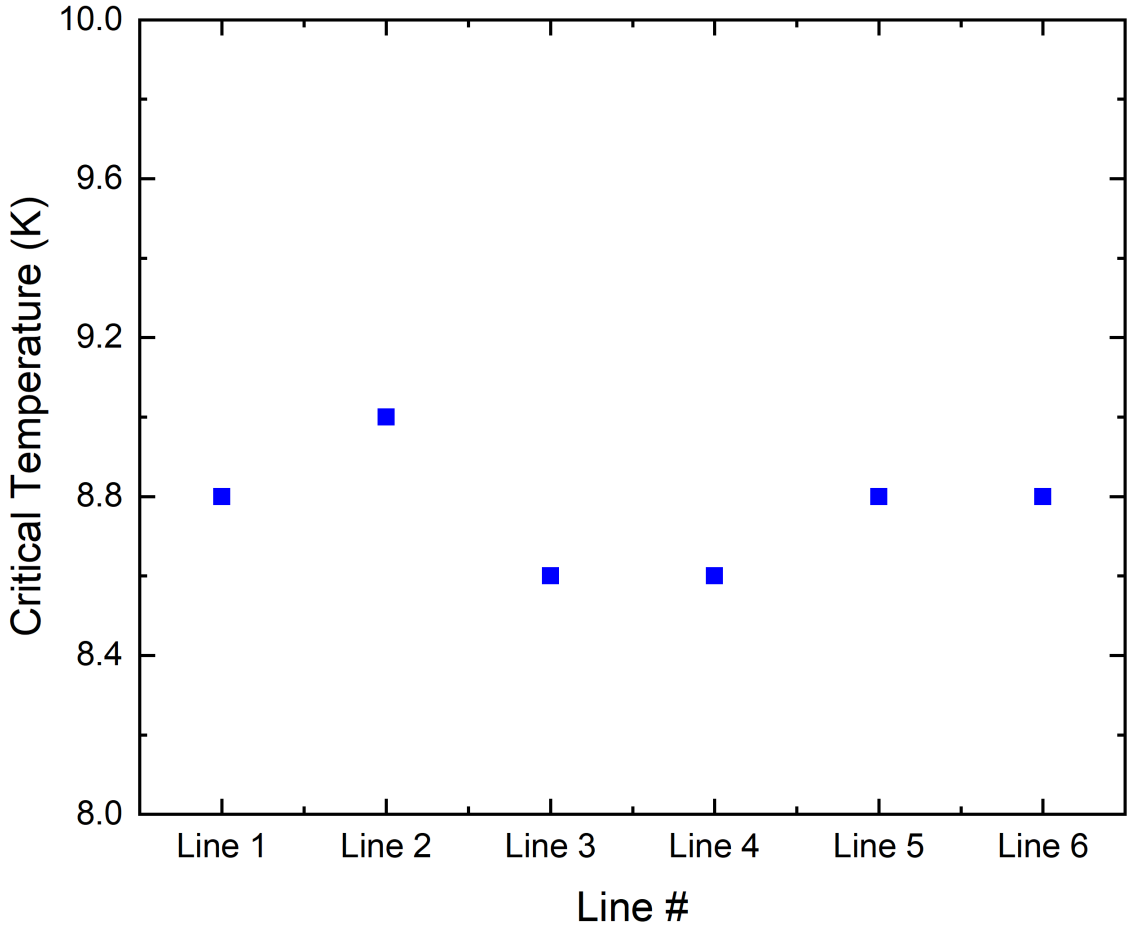

Figure 2.48: Plot shows the measured critical temperature values of all the six testable lines in the assembly.

Table 2.2: Critical Currents and Critical Temperatures of 6 Testable Signal Lines in the Assembly Resulting From 12 Face-to-face signal contacts with loop-backs.

Line number	Critical current (mA)	Critical temperature (K)
1	10.4	8.8
2	10.1	9.0
3	10.1	8.6
4	10.1	8.6
5	10.1	8.8
6	10.4	8.8

at 1 mA, much below the lowest critical current of around 10 mA. The total resistance of the assembly when the traces on the flex cables were in a superconducting state was in the range of 400-750 mΩ. A portion of this resistance is attributed to Neoconix connector resistance and contact resistance of Neoconix SAC-In bumps on the tape. This combined resistance was measured to be in the range of 220-320 mΩ. The contact resistance of face-to-face cables in the connection region, which includes a segment of normal metal (Ti/Au) resistance was calculated to be in the range of 90-215 mΩ per contact. The measured critical transition temperatures were in the range of 8.6-9.0 K. Table 2.2 shows the measured critical current and critical transition temperature of each testable line in the assembly.

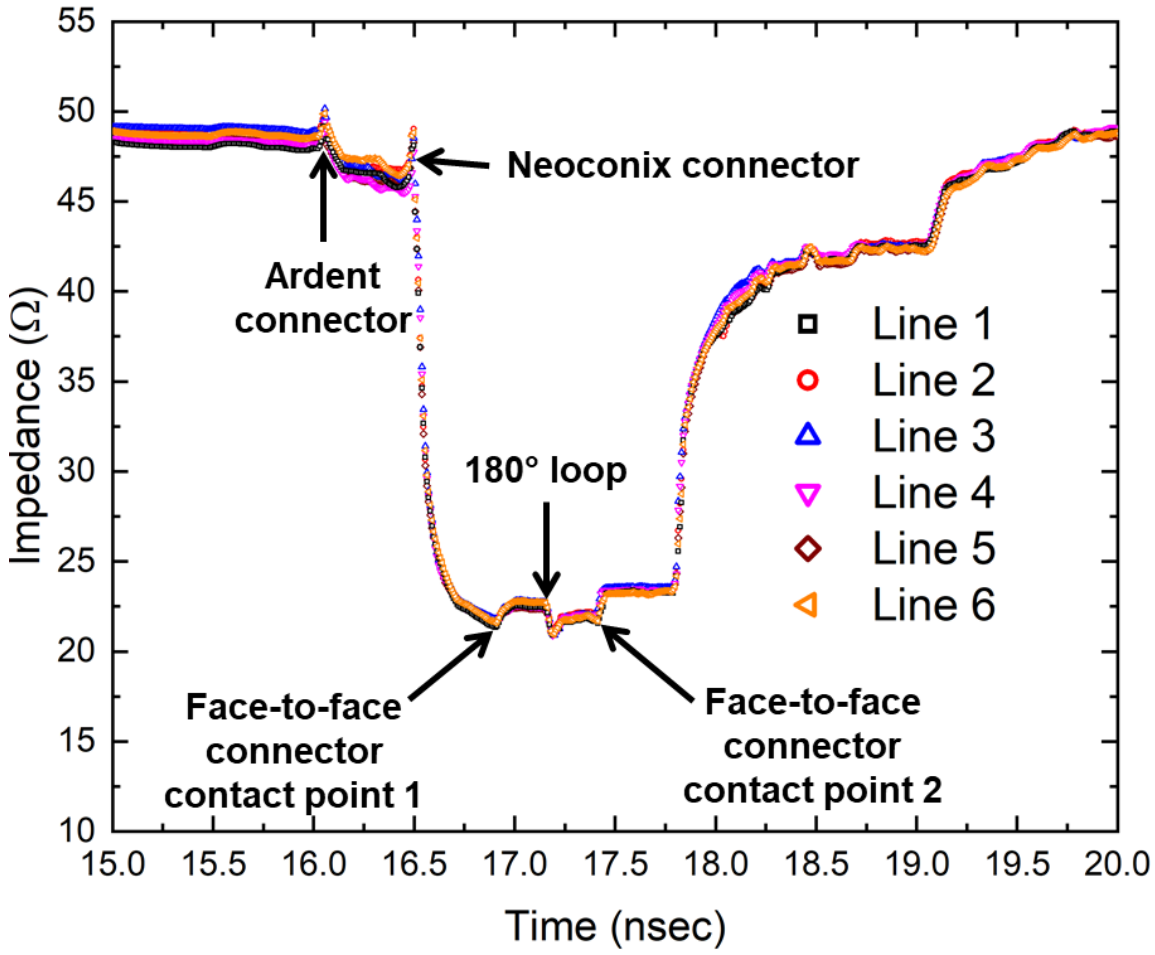

Figure 2.49: Time-domain reflectometry measurement results for all 12 face-to-face signal contacts with loop-backs resulting in 6 testable signal lines in the assembly at 4.2 K. The two impedance jumps in the plot, at $\sim$ 16.9 ns and $\sim$ 17.4 ns, correspond to the signal contact points of the assembled lines and the 180° bends on the signal lines of the LB cable show a capacitive response at $\sim$ 17.15 ns.

2.6.2 Time-domain Properties

Fig. 2.49 shows the acquired TDR measurements of all six intact lines. Measurements were carried out in an evacuated cryogenic environment using a PNA controlled by PLTS software. The two impedance jumps in the plot, at $\sim$ 16.9 ns and $\sim$ 17.4 ns, correspond to the signal contact points of the assembled lines and the 180° bends on the signal lines of LB cable show capacitive response at $\sim$ 17.15 ns. The slightly higher overall impedance of the connector assembly can be attributed to the long test cables running from the top of the probe to the sample chamber. Conductor loss in these cables, which is caused by metal conductors' finite resistance, increases with frequency, giving the impression of higher DUT impedance than it actually is.

Keysight PathWave ADS circuit design simulations were performed to match the measurements by accurately modeling different components in the assembly. Fig. 2.50 shows the ADS schematic circuit modeling of CT cable, LB cable, and interconnect region. All the dimensions in the model were obtained from physical measurements and PI-2611 dielectric properties are based on [49]. The coupled stripline traces on CT and LB cable were divided into multiple sections of 0.5 mm unit length, which is shorter than 1/10 of the wavelength at the highest frequency ($\sim$ 56 GHz) corresponding to signal rise time. Each coupled section consisted of a series inductor L_k, corresponding to the kinetic inductance of the Nb superconductor. R_c and C_c located at the CT-LB contact regions were used to represent the contact resistance and distributed shunt capacitance at contact points due to wider contact pad width (100 μm). Another shunt capacitance C_{cp} was added at the 180° bend in the LB traces to match the capacitive reflection. This capacitive response can be due to the mutual coupling at 180° bend and increase in current density on the edge of the loop. Simulation with parameter values for extracted L_k of 10 pH, R_c of 850 mΩ, C_c of 40 fF, and C_{cp} of 0.15 pF exhibited a close match to the measurement results. The kinetic inductance of unit length for the outbound signal trace on the LB cable had to be adjusted to 9 pH to match the measurement results. Fig. 2.51 shows the TDR response of all 6 testable lines in the

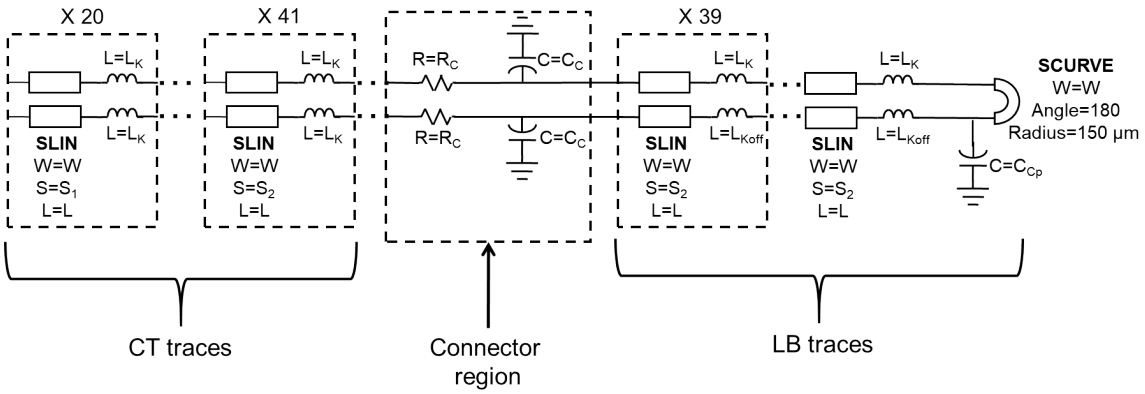

Figure 2.50: Equivalent distributed stripline circuit model near the interconnect region of face-to-face assembly is shown. SLIN is a coupled stripline element unit with line length and width values of L=0.5 mm and W=86.2 µm, respectively. The coupling gap $S_1 = 663.6$ µm and $S_2 = 225.6$ µm. The kinetic inductance (L_k) of Nb per unit element was determined to be 10 pH in the simulation. Contact resistance (R_c) = 850 mΩ, contact pad capacitance (C_c) = 40 fF and mutual coupling capacitance at the 180° bend (C_{cp}) = 0.15 pF. Note that the kinetic inductance of outbound traces on LB cable (L_{koff}) = 9 pH was simulated with a lower value than L_k to match the measurements.

connector region and ADS schematic simulation results. Using a simple model, a reasonable agreement between measurements and simulations in the connector region was achieved.

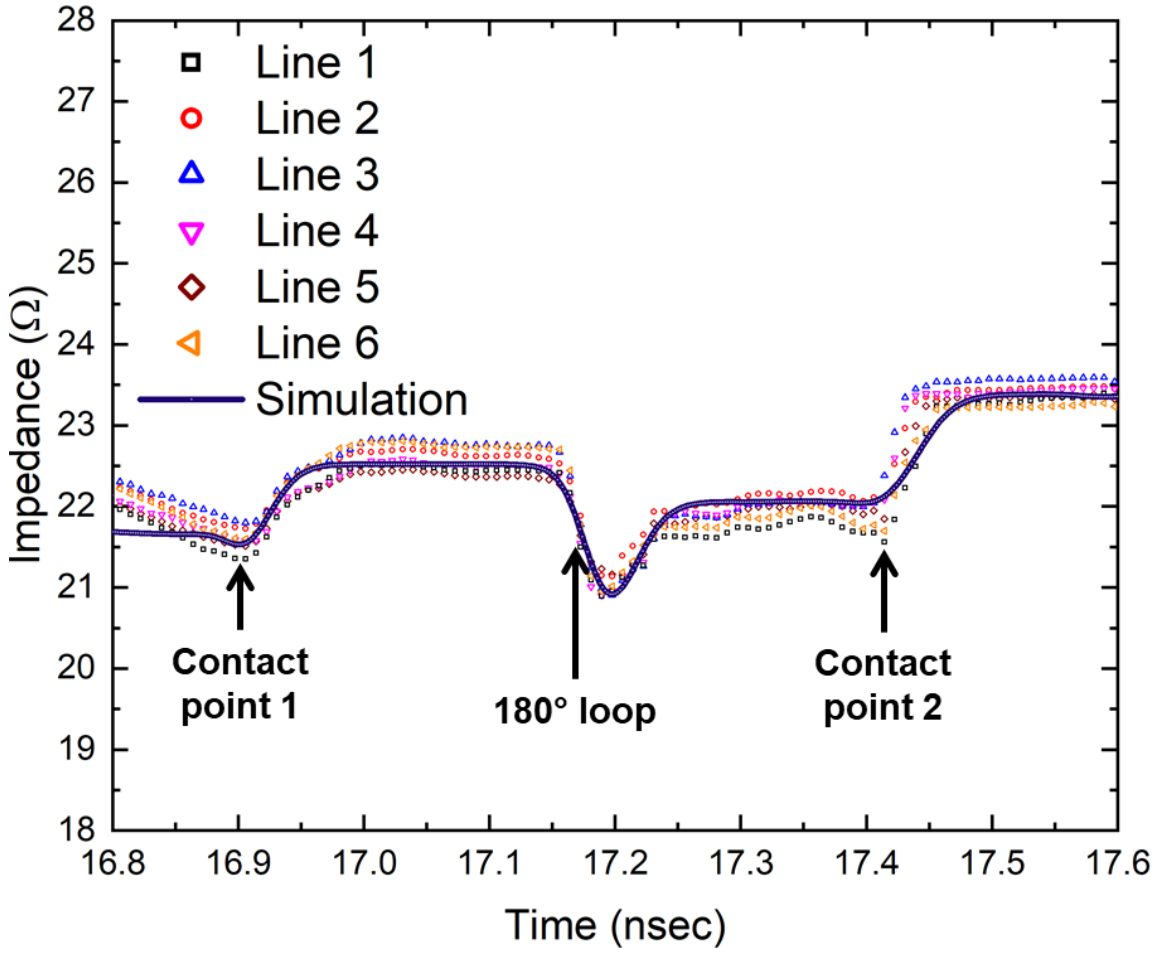

Figure 2.51: Time-domain reflectometry measurement results for all 6 testable signal lines at the connector region at 4.2 K along with ADS schematic simulation results. A reasonable agreement between measurements and simulations in the connector region was achieved. The power dependency measurements on all six testable lines yielded similar results.

2.6.3 Microwave power dependence

Face-to-face connector microwave power-dependence tests were performed on the assembly at 4.2 K. Fig. 2.52 shows the TDR response of line 1 in the assembly measured with different PNA output power settings of -20 dBm, -10 dBm, and 0 dBm. During these power dependence measurements, the assembly was tested without any disassembly or re-assembly. From the plot, it's evident that the TDR responses are relatively consistent, and minimal power dependency was observed within the measurement errors and over the tested range from -20 to 0 dBm PNA output power levels. Similar responses were recorded with all the other five testable lines in the assembly with different input power from the PNA.

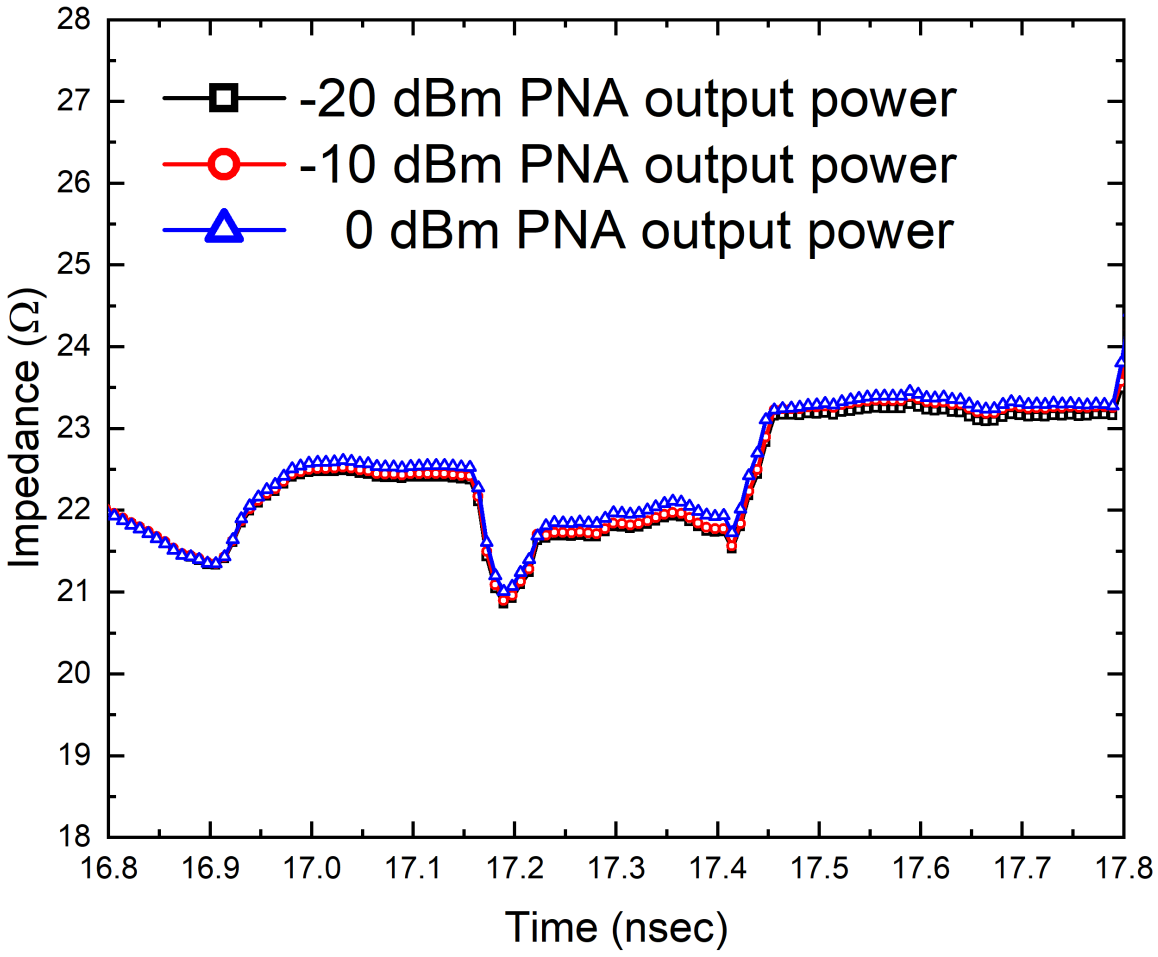

Figure 2.52: Time-domain reflectometry response of line 1 with different output power (-20 dBm, -10 dBm, and 0 dBm) from the network analyzer. Minimal microwave power dependency was observed. Similar responses were recorded with all the other five testable lines in the assembly with different input power from the PNA.

2.7 Summary

The face-to-face cable connection scheme between flexible thin-film superconducting stripline cables was successfully described and demonstrated. The transition of all traces on the flexible cables to a superconducting state within a critical temperature range of 8.6-9.0 K signifies the effectiveness of the superconducting materials employed in the assembly. Measurements conducted to determine the critical current of the face-to-face signal contacts showed an average value in the range of 10-10.5 mA for all 12 face-to-face signal contacts with loop-backs resulting in six testable signal lines in the assembly. This indicates that the superconducting stripline cables are capable of carrying current without significant resistance, thereby minimizing power loss and maintaining the integrity of the transmitted signals. Time-domain reflectometry measurements performed at a temperature of 4.2 K revealed an average impedance jump of 1 Ω at the signal contact points. This low impedance jump indicates a smooth and effective transition between the face-to-face signal contacts, minimizing signal reflections and preserving the integrity of the transmitted signals. Furthermore, the lines exhibited minimal microwave power dependency, ensuring stable signal characteristics even with varying power levels.

The experimental results obtained from this study using a face-to-face connection scheme, utilizing thin and flexible superconducting stripline cables, offers the potential for high-density signal integration without compromising signal integrity. The successful transition of the traces to a superconducting state, combined with the measured critical current values and impedance characteristics, indicates the suitability of this approach for demanding applications in cryogenic and quantum technologies.

The demonstrated transition to a superconducting state, the measured critical current values, and the impedance characteristics provide a solid foundation for future research and development in this field. This approach holds great potential for enabling advanced signal transmission in low-temperature environments, contributing to the advancement of cryogenic and quantum technologies.

Chapter 3

Investigating the Impact of Gamma Radiation on Superconducting Microstrip Resonators

3.1 Introduction

Cryogenic temperatures present unique challenges for signal integrity in electronic systems, necessitating a comprehensive understanding of device behavior under extreme conditions. This chapter of the dissertation explores the effects of gamma radiation on superconducting microstrip resonators, with a specific emphasis on quantifying changes in their Q values before and after exposure.

Superconducting microstrip resonators have emerged as promising candidates for various applications due to their compactness, scalability, and high Q values. These resonators, based on the principles of superconductivity, exhibit zero electrical resistance below a critical temperature, making them ideal for low-loss transmission of high-frequency signals. However, their performance can be affected by external factors, including radiation exposure.

Gamma radiation, an ionizing form of radiation encountered in several real-world scenarios, poses a significant challenge to the reliable operation of cryogenic systems. With applications in space missions, nuclear facilities, and medical imaging, understanding the impact of gamma radiation on superconducting microstrip resonators is crucial for designing resilient cryogenic systems capable of withstanding radiation exposure.

Previous experiments on the influence of gamma rays on superconducting properties have been reported in [61, 62, 63, 64, 65]. Gamma-ray exposure up to a cumulative dose of 1.5 Mrad had small to no impact on the critical temperature and critical current density of thin superconducting films [66]. Polyimide (PI) films provide reasonable mechanical strength and flexibility with excellent dielectric properties, thermal stability, and chemical resistance [67, 68]. PI has been used as a component of satellite exteriors for many years because

of their excellent thermal insulator properties, which provide stable operating temperature ranges for satellite systems. They also provide good shielding for the electrical and electronic components from the space environment through which the spacecraft travels [69, 70, 71, 72].

The primary objective of this chapter is to investigate the influence of gamma radiation on the Q values of superconducting microstrip resonators. By subjecting these resonators to controlled gamma radiation and comparing their performance before and after exposure, we can evaluate the extent to which radiation affects their quality factors. This research contributes to the broader understanding of the behavior of superconducting devices in cryogenic environments and provides insights into their suitability for radiation-intensive applications.

The findings presented in this chapter have implications for both the specific domain of superconducting microstrip resonators and the broader field of cryogenic electronics. The results contribute to the body of knowledge surrounding the behavior of superconducting devices under challenging conditions, providing guidance for the design and operation of robust cryogenic systems. Furthermore, the insights gained from this research can inform the development of signal integrity solutions, advancing the frontiers of high-speed digital systems in extreme environments.

In summary, this chapter focuses on investigating the impact of gamma radiation on superconducting microstrip resonators within the context of signal integrity challenges at cryogenic temperatures. By quantifying changes in the resonator Q values following radiation exposure, this research contributes to our understanding of the behavior of these devices under extreme conditions and provides valuable insights for the design and operation of reliable cryogenic systems.

3.2 Design and Fabrication

I used half-wavelength capacitively coupled "through-type" embedded microstrip transmission line resonators that were designed and fabricated similarly to those in our previous

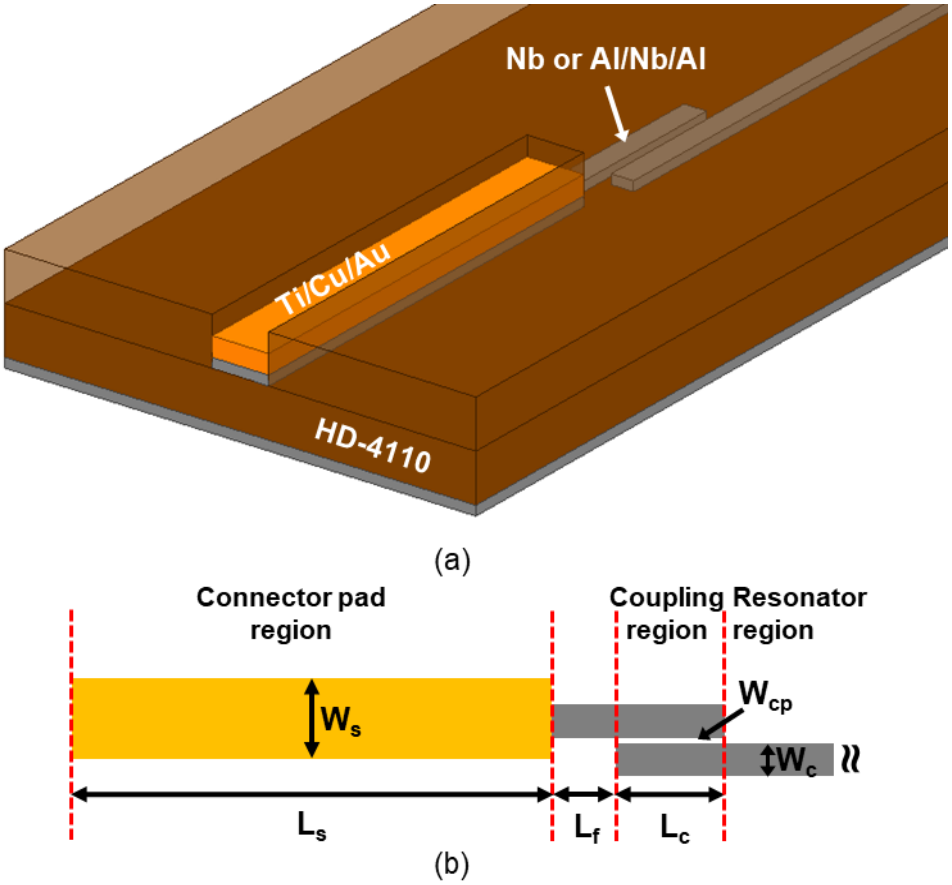

Figure 3.1: (a) 3D design view of one end of the through-type microwave transmission line resonator used in this work. (b) Top view of coupling region cross-section of connector attachment and resonator coupling region with dimensions corresponding to $L_s = 1200$ μm, $W_s = 120$ μm, $L_f = 100$ μm, $L_c = 300$ μm, $W_c = 47.4$ μm and $W_{cp} = 20$ μm.

work [73, 74, 75]. The width of these thin transmission line resonators was designed for a 50 Ω characteristic impedance. Two different metals Nb, Al/Nb/Al were chosen for these tests. Fabrication of these resonators started with the deposition of 25 nm thick Cr and 200 nm thick Al as a sacrificial layer on a couple of oxidized silicon wafers, which act as temporary substrates during fabrication. HD-4110 polyimide from HD Microsystems was spin-coated and cured at 375 °C in a nitrogen ambient environment for one hour to obtain an approximate thickness of 20 μm. A conventional photolithography lift-off process was used to define the signal lines on top of the cured polyimide. Two different conductor stack-ups were used, one for each wafer. On one of the wafers, 250 nm thick Nb was deposited as the signal trace whereas on the other wafer, Al(20 nm)/Nb(250 nm)/Al(20 nm) was deposited as the signal trace [76]. Separate runs were performed in order to deposit the signal layer on each wafer. A brief Ti gettering process step was performed prior to Nb sputtering (dc sputter for 30 min and Ar pressure of 4 mTorr [77]) while the wafers were hidden behind a shield in a CHA Mark 50 deposition system. The wafers were then patterned for connector contact metallization, and then Ti(50 nm)/Cu(500 nm)/Au(10 nm) was deposited, followed by lift-off.

Kapton dots were placed on the connector contact metallization area before spinning the second layer of polyimide on the embedded version samples and were removed before curing. The final thickness of the encapsulation layer was approximately 20 μm. The samples were then protected with photoresist and released in a salt solution with 0.5 V applied to the Cr/Al release layer. After stripping the photoresist, released tapes were flipped and mounted onto a clean Si wafer to allow the deposition of a 250 nm thick Nb ground plane layer. Fig. 3.1 shows a 3D design view of one end of the resonator used in this work, a top view of the coupling region cross-section. Fig. 3.2 shows a schematic drawing of the steps involved in the fabrication of embedded microstrip transmission line resonators fabricated using HD-4110 polyimide.

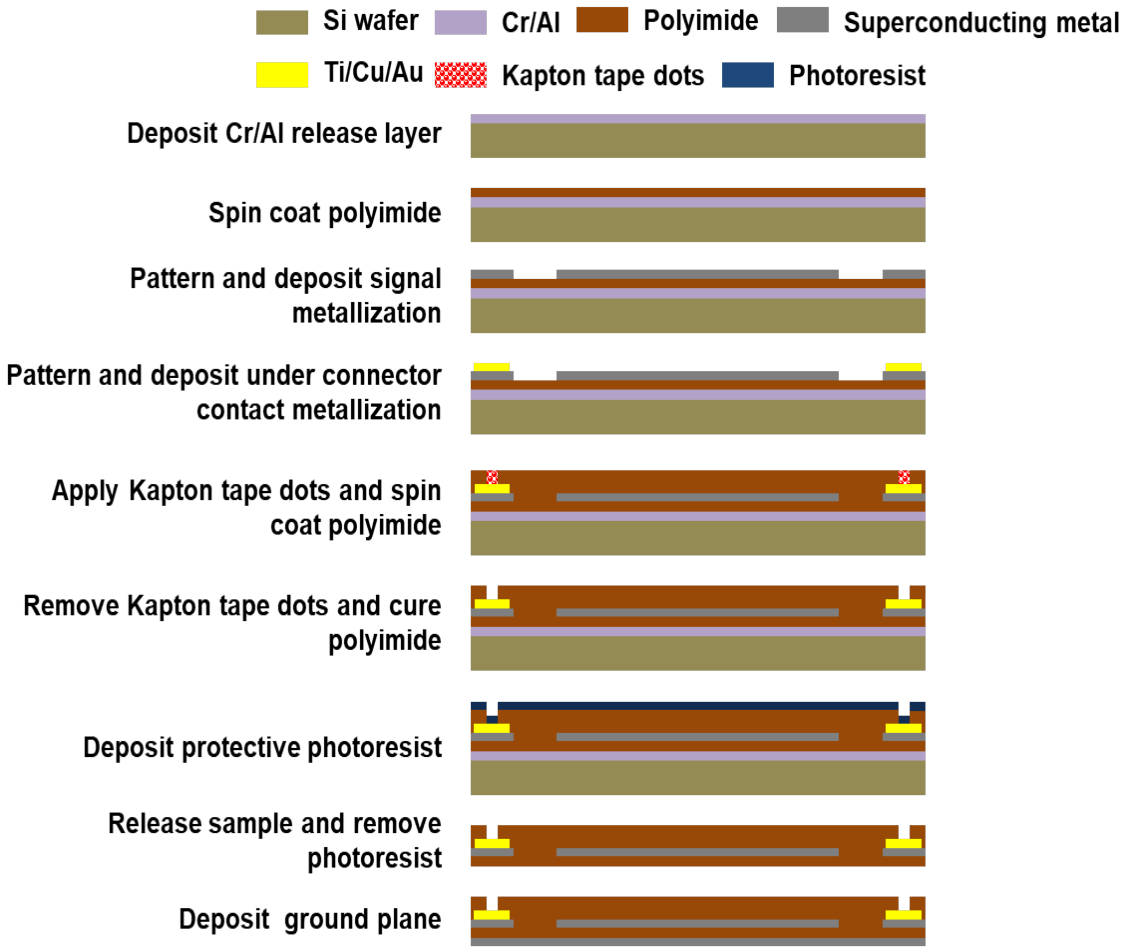

Figure 3.2: Schematic fabrication flow diagram for thin film superconducting Nb and Al/Nb/Al microstrip transmission line resonators.

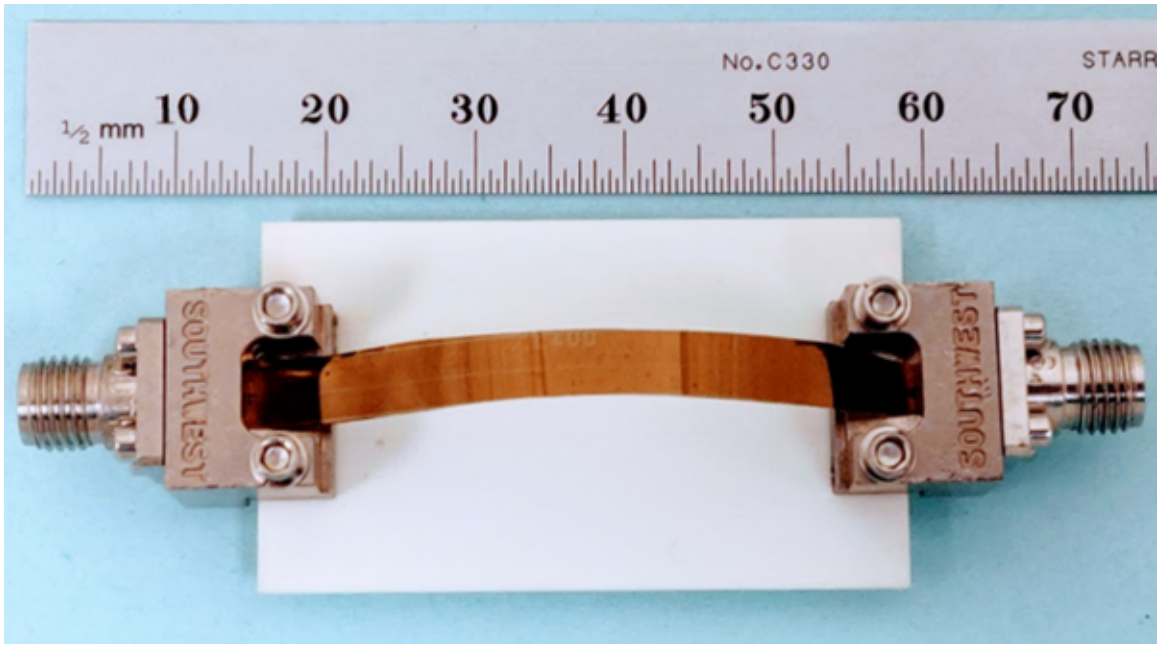

Figure 3.3: Assembled resonator sample with edge launch SMA connectors and support board.

3.3 Assembly and Measurement

Southwest Microwave's edge launch Subminiature version A (SMA) connectors were used to assemble the resonator samples. Assembled resonators were mounted onto a support board to stabilize the sample for mounting within the test setup and prevent possible damage to the thin flexible cables from the heavy connectors. Fig. 3.3 shows the resonator sample with edge launch SMA connectors and support board. Fig. 3.4 shows the cryogenic probe used for measurements inside a pulse-tube based close-cycle cryostat. The microwave performance of polyimide films is known to be affected by the water content within the film, for example when exposed to humid conditions. Previously, measurements of microwave resonators exposed to high humidity showed a shift in resonance frequencies and a decrease in quality factors at cryogenic temperatures below 4.0 K [78]. To reduce humidity effects below detectable levels and to ensure repeatability of the measured Q's and the resonance frequencies, the samples were baked at 90 °C for one hour in a vacuum oven. The measurements at various cryogenic temperatures were performed in a pulse-tube based closed-cycle cryostat. Cryogenic

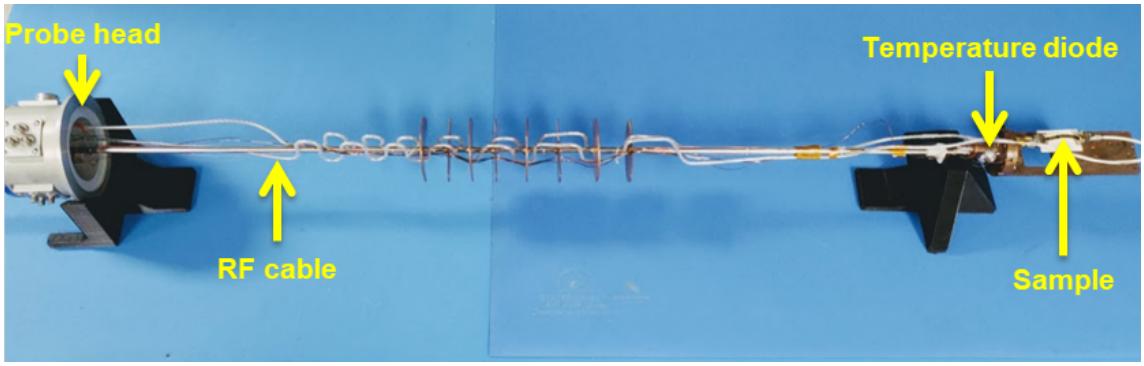

Figure 3.4: Cryogenic sample probe with resonator sample and RF coaxial cables used for measurements.

semi-rigid RF coaxial cables were used to interface the sample through the edge launch connectors. A temperature diode located on the sample holder was used to measure the sample temperature. A Keysight N5227A performance network analyzer was used to measure the scattering parameters within a sufficient range of frequencies around the resonant peaks. Fig. 3.5 shows the block diagram of the measurement set-up. Previous work on similar resonators showed quality factor reduction and nonlinearities for microwave powers incident at the sample greater than -25 dBm [78]. Therefore, for the work presented here, I used -28±2 dBm incident power at the sample. Edge-launch SMA connectors were not attached during irradiation. The irradiated resonators were re-assembled with edge-launch SMA connectors within an hour of removal from the radiation chamber and re-measured after dehydration bake using the same measurement set-up and equipment.

3.4 Irradiation Details

The irradiation of resonator samples was carried out using cobalt-60 as a radiation source. The radiation source comprised 18 rods and was stored in a containment pool. Each 17" tall rod was sealed in stainless-steel cladding and was maintained at a radial distance of 4" with 20° arc spacing between the centers of neighboring rods. A sodium sulfide ion chamber dosimetry system was used to measure the dose rate to air at the chamber center, which was 23.6 rad/s. This dose rate was corrected to different materials based on their mass

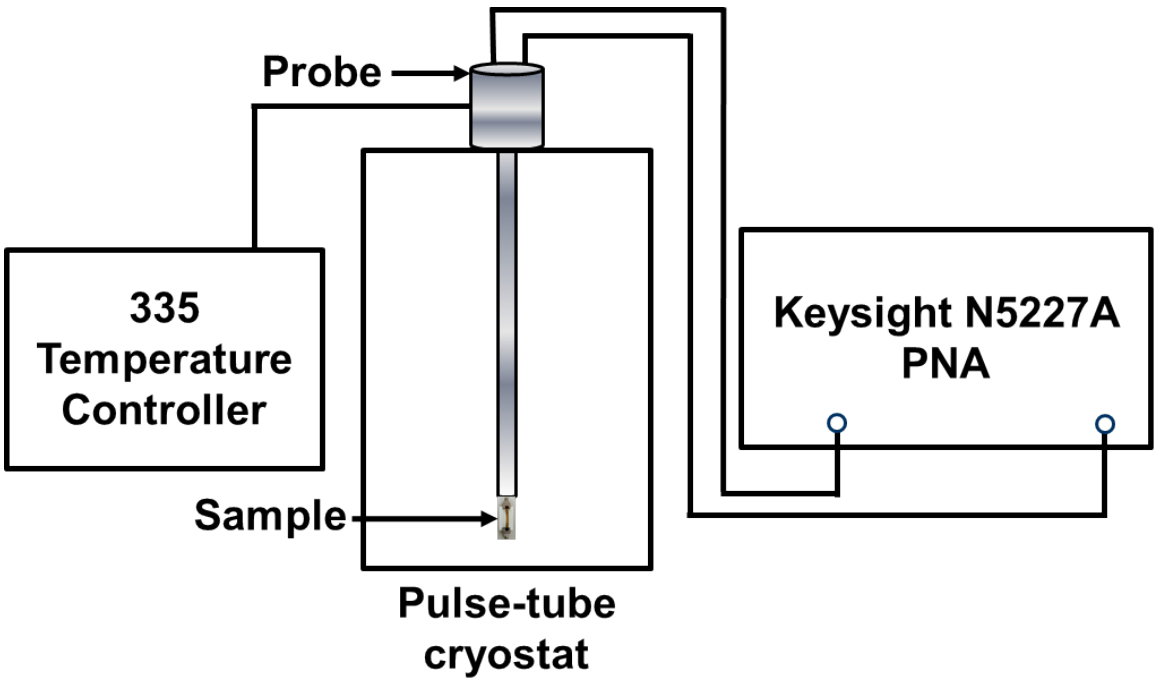

Figure 3.5: Block diagram of the measurement set-up showing Pulse-tube based closed-cycle cryostat, and Keysight performance network analyzer used to measure the S-parameters of the resonators in the desired frequency range before and after the irradiation.

energy-absorption coefficients for 1.25 MeV photons from the National Institute of Standards and Technology [79]. Absorbed dose or dose rate to any material can be calculated from the absorbed dose to air as:

$$D_{material} = D_{air} \frac{(\mu_{en}/\rho)_{material}}{(\mu_{en}/\rho)_{air}} \tag{3.1}$$

where $D_{material}$ is the dose rate to specified material, D_{air} is the dose rate to air, $(\mu_{en}/\rho)_{material}$ and $(\mu_{en}/\rho)_{air}$ is mass energy-absorption coefficient at a photon energy of interest for specified material and air, respectively. Table 3.1 gives the total absorbed dose in each material. The absorbed dose values are very high compared to the radiation levels absorbed by electronics on satellites in a geosynchronous orbit in their typical lifetime, which is 3 kGy for 10 years [80].

Table 3.1: Total absorbed dose for 4 weeks

Material	μ_{en}/ρ (cm^2/g)	$D_{material}$ (rad/s)	Total dose (Mrad (kGy))
Air, dry	2.67E-2	23.6	56.4 (564)
Niobium	2.40E-2	21.2	50.7 (507)
Polyimide	2.88E-2	25.5	60.8 (608)

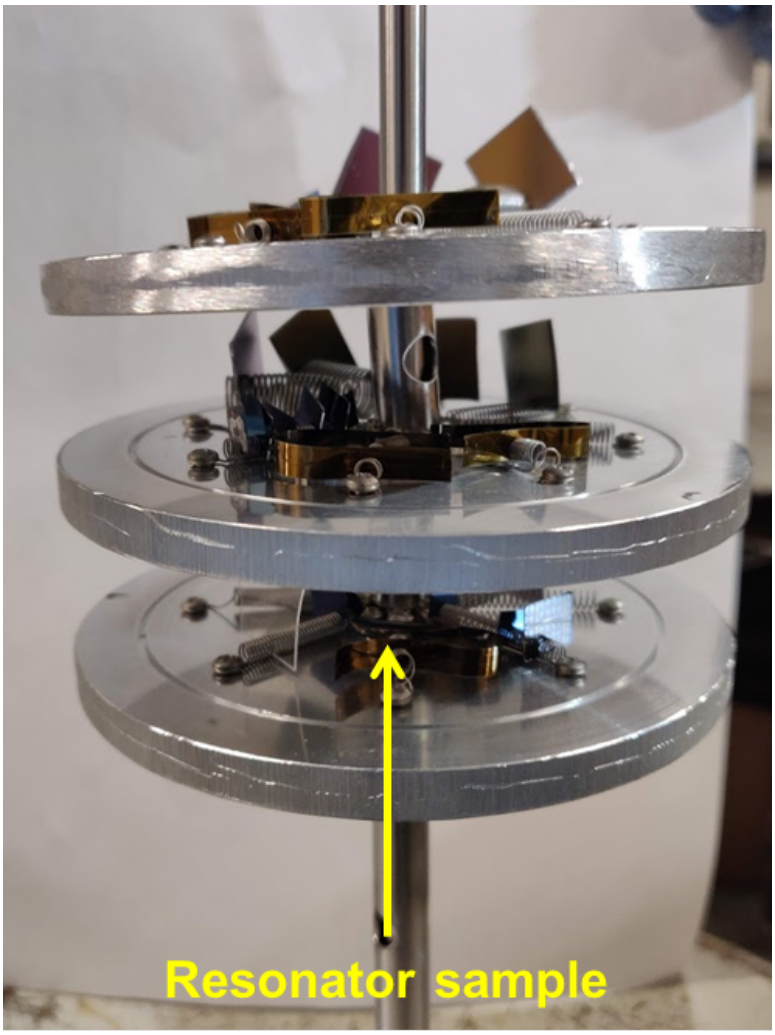

Figure 3.6: The irradiation sample holder with resonator samples.

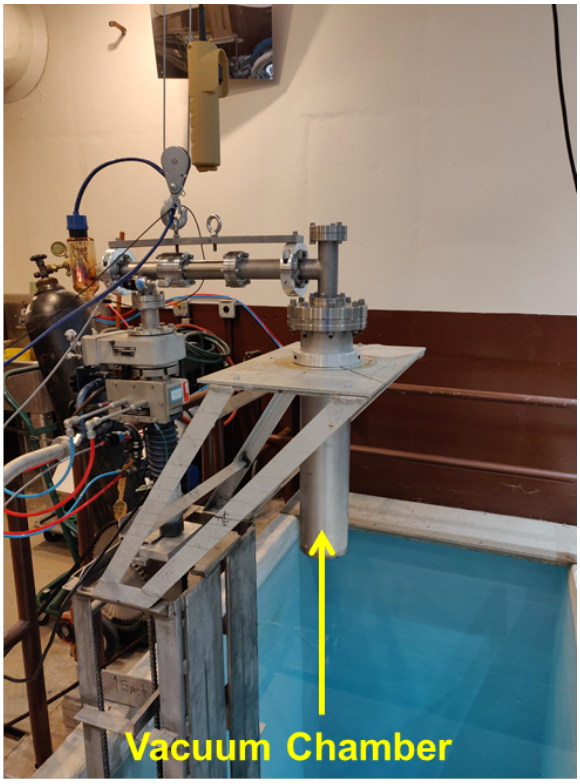

Figure 3.7: Vacuum chamber into which the sample holder is lowered.

The resonators were held radially normal to the gamma source on the sample holder. The sample holder was lowered into a cylindrical chamber and sealed. The cylindrical chamber with the sample holder was put under constant vacuum, at a pressure of 1E-6 Torr, during irradiation. The radiation source was raised from its containment pool to coaxially surround the cylindrical vacuum chamber containing the resonator samples at room temperature. Fig. 3.6 shows the sample holder with all the resonator samples. Fig. 3.7 shows the vacuum chamber and Fig. 3.8 shows the gamma radiation source. The resonator samples were under constant exposure of 1.17 and 1.33 MeV gamma photons, widely used in total-dose testing for space research [81]. The radiation source was lowered back into its safe water storage pool at the end of each week-long duration and the vacuum chamber was backfilled with N_2 to bring it up to atmospheric pressure before opening. The sample holder was pulled out and the designated resonator samples were removed. The remaining samples on the aluminum plates were immediately replaced into the chamber, and the chamber was pumped back to

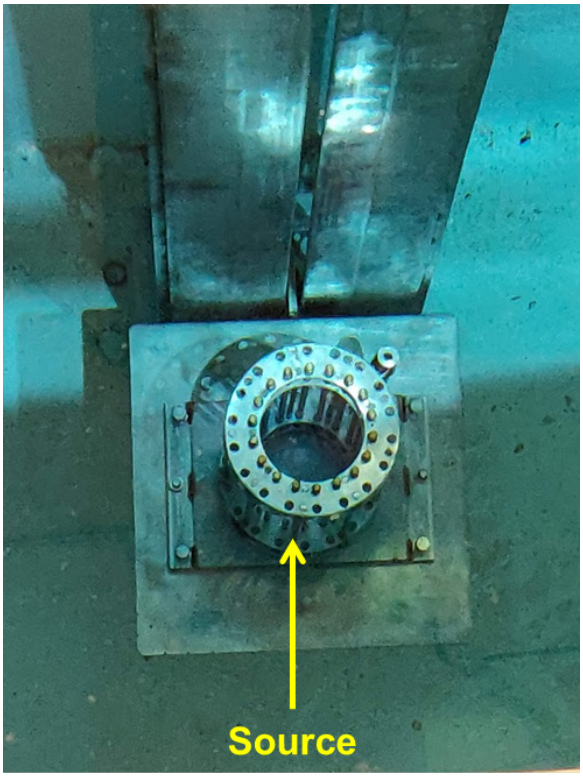

Figure 3.8: ^{60}Co source lowered into a pool of water when not in the raised position for use.

vacuum. The chamber was heated to approximately 100 °C for 2 hours during each pump-down process to drive out molecules that might have been adsorbed onto its inner walls. The resonator samples of each variant were removed from the test chamber after approximately one week or four weeks, corresponding to a maximum dose of 15.2 Mrad (152 kGy) and 60.8 Mrad (608 kGy), respectively.

3.5 Results and Discussion

The quality factors of the resonators, which provide a sensitive probe of the combined dielectric and superconductor loss, were measured before and after irradiation for the same sample. S_{12} and S_{21} were measured up to 20 GHz at multiple cryogenic temperatures (4.2 K, 3.0 K, 2.0 K, and 1.2 K). Loaded quality factors (Q_l) of the resonators at each resonant frequency were extracted by using a fit to a Lorentz line shape [82]. Fig. 3.9 and Fig. 3.10 show comparison plots of $1/Q_l$ versus the determined resonant frequency for the Nb and Al

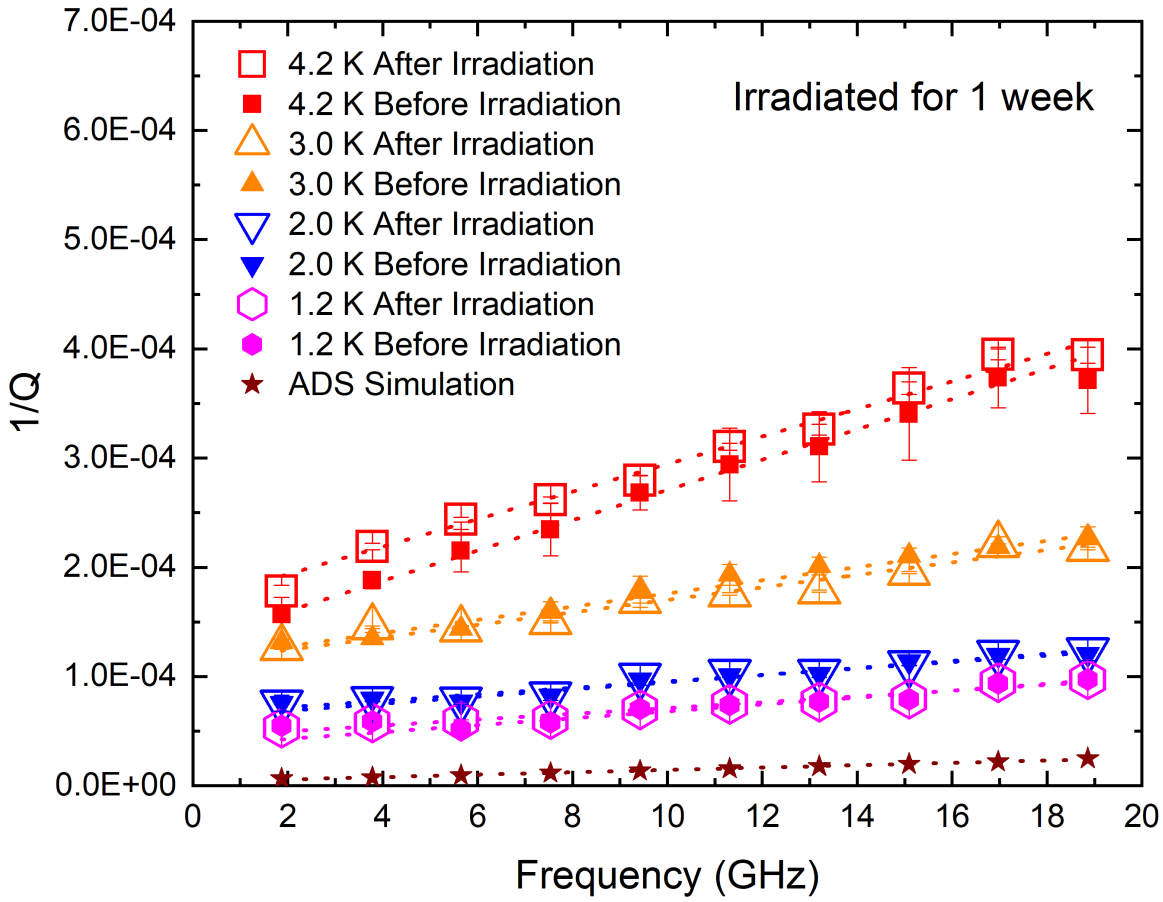

Figure 3.9: Comparison of $1/Q$ vs. resonant frequency for Nb embedded resonators before and after irradiation for one week along with ADS simulation results for the same resonator design with no conductor or dielectric loss to demonstrate coupling loss.

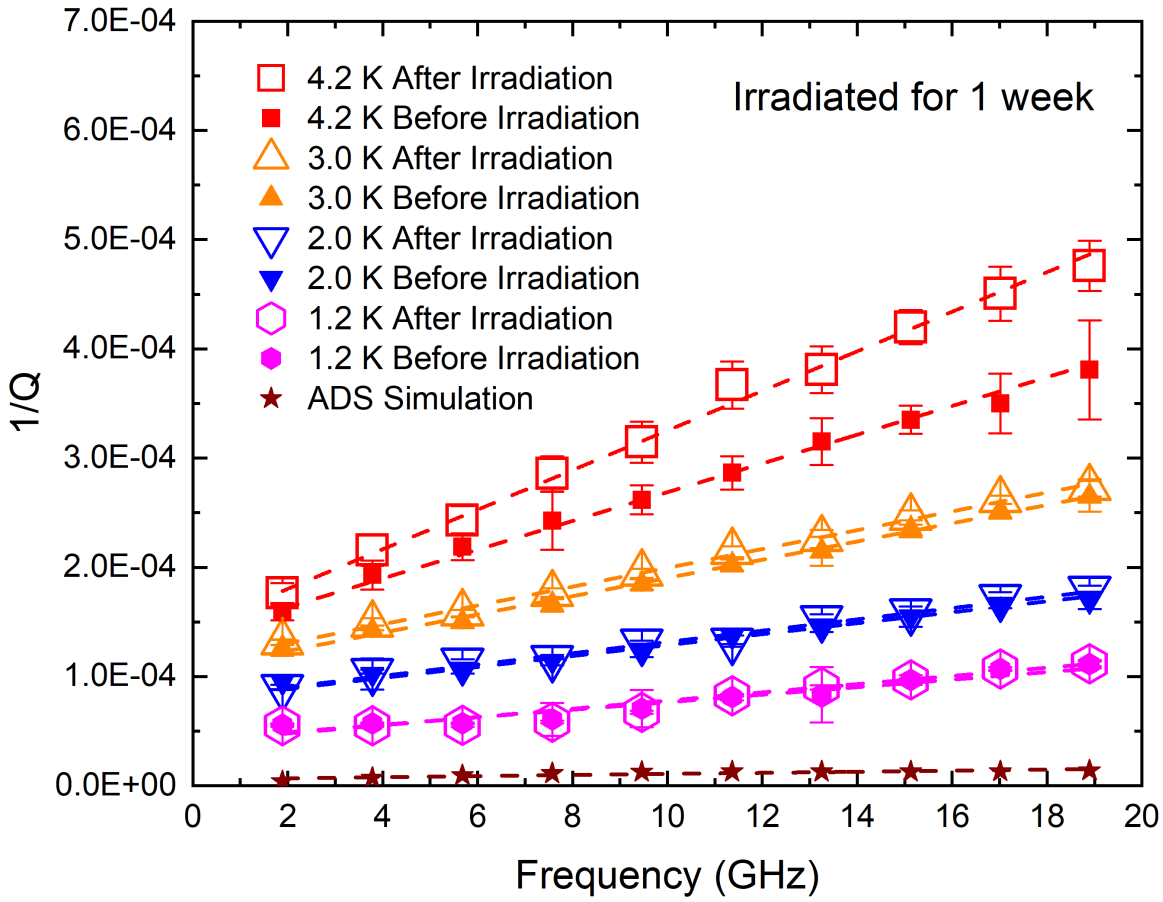

Figure 3.10: Comparison of $1/Q$ vs. resonant frequency for Al/Nb/Al embedded resonators before and after irradiation for one week along with ADS simulation results for the same resonator design with no conductor or dielectric loss to demonstrate coupling loss.

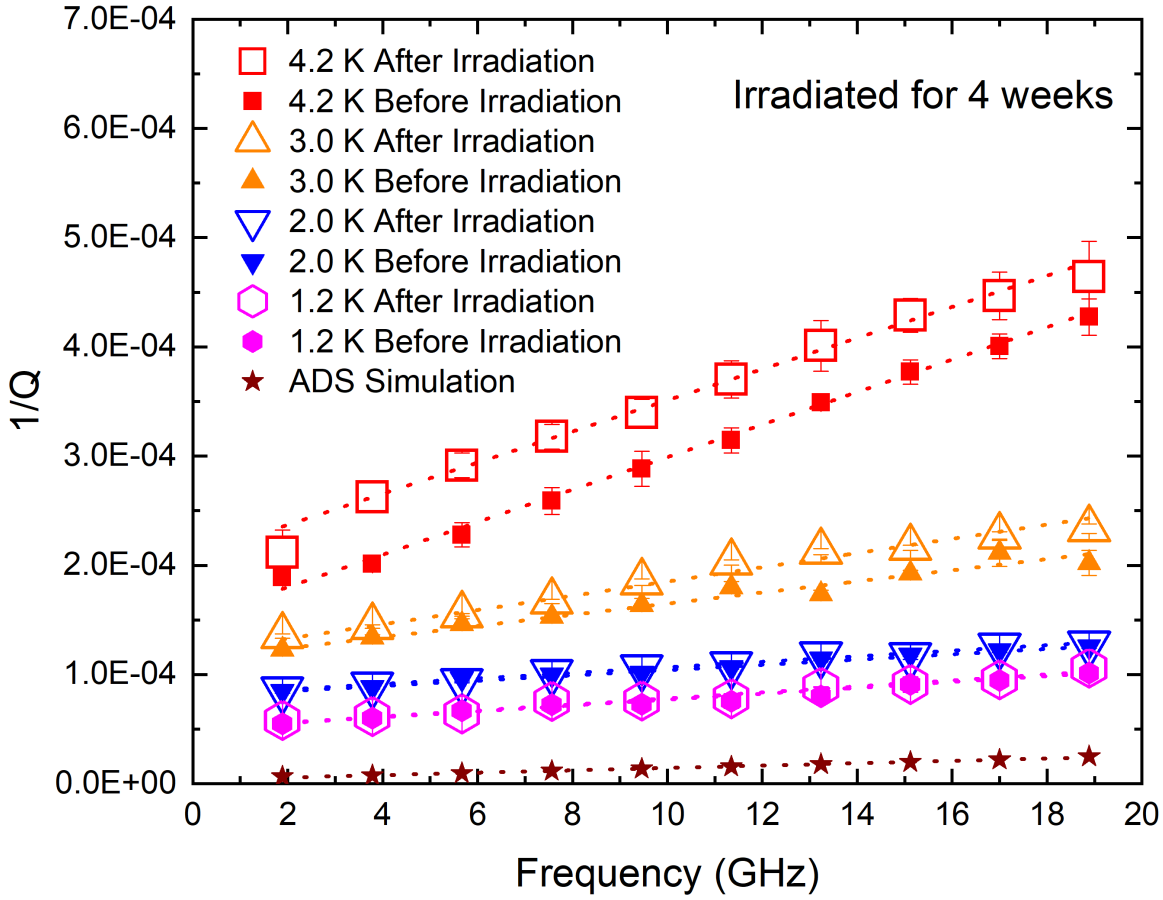

Figure 3.11: Comparison of $1/Q$ vs. resonant frequency for Nb embedded resonators before and after irradiation for four weeks along with ADS simulation results for the same resonator design with no conductor or dielectric loss to demonstrate coupling loss.

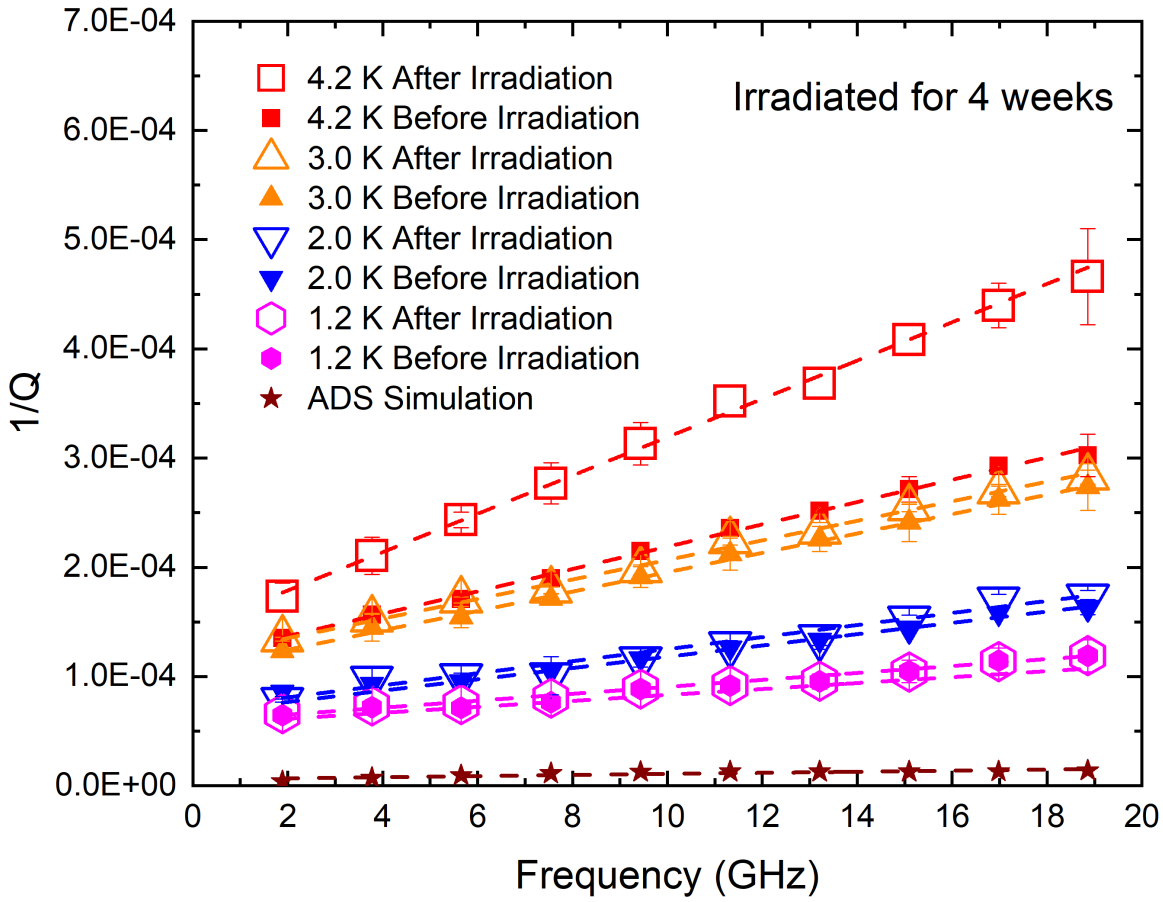

Figure 3.12: Comparison of $1/Q$ vs. resonant frequency for Al/Nb/Al embedded resonators before and after irradiation for four weeks along with ADS simulation results for the same resonator design with no conductor or dielectric loss to demonstrate coupling loss.

resonator sample before and after irradiation for one week, respectively. Fig. 3.11 and Fig. 3.12 show comparison plots of $1/Q_l$ versus the determined resonant frequency for the Nb and Al resonator sample before and after irradiation for four weeks, respectively. The plotted Q values are the average of ten discrete measurement results at each frequency. To consider the measurement errors and temperature drift inside the cryostat, the plots include 3σ error bars. ADS simulation results with zero conductor loss and zero dielectric loss have been added to provide an estimate of the sufficiently low coupling loss at each resonant frequency. A significant reduction in slope as the temperature reduces from 4.2 K to 2.0 K is consistent with BCS theory. According to BCS theory, the number of superconducting charge carriers increases exponentially as T/T_c is reduced (i.e., as the superconductor is taken further below its transition temperature T_c), resulting in a continued reduction in microwave losses as the temperature is reduced. The slope at a temperature of 1.2 K is almost approaching zero indicating that the superconductor quasiparticle loss is minimal and is mostly dominated by the dielectric loss of HD-4110.

In both conductor variants, a small increase in loss at 4.2 K was observed, which points to a small change in the superconducting properties of the conductor. The losses at 2.0 K and 1.2 K for both variants exhibited an undetectable change indicating a minimal change in the dielectric properties of the resonator samples due to radiation up to a dose of 60.8 Mrad. Fig 3.13 and Fig 3.14 show the difference in $1/Q_l$ for resonators at 4.2 K and 3.0 K with different conductors after one week and four weeks of irradiation, respectively. The difference in the extracted Q at 4.2 K for the Al/Nb/Al conductor resonators before and after irradiation was higher than the Nb conductor resonators. The results show evidence of more damage to the Al/Nb/Al conductor variant resonators resulting in decreased superconductor performance properties (T_c and I_c). Though sufficient results to show actual degradation of the Al layer aren't presented, the results point to that being the case and further exploration of the specific degradation mechanisms is warranted. Fig 3.15 and Fig 3.16 show the difference in

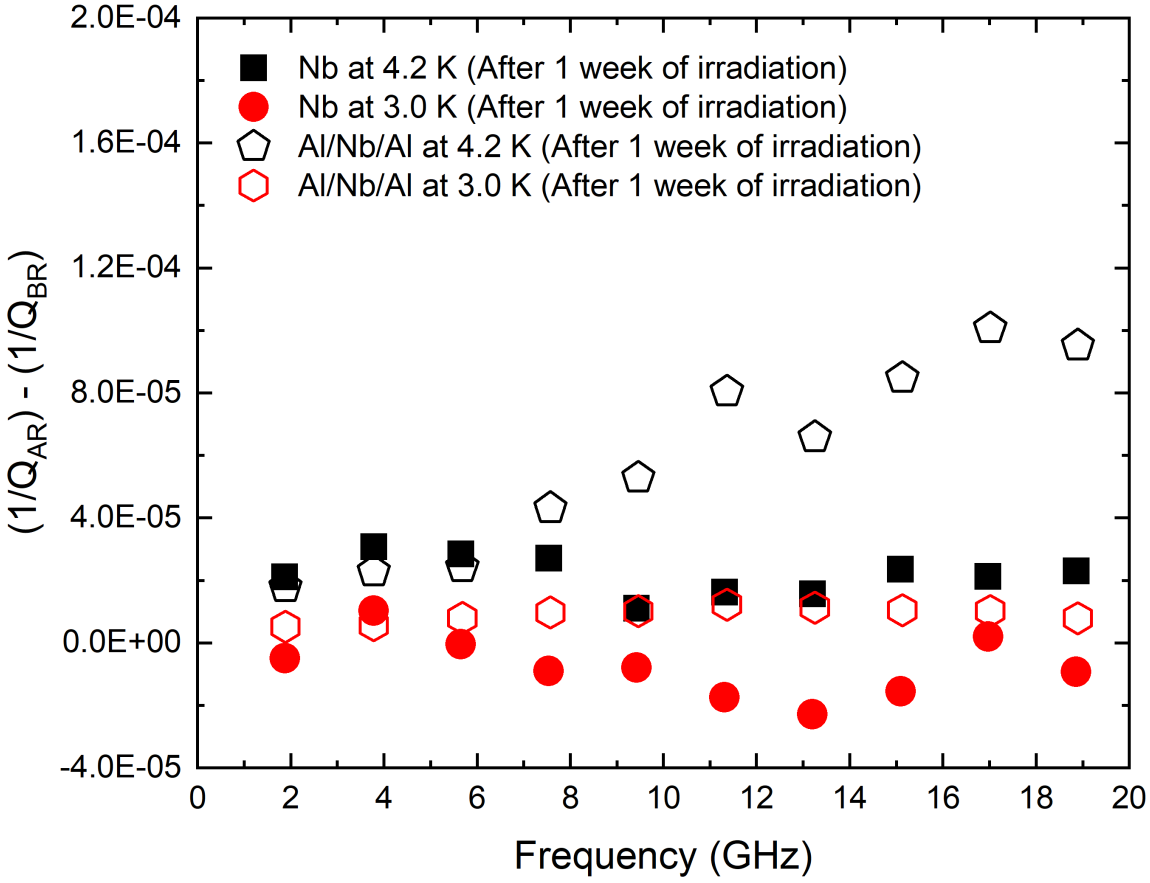

Figure 3.13: Difference in $1/Q$ vs. resonant frequency at 4.2 K and 3.0 K for different conductor variant embedded resonators after one week of irradiation.

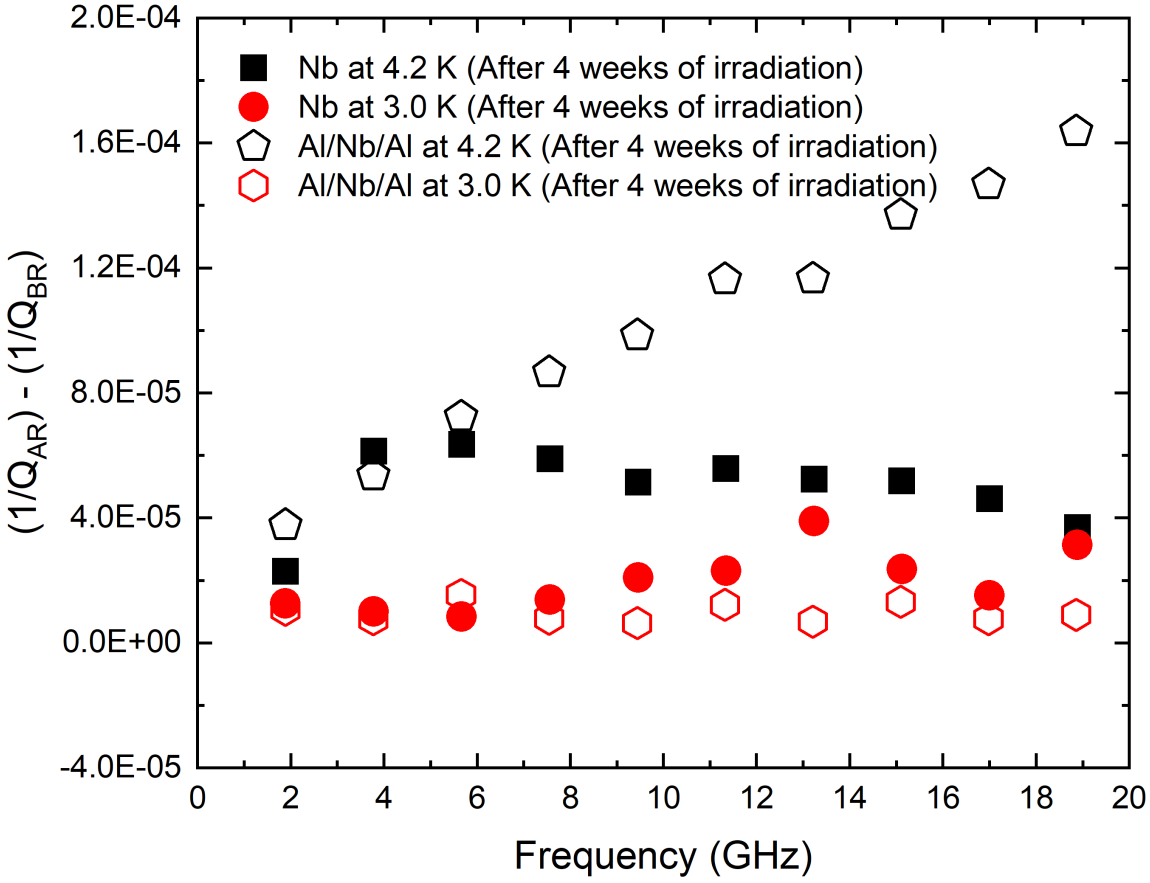

Figure 3.14: Difference in $1/Q$ vs. resonant frequency at 4.2 K and 3.0 K for different conductor variant embedded resonators after four weeks of irradiation.

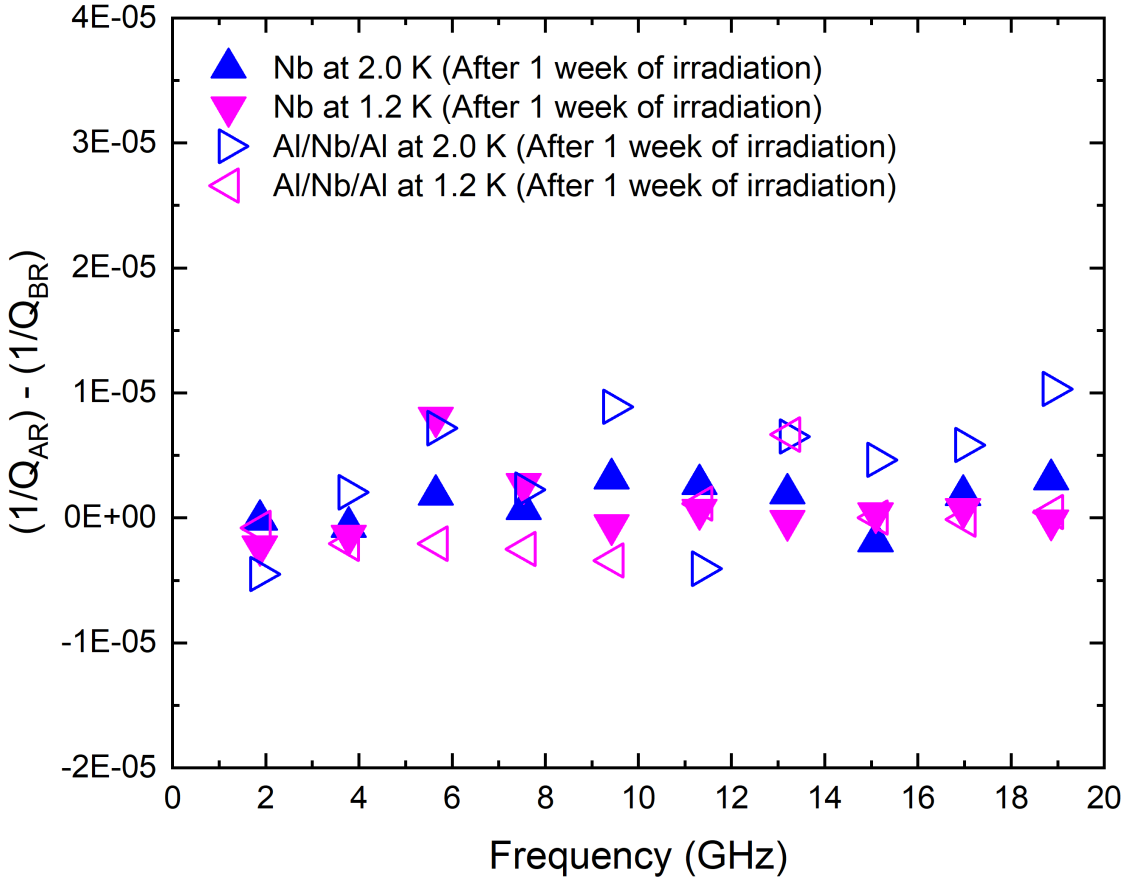

Figure 3.15: Difference in $1/Q$ vs. resonant frequency at 2.0 K and 1.2 K for different conductor variant embedded resonators after one week of irradiation.

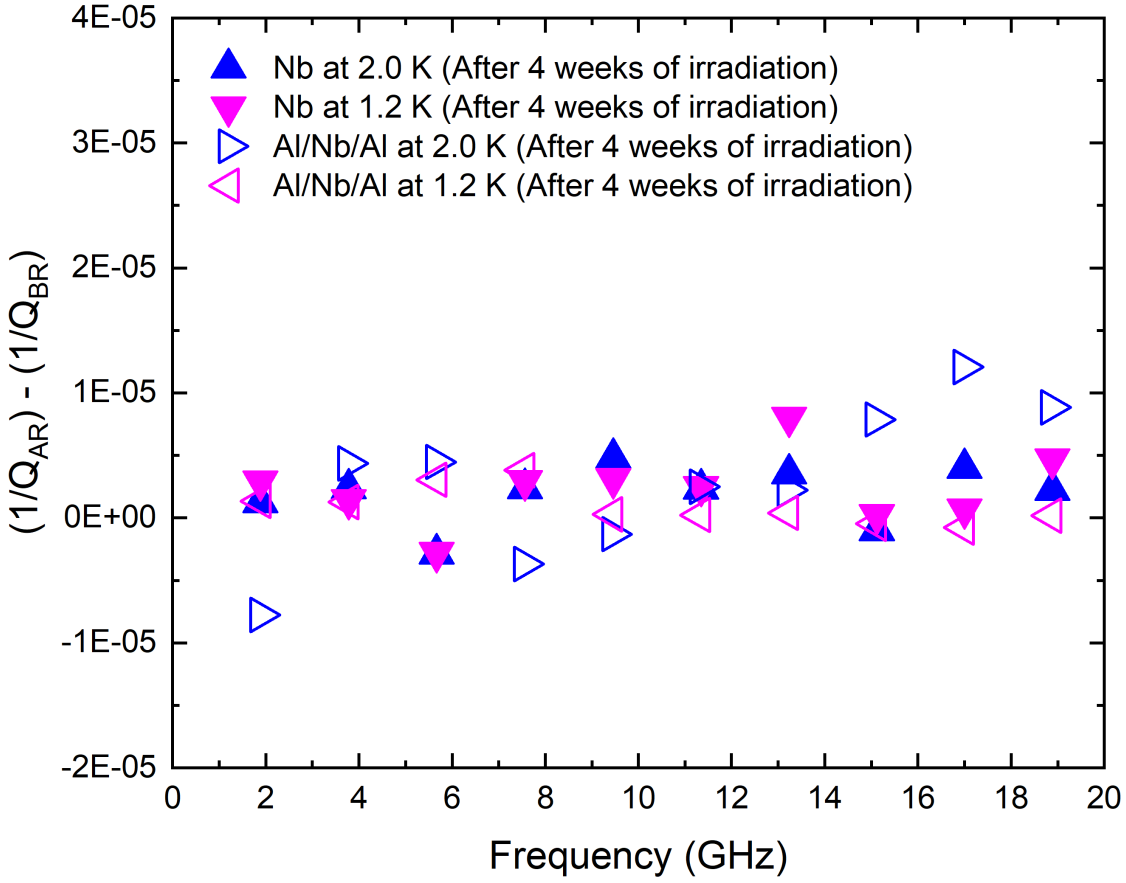

Figure 3.16: Difference in $1/Q$ vs. resonant frequency at 2.0 K and 1.2 K for different conductor variant embedded resonators after four weeks of irradiation.

$1/Q_l$ for resonators at 2.0 K and 1.2 K with different conductors after one week and four weeks of irradiation, respectively.

The slopes and the zero-frequency intercepts of the $1/Q_l$ plots correspond to quasiparticle-induced losses ("BCS losses") and low-frequency dielectric loss, respectively, based on superconducting transmission line theory.

The loaded quality factor Q_l can be described as:

$$\frac{1}{Q_l} = \frac{1}{Q_c} + \frac{1}{Q_d} + \frac{1}{Q_r} + \frac{1}{Q_{coupling}} \tag{3.2}$$

where Q_c, Q_d, Q_r and $Q_{coupling}$ are the Q-factors associated with conductor loss, dielectric loss, radiation loss, and coupling loss, respectively. Radiation losses for these smaller cross-section resonators and conductor losses at 1.2 K are both assumed to be negligible. These weakly-coupled resonators have sufficiently high $Q_{coupling}$ as demonstrated in the ADS simulation results and can be neglected. Thus, equation 3.2 can be modified to:

$$\frac{1}{Q_l} = \frac{1}{Q_d} \tag{3.3}$$

For microstrip geometries, the dielectric loss tangent (tan δ) can be determined from Q_d using the expression:

$$Q_d = \frac{1}{tan\delta}(1 + \frac{1-q}{q\epsilon_r}) \tag{3.4}$$

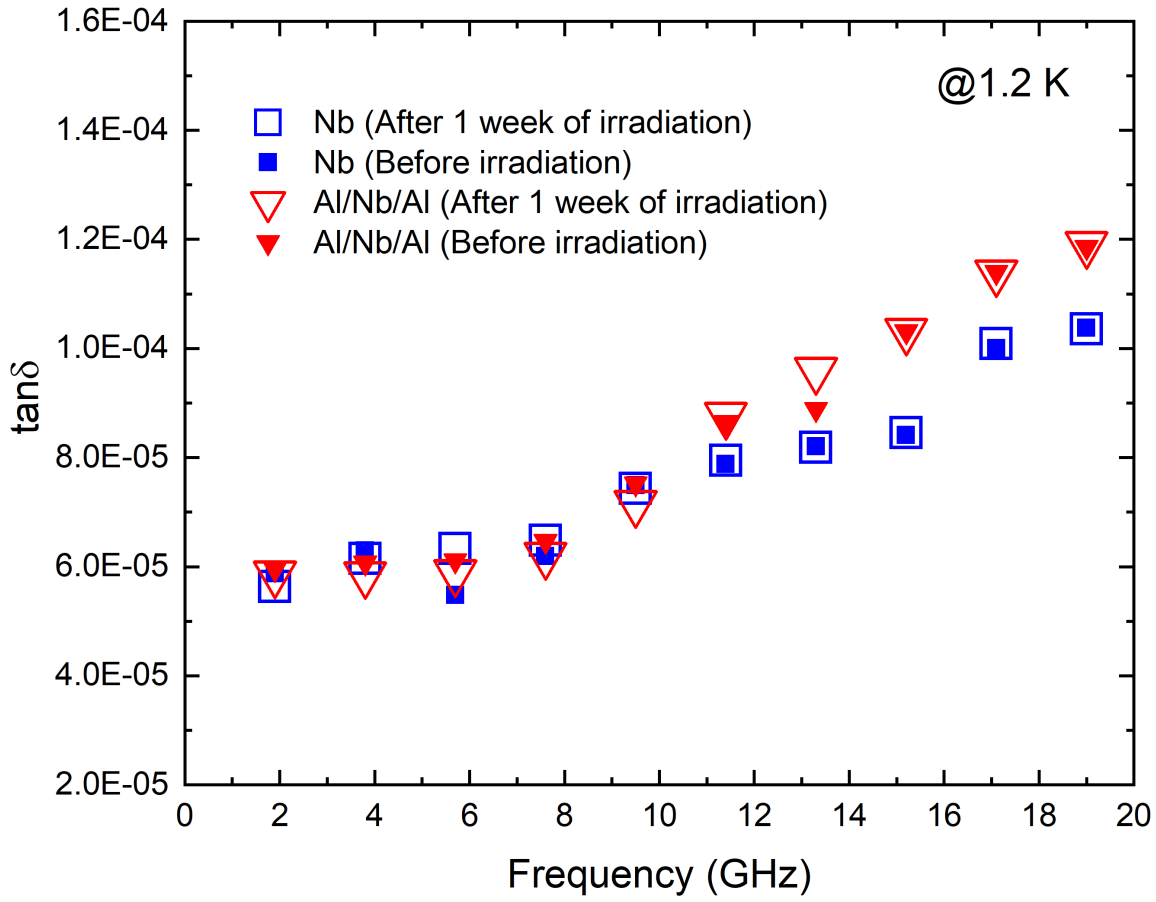

Figure 3.17: Extracted upper bound tanδ at different resonant frequencies at 1.2 K after one week of irradiation for different conductor variant embedded resonators.

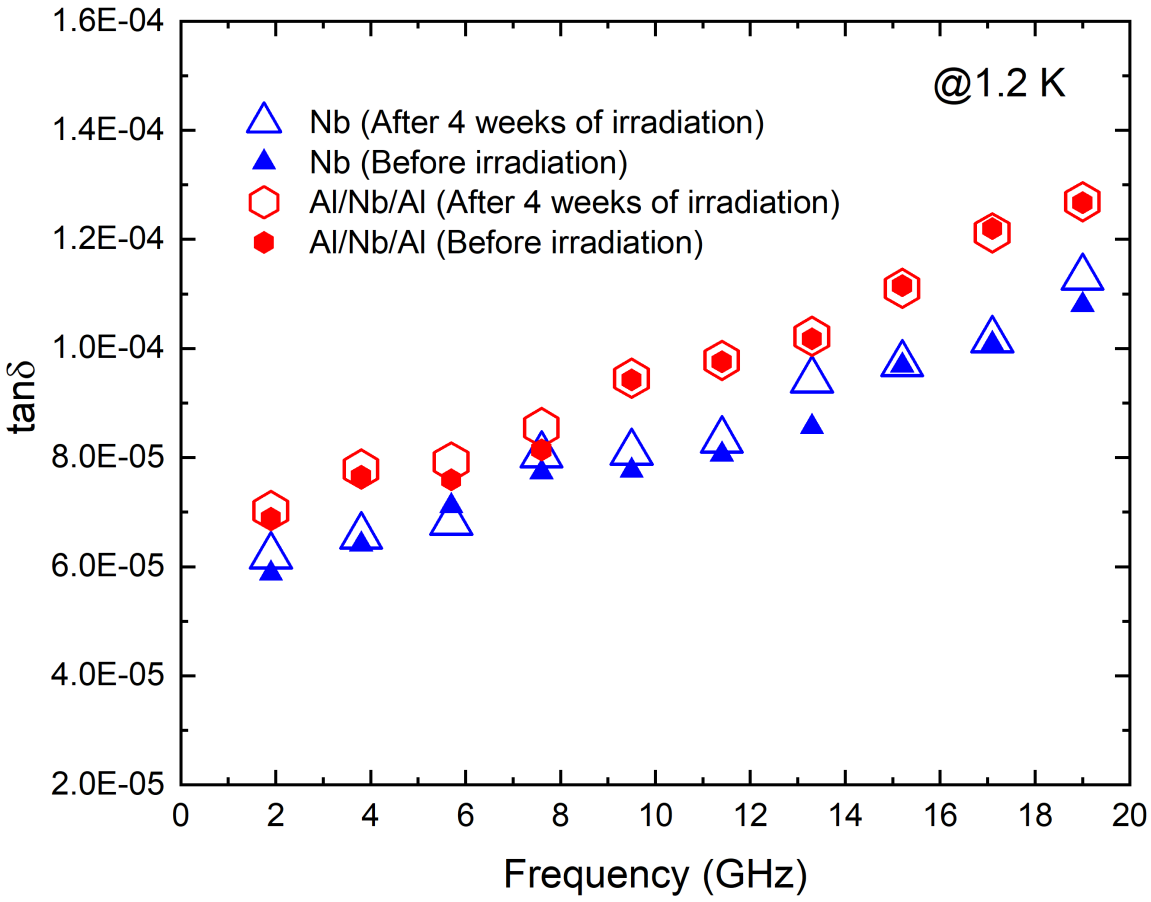

Figure 3.18: Extracted upper bound tanδ at different resonant frequencies at 1.2 K after four weeks of irradiation for different conductor variant embedded resonators.

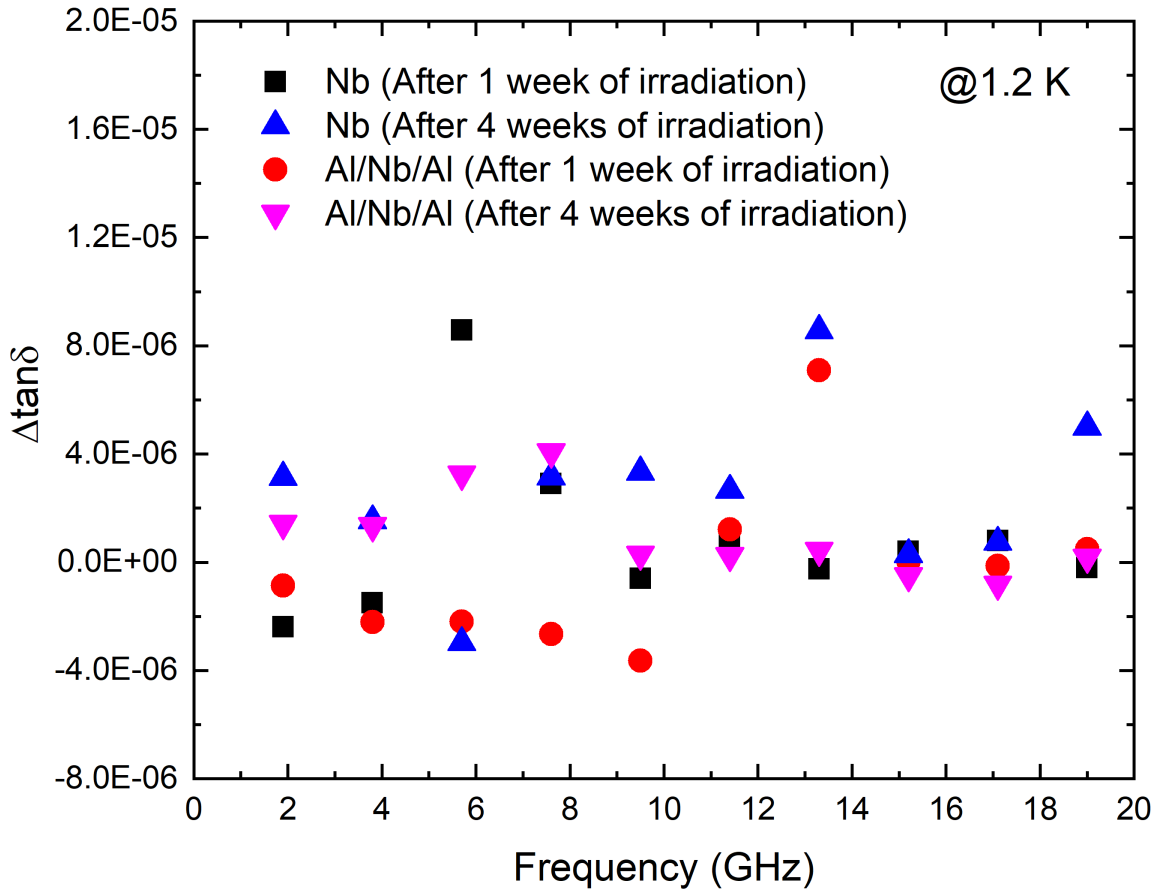

Figure 3.19: Extracted upper bound on the change in tanδ at different resonant frequencies at 1.2 K after one and four weeks of irradiation for all embedded resonators. The plot shows negligible degradation of dielectric loss tangent after one and four weeks of irradiation.

where, ϵ_r is the relative permittivity of the dielectric and q corresponds to a microstrip filling factor, which has been previously determined to be 0.828 for the geometries of these embedded microstrip transmission lines. More details on calculations of the dielectric filling factor are given in [78]. Fig. 3.17 and Fig. 3.18 show the extracted upper bound tanδ at different resonant frequencies at 1.2 K after one and four weeks of irradiation for different conductor variant embedded resonators, respectively. The determined tanδ values showed negligible change at different resonant frequencies for each of the embedded resonator variants before and after irradiation for one and four weeks. Fig 3.19 shows the determined change in tanδ values after one and four weeks of irradiation for all embedded resonators. Even with the high radiation doses the polyimide had no detectable change in its dielectric properties.

3.6 Summary

This chapter investigated the impact of gamma radiation on the quality factors of Al/Nb/Al embedded resonators and Nb embedded resonators, shedding light on their behavior in extreme and harsh environments. The primary objective was to assess whether these resonators experienced degradation following exposure to gamma radiation, which is prevalent in various real-world scenarios.

Through controlled irradiation experiments and subsequent measurements of the resonators' Q values before and after exposure, valuable insights were gained regarding their resilience in extreme conditions. The results demonstrated that both Al/Nb/Al embedded resonators and Nb embedded resonators exhibited changes in their Q values following gamma radiation exposure. However, the extent of degradation varied depending on the specific resonator design and materials used.

For the Al/Nb/Al embedded resonators, a noticeable degradation in the Q values at higher frequency was observed after four weeks of gamma radiation exposure compared to the Nb embedded resonators. This degradation can be attributed to several factors, including radiation-induced quasiparticle generation, trapping effects, and material damage. On the

other hand, the Nb embedded resonators showed more robustness in the face of gamma radiation. Although some minor changes in the Q values were observed, they were relatively smaller compared to the Al/Nb/Al embedded resonators.

Overall, this chapter provides valuable insights into the behavior of Al/Nb/Al embedded resonators and Nb embedded resonators in extreme environments. The results highlight the importance of considering the effects of gamma radiation on the performance of superconducting resonators, especially when designing cryogenic systems for radiation-intensive applications. The findings from this chapter contribute to the broader understanding of signal integrity challenges at cryogenic temperatures and provide guidance for the design and operation of robust cryogenic systems.

Chapter 4

Very Long Superconducting Resonators on Si Substrate

4.1 Introduction

This chapter focuses on utilizing very long resonators as a means of investigating and evaluating material losses at cryogenic temperatures. These resonators offer a valuable tool for analyzing the dense resonance frequency spectrum with exceptional precision, enabling researchers to identify the impact of various fabrication procedures on the overall quality and performance of superconducting structures.

The primary objective of this study is to utilize the dense resonance frequency spectrum obtained from these very long superconducting resonators to characterize material losses in superconducting structures across a range of frequencies at cryogenic temperatures. By carefully examining the behavior of the resonators, researchers can gain insight into the origin and magnitude of losses associated with different materials and fabrication techniques.

Characterizing material losses in superconducting structures is of utmost importance in quantum computation. Loss mechanisms, such as dielectric loss, two-level system (TLS) loss, and surface loss, can significantly degrade the coherence of quantum bits and lead to errors in computations. Therefore, understanding these loss mechanisms and their relationship to the underlying materials becomes indispensable for developing robust and error-resistant quantum systems.

Furthermore, by exploring the impact of different fabrication procedures on material losses, this research aims to provide valuable guidelines for designing and manufacturing superconducting structures with enhanced performance and reduced losses. Identifying the fabrication techniques that yield the lowest losses can pave the way for the development of more efficient and reliable quantum computing systems.

In summary, this chapter investigates the characterization of material losses in superconducting structures at cryogenic temperatures using very long resonators. Through a comprehensive analysis of the resonance frequency spectrum, this chapter aims to shed light on the losses associated with different materials and fabrication techniques used to process the structures. By identifying the most favorable fabrication procedures and materials, researchers can take crucial steps toward realizing high-performance quantum computers capable of harnessing the full potential of quantum mechanics.

The subsequent sections of this chapter will dive into the methodology, experimental setup, data analysis, and discussion of results obtained from the use of very long resonators to characterize material losses in superconducting structures at cryogenic temperatures. At the end of this study, a deeper understanding of loss mechanisms and effective strategies to minimize losses is expected to contribute to the advancement of quantum computation and the realization of practical quantum computers.

4.2 Design

The long shunt-microstrip resonators used in this study were meticulously designed to exhibit a trace width corresponding to a 50 Ω characteristic impedance. By adhering to this specific impedance, efficient power transfer and impedance matching between the resonator and the measurement circuitry were achieved. The signal line width for a characteristic impedance of 50 Ω on 200 μ m thick intrinsic silicon was 162 μm. The design process, including simulations, was carried out using ADS software to determine the optimal coupling length and coupling gap for material loss characterization at cryogenic temperatures.

The selection of the coupling length and the coupling gap is critical as it determines the coupling strength between the resonator and the measurement circuit, which directly influences the sensitivity of material loss characterization. To achieve a comprehensive understanding of the loss mechanisms, it is desirable to operate the resonator within a coupling region affected by both conductor and dielectric losses.

Using the ADS momentum simulation tool, numerous simulations were conducted to explore the effects of different coupling lengths and coupling gaps on the resonator's performance. The simulations considered the electromagnetic properties of the materials involved, as well as the expected cryogenic operating temperatures. The goal was to identify a coupling configuration that maximizes sensitivity to material losses across a wide range of frequencies.

By iterative adjustment of the coupling length and coupling gap, the simulations provided insight into the resonator's behavior, such as its resonance frequency, quality factor, and sensitivity to losses. The coupling configuration that yielded the desired sensitivity and performance was selected for further analysis and fabrication.

The simulations also played a crucial role in evaluating the impact of various factors on the resonator's performance. Parameters such as substrate material, superconducting film thickness, and dielectric properties were taken into account to assess their effects on the resonator's overall performance and sensitivity to material losses. This comprehensive analysis helped guide the design process and ensure the suitability of the resonator for precise material loss characterization at cryogenic temperatures. Fig. 4.1 shows the mask design from the ADS software. The total length of the resonating section was 4.17 m and the corresponding fundamental frequency was 13.4 MHz. Fig. 4.2 shows the cross-section view of the microstrip resonators.

4.3 Fabrication

The fabrication of long shunt-microstrip resonators involved two different procedures using two different conductors: Nb and Al. In both cases, the processing was carried out on intrinsic silicon wafers, and the fabrication process began with wafer cleaning. Intrinsic silicon wafers were chosen as the substrate material due to their favorable electrical properties and compatibility with the subsequent fabrication steps. These wafers offer a high purity, low doping environment, which minimizes unwanted electrical losses and provides a stable platform for the resonator structures [83, 84, 85].

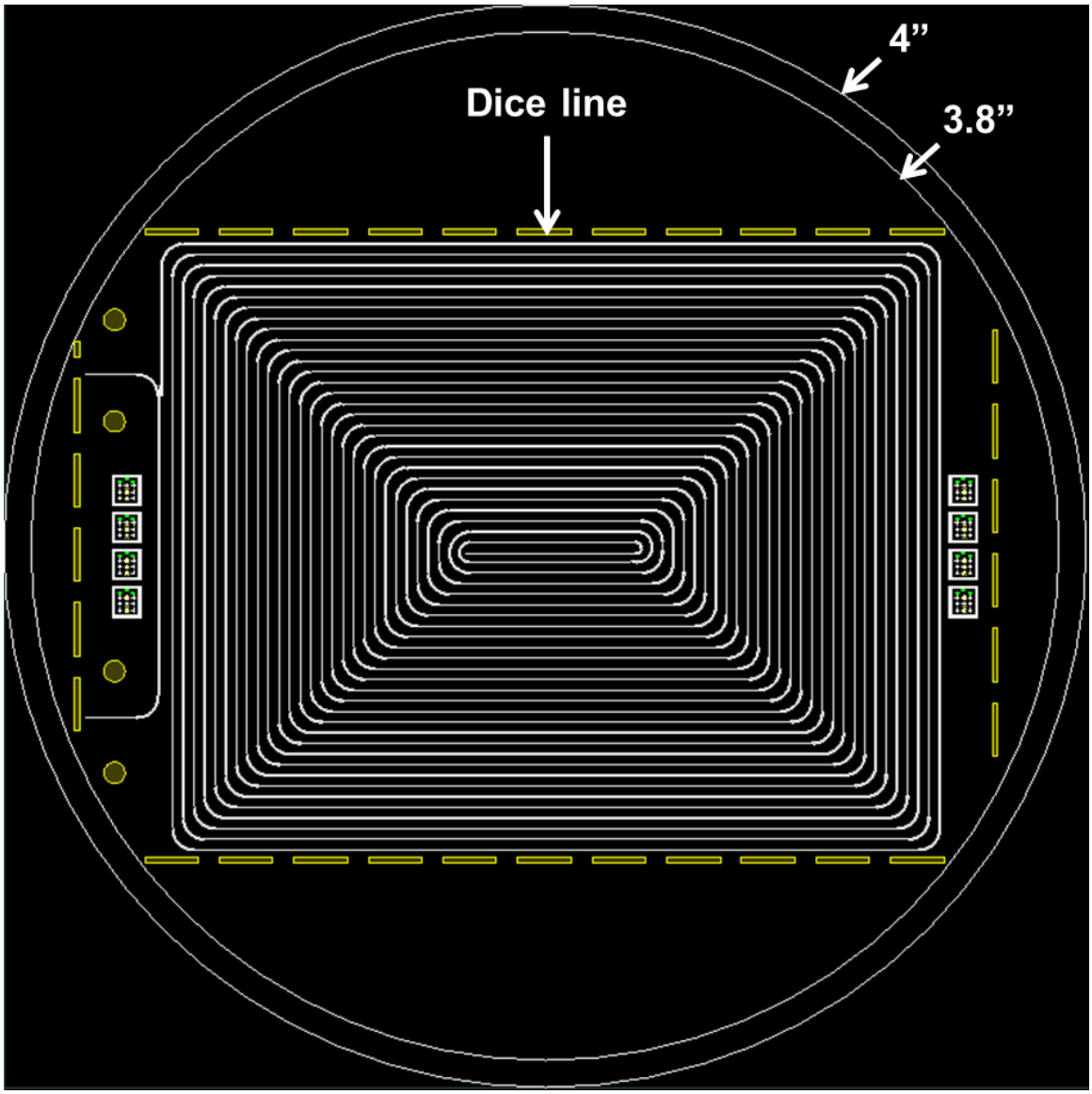

Figure 4.1: Long shunt-microstrip resonator mask design from ADS. The total length of the resonating section was 4.17 m, the fundamental frequency was 13.4 MHz and the coupling gap was 20 μm and the coupling length was 2000 μm.

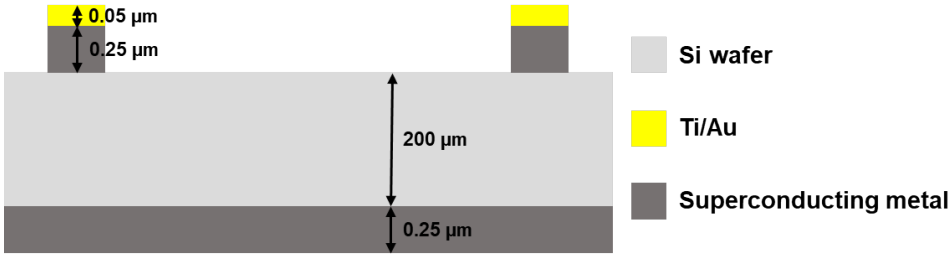

Figure 4.2: Cross-section view of the long superconducting microstrip resonator. Nb and Al are the two superconducting metals deposited on different wafers processed using either liftoff or an etching technique.

Prior to the fabrication process, the intrinsic silicon wafers underwent a thorough cleaning procedure known as the RCA clean. RCA clean is a standard cleaning technique widely used in semiconductor manufacturing to remove contaminants and optimize the wafer surface for subsequent processing steps. The RCA clean typically involves a sequence of cleaning steps using a mixture of deionized water, hydrogen peroxide, and ammonium hydroxide. These cleaning solutions effectively remove organic and inorganic residues from the wafer surface, ensuring a clean substrate for subsequent deposition and patterning steps [86, 87].

The incorporation of different metals and the utilization of intrinsic silicon wafers, along with the RCA cleaning process, provided a suitable foundation for the fabrication of the long-shunt-microstrip resonators. In the subsequent sections, specific fabrication steps employed for the patterning of superconducting metal traces on the wafers are explored in more detail.

4.3.1 Liftoff Process

A negative resist AZ nLOF 2035 was used for the fabrication of long-shunt microstrip resonators using the liftoff process. This process involved several steps, starting with the coating of intrinsic silicon wafers with the resist material. To ensure uniform resist thickness, the AZ nLOF 2035 resist was carefully spun onto the wafers at an optimized speed. The spin speed was selected to yield a resist thickness of approximately 4 µm, providing a suitable layer for subsequent patterning. After the photoresist coating, a negative mask with the desired resonator design, as shown in Fig. 4.1, was carefully aligned and positioned on the

coated wafer using a mask aligner. The unexposed regions of the mask corresponded to the desired resonator pattern. Once aligned, the mask and the coated wafer were exposed to the UV light source, which activated the photosensitive properties of the resist material. The exposure process caused the unexposed regions of the resist to become soluble, while the exposed regions remained intact. Following exposure, the wafer underwent a development process using AZ 300MIF developer. This process selectively removed the unexposed regions of the resist, leaving behind a positive patterned resist layer on the wafer surface. The pattern corresponded to the desired resonator structure, allowing for the subsequent deposition of the superconducting materials in the desired pattern. To prepare the patterned structures for the subsequent deposition of the superconducting materials, the wafer underwent an oxygen plasma treatment. The oxygen plasma served to remove any residual resist material from the exposed areas, ensuring a clean surface for the subsequent deposition steps. Once the plasma treatment was completed, the wafers with the patterned resist structures were loaded into a deposition chamber. In the case of Nb resonators, a sputtering technique was employed for the deposition process. The sputtering process involved bombarding a Nb target material with high-energy ions, causing the Nb atoms to be ejected and subsequently deposited onto the patterned resist structures. The deposition was carried out until it resulted in the formation of a thin Nb conductor layer with a thickness of approximately 0.25 μm. For Al resonators, an e-beam evaporation technique was employed. In this process, a solid Al source was heated using a high-energy electron beam, causing the Al atoms to vaporize and condense onto the patterned resist structures. The deposition of Al resulted in a conductor layer with a thickness of approximately 0.25 μm. Fig. 4.3 shows an image of the wafer with Nb metal after signal layer deposition and liftoff.

4.3.2 Etching Process

In the same run where the patterned wafers for the liftoff process were deposited with metal, additional wafers were added to the deposition chamber to coat a blanket metal layer.

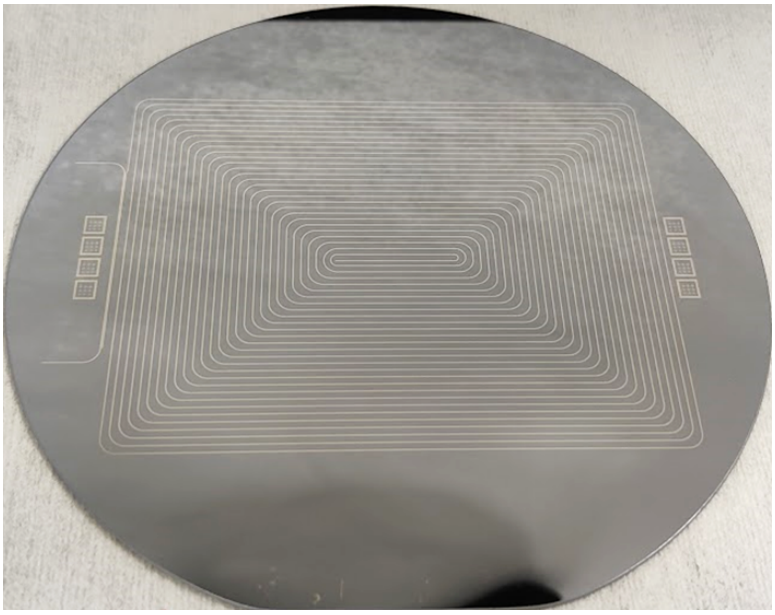

Figure 4.3: Image of a wafer with Nb metal trace after signal layer deposition and resist removal. The signal trace was patterned using the liftoff technique. The wafer was then patterned for wirebond pads and deposited with Ti/Au.

These wafers served as the starting point for the etching process, allowing for the creation of resonator structures without the need for the liftoff technique. To define the desired resonator structures, the wafers with the blanket metal layer underwent a patterning step. A positive resist, AZ 9245, was spun onto the wafers to create a uniform resist layer. The wafers were then exposed to UV light using a mask aligner. Following exposure, the wafers were developed using AZ 400K developer. This development process selectively removed the exposed regions of the resist, leaving behind a patterned resist layer on the wafers. The pattern corresponded to the desired resonator structures, with the undesired regions exposed and ready for etching.

For the Nb resonators, an Inductively Coupled Plasma Etching (ICP) technique was employed using a Trion etcher. The etching process utilized a combination of CF_4 and O_2 gases in the Trion etcher. The CF_4 gas served as the main etchant, while the O_2 gas acted as an assist gas, enhancing the etching process. The ICP etching with CF_4 and O_2 effectively removed the exposed Nb regions, defining the desired resonator structures. The etch rate for

Table 4.1: Etching Recipe Parameters Used for Nb Metal Etching.

Etchant	CF_4/O_2
Pressure (mTorr)	150
Power (W)	200
Refl. Power (W)	10
CF_4 Flow (sccm)	42
O_2 Flow (sccm)	8
He Cooling Pressure (Torr)	5

Nb using the Trion etcher was 20 nm per minute. Table 4.1 shows the etching parameters used for Nb metal etching using Trion etcher.

For the Al resonators, wet etching was implemented. Wet etching involved immersing the wafers in a suitable etchant solution that selectively removed the exposed regions of the metal layer. The etchant used for wet etching of Al wafers was PAE etchant. The etch rate for Al using the wet etching process was 42 nm per minute.

After the desired resonator metal patterns were obtained through the liftoff and etching processes, all the wafers underwent an additional patterning step. This step involved using a positive mask and positive resist AZ 9245 to create a positive pattern for the deposition of Ti/Au in the wirebond regions. A positive mask with the desired wirebond pattern was carefully aligned and positioned on the wafers coated with the resonator structures and exposed to UV light. After exposure, the wafers were developed using AZ 400K developer. The next step involved the deposition of Ti/Au in the wirebond regions. The Ti layer served as an adhesion layer, ensuring good bonding between the Au layer and the superconducting metal. The deposition of Ti/Au in the wirebond regions allowed for the subsequent wire bonding of the fabricated resonators to a printed circuit board. The PCB featured coplanar waveguide (CPW) lines, providing the necessary electrical connections for the resonator

measurements. After the deposition of Ti/Au in the wirebond regions, the wafers underwent the liftoff process to remove the unwanted metal and define the desired wirebond structures.

After the liftoff process, the wafers were once again loaded into the deposition chamber for the deposition of the backside ground plane. For the Nb backside ground plane, sputter deposition was employed. In the case of the Al backside ground plane, e-beam evaporation was utilized. The deposition of Nb and Al for the backside ground plane completed the fabrication process of the long shunt-microstrip resonators. These resonators now possessed the necessary metal patterns, including the wirebond regions with Ti/Au deposition and the backside ground plane for optimal performance.

After the completion of the fabrication process, an additional step was performed to protect the fabricated resonators before dicing. The wafers, containing the completed resonator structures, were coated with a protective layer of AZ 9245 resist. This resist layer acted as a shield, safeguarding the resonators from potential damage or contamination during the subsequent dicing process. A dicing saw, specifically designed for precision cutting, was employed to dice the wafers. The dicing saw utilized a fine diamond blade and other suitable cutting tools to make precise cuts along the predefined lines, separating the resonators from the wafer.

After the dicing process, the next step involved the removal of the AZ 9245 resist layer that was applied as a protective coating. The removal of the resist was necessary to ensure the cleanliness of the fabricated resonators before the assembly process.

4.4 Assembly

In the assembly process, the diced resonator samples were carefully attached to a PCB featuring CPW lines using silver paint. This assembly step aimed to establish a reliable electrical connection between the resonator and the PCB, ensuring optimal performance. Fig. 4.4 shows the PCB with CPW traces and a diced Al resonator sample before the assembly process.

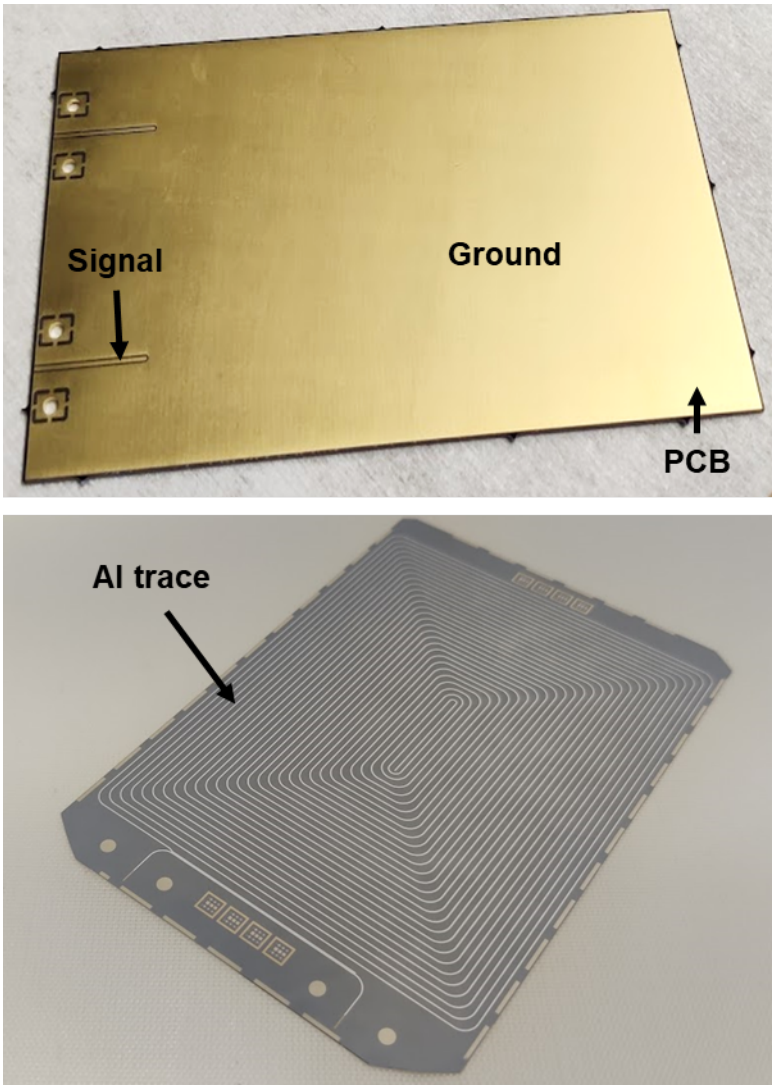

Figure 4.4: PCB with CPW traces and a diced Al resonator sample before the assembly process. The resonator sample is attached to the PCB using silver paint. The diced resonator sample was carefully positioned and placed onto the silver paint-coated area of the PCB at room temperature and later cured in a vacuum oven at 80 °C for an hour to improve the electrical conductivity of the silver paint, enhancing the bond between the PCB and the resonator sample and ensuring a robust electrical connection.

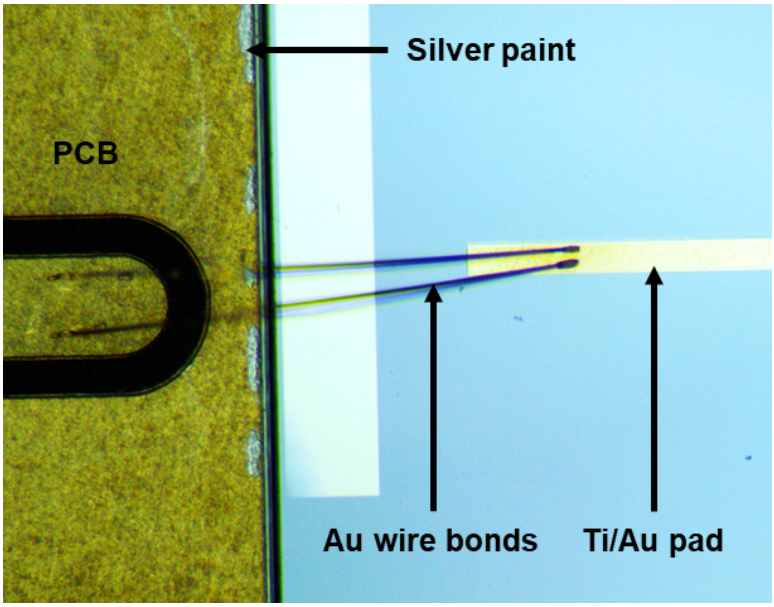

Figure 4.5: Wirebonds connecting resonator signal with CPW signal line on PCB. Two wire bonds per signal connection were made to reduce the inductance.

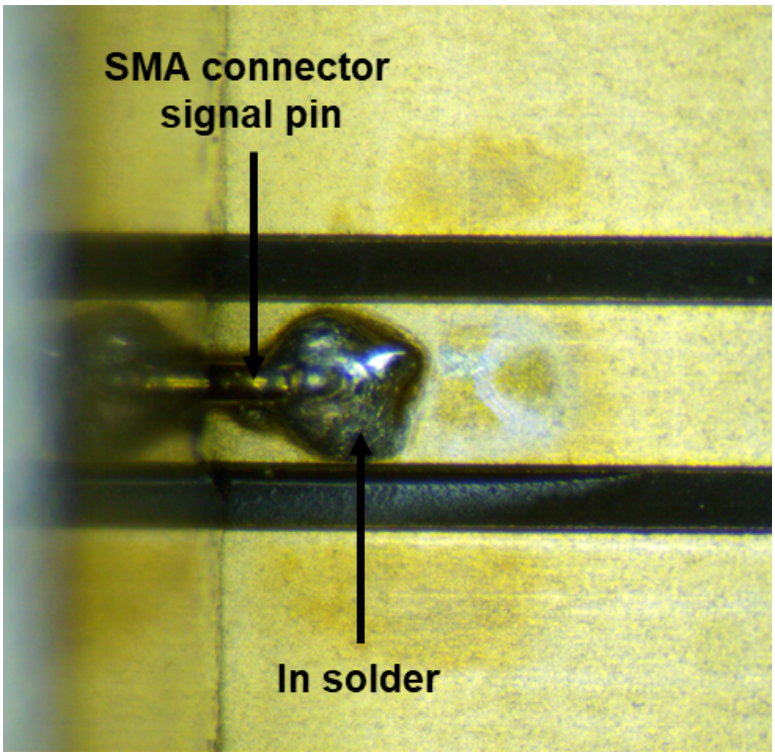

Figure 4.6: The signal pin from the SMA connector was soldered to the signal line on the PCB using In solder. The signal width of CPW trace on the PCB was 400 μm.

Before the assembly, the surface of the PCB and the ground plane on the microstrip resonator were thoroughly cleaned to remove any contaminants or oxide layers that could hinder the bonding process. Isopropyl alcohol (IPA) was used as a cleaning agent for this purpose. IPA effectively removes grease, dirt, and other residues, providing a clean and suitable surface for assembly. Once the cleaning process was completed, an optimum amount of silver paint was applied to the designated area on the PCB. The silver paint, known for its excellent electrical conductivity, acted as a conductive adhesive, facilitating the electrical connection between the resonator sample ground and the PCB ground. The diced resonator sample was carefully positioned and placed onto the silver paint-coated area of the PCB. Precision alignment ensured the accurate placement of the resonator with respect to the CPW lines on the PCB, optimizing signal transmission and minimizing losses.

Following the placement of the resonator sample, the assembly was subjected to a curing process. This involved placing the assembled PCB with the resonator sample in a vacuum oven set to a temperature of 80 °C. The curing process helped to improve the electrical conductivity of the silver paint, enhancing the bond between the PCB and the resonator sample and ensuring a robust electrical connection. The curing duration for this process was approximately one hour. The vacuum environment provided a controlled atmosphere for curing, enabling the silver paint to effectively bond and establish a reliable ground electrical pathway between the PCB and the resonator sample. After the curing of the silver paint, two wire bonds per signal connection were made to reduce the inductance. Gold wire bonds were used to connect the signal lines on the resonator sample to the signal lines on the PCB. The wire bonding process was done using a wire bonding machine, which precisely places and attaches the wire bonds. The wire bonds were then tested to ensure proper electrical connections were made.

Gold wire bonds offer several advantages in terms of electrical conductivity, reliability, and compatibility with the operating conditions required for superconducting structures. Gold is a highly conductive material that allows for efficient signal transmission, minimizing

losses and maintaining signal integrity. Additionally, gold exhibits excellent corrosion resistance, ensuring long-term stability and preventing degradation of the electrical connections [88, 89, 90].

After the wire bonding process was completed, the assembled samples underwent testing to verify the electrical continuity between the PCB and the resonator sample. This testing aimed to ensure proper connections and to confirm the integrity of the signal paths. A multimeter, set to measure resistance or continuity, was used for this purpose. By measuring the resistance or checking for continuity, the multimeter provided a quick and straightforward method to assess the electrical connection between the two components. The testing was conducted at room temperature to evaluate the electrical continuity under typical operating conditions. The multimeter readings were analyzed to confirm that the resistance values were within the expected range, indicating successful electrical connections.

To facilitate the measurements and characterization of the fabricated resonators, edge-mount southwest SMA connectors were mounted onto the PCB. These connectors served as an interface between the cables used for measurements and the resonator sample, enabling convenient and reliable signal transmission. The edge mount SMA connectors were carefully positioned, and screwed to the PCB. The signal pin was soldered onto the designated locations on the PCB. The connectors were aligned with the corresponding signal traces on the CPW structure. Proper alignment ensured accurate signal transfer and minimized any potential signal loss or interference.

During the soldering process, an indium solder was utilized to establish a robust electrical connection between the signal pin of the SMA connector and the CPW signal trace on the PCB. Indium solder is known for its low melting point, which helps prevent excessive heating and potential damage to sensitive components during soldering. By soldering the signal pin of the SMA connector to the signal trace on the CPW, a direct electrical pathway was established, ensuring the efficient transfer of signals between the resonator samples and the measurement equipment.

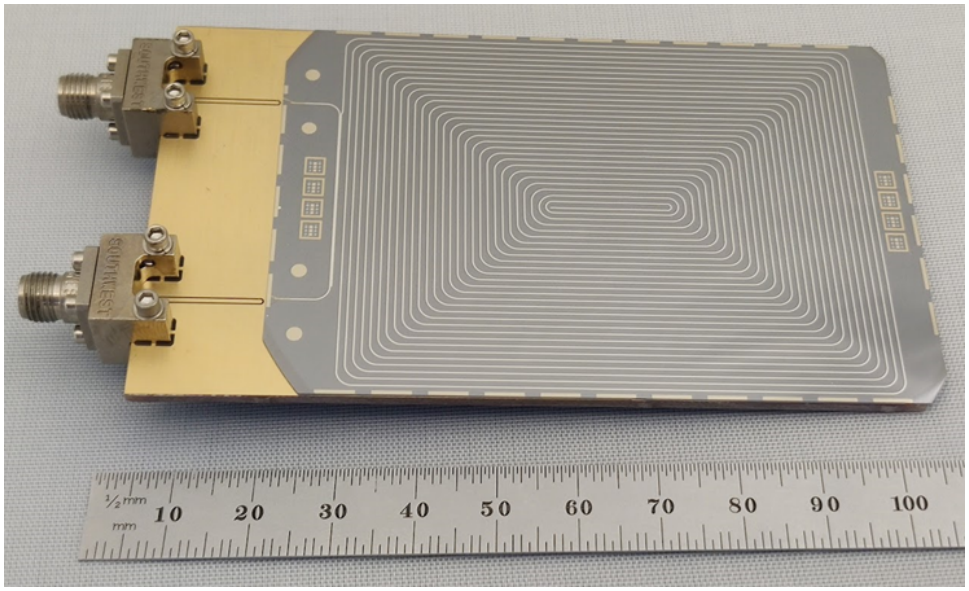

Figure 4.7: Assembled microstrip resonator on the CPW PCB. The signal trace on the silicon was wire bonded to the signal trace on the PCB. Edge-mount southwest SMA connectors were mounted onto the PCB to interface the RF cables and the PCB.

After the successful mounting of the SMA connectors, the fabricated samples were prepared for measurements. This involved attaching coaxial cables to the SMA connectors, which allowed for the transmission of signals between the resonators and the measurement instruments. Fig. 4.7 shows an assembled resonator sample with an Al conductor signal trace.

4.5 Measurements

The measurements were typically carried out at cryogenic temperatures, as the resonators were designed to operate in such conditions. Therefore, the samples were placed in an appropriate cryogenic chamber to achieve the desired low temperatures. Care was taken to ensure proper alignment and secure connections to minimize signal loss or distortion during the measurements.

To perform measurements in liquid helium, a specialized setup was employed. The resonator sample was carefully mounted onto a support board, which was then attached to the end of a vacuum dip probe. The vacuum dip probe provided a means to immerse the sample into the liquid helium dewar while maintaining a controlled environment. Once the

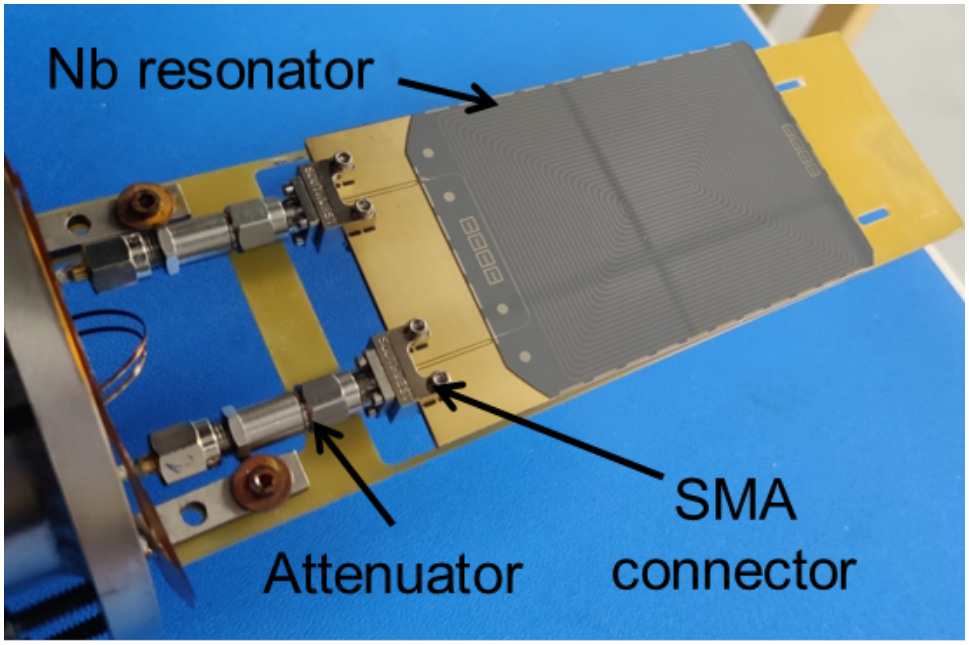

Figure 4.8: Nb resonator sample assembly mounted on a support board and connected to RF cables.

sample was securely mounted, the SMA cables were connected to the SMA connectors on the resonator sample, allowing for the transmission of signals to and from the resonator. Fig. 4.8 shows a Nb resonator sample assembly mounted on a support board and connected to RF cables.

To ensure a tight seal and prevent the ingress of liquid helium, a can was used to enclose and protect the assembly. The can, designed to fit around the mounted sample and support board, provided an additional layer of insulation and safeguarded against any potential contamination or interference during the measurements. To facilitate the cooling process from room temperature to 4.2 K, the vacuum dip probe consisted of two feedthrough connections. These feedthroughs played a crucial role in achieving an efficient and controlled cooldown of the resonator sample. The first feedthrough on the vacuum dip probe was used to establish a vacuum inside the probe. By connecting the feedthrough to a vacuum pump, the pressure inside the dip probe could be reduced to low values. The evacuation of air and other gases from the probe created a vacuum environment, which helped minimize heat transfer through conduction and convection, thus aiding in the cooling process. Once the desired level

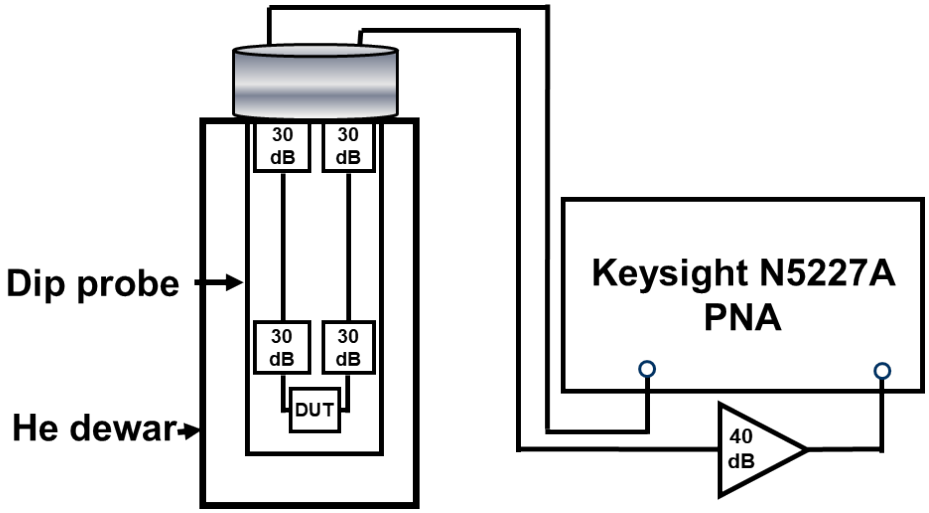

Figure 4.9: Block diagram of the measurement set-up inside the liquid helium dewar. A 60 dB attenuation was applied to both the input and output signal paths, resulting in a total attenuation of 120 dB.

of vacuum was achieved inside the dip probe, the second feedthrough was utilized to introduce an exchange gas, typically helium gas, into the probe. The introduction of the exchange gas served two purposes: firstly, it enhanced the cooling efficiency by facilitating heat transfer between the sample and the cooling medium, and secondly, it ensured a quicker cool-down from room temperature to the desired liquid helium temperature. Before immersing the vacuum dip probe into the liquid helium dewar, a pre-cooldown step was performed in liquid nitrogen. This pre-cooldown in liquid nitrogen served to cool down the sample to a lower temperature range before entering the liquid helium environment. By pre-cooling in liquid nitrogen, the consumption of liquid helium during the cooldown process was minimized, ensuring efficient use of this valuable cryogenic resource.

For measurements in a dilution refrigerator, a different setup was employed to achieve even lower temperatures, typically around 20 mK. This setup involved loading the sample onto a fast sample exchange probe designed specifically for use in a dilution refrigerator. The fast sample exchange probe allowed for quick and efficient transfer of the sample into the dilution refrigerator while maintaining a controlled environment. This ensured that the sample could reach the desired ultra-low temperatures required for precise measurements of

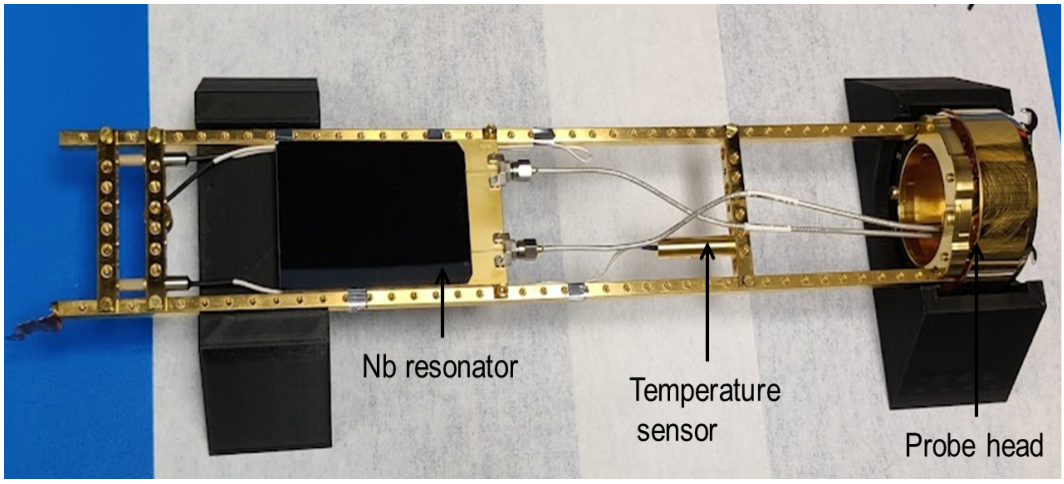

Figure 4.10: A Nb resonator sample assembly screwed to the fast sample exchange probe. The probe is inserted into the dilution refrigerator and cooled down to 20 mK.

the resonances. Fig. 4.10 shows the resonator sample assembly screwed to the fast sample exchange probe.

The cooling process in a dilution refrigerator involved the use of a mixture of isotopes, typically helium-3, and helium-4, to achieve extremely low temperatures. The dilution refrigerator utilized a series of cooling stages, with each stage providing progressively lower temperatures. After loading the sample onto the fast sample exchange probe, the probe was carefully inserted into the dilution refrigerator. The refrigerator's cooling stages, consisting of a mixing chamber and a series of heat exchangers, allowed for the gradual cooling of the sample to temperatures well below 50 mK. Once the sample reached the desired temperature range, the resonances in the Nb and Al samples could be measured. It's important to note that measurements in the dilution refrigerator were typically conducted for both Nb and Al samples, while measurements in liquid helium dewar were limited to Nb samples.

For the measurement of resonances in both the helium dewar and dilution refrigerator, a PNA was used. To ensure accurate and reliable measurements, the signal path from the PNA to the resonator samples was carefully controlled and attenuated. In both the helium dewar and dilution refrigerator setups, the signal path was attenuated by 60 dB. This attenuation level was chosen to significantly reduce the signal power reaching the resonator samples. It's

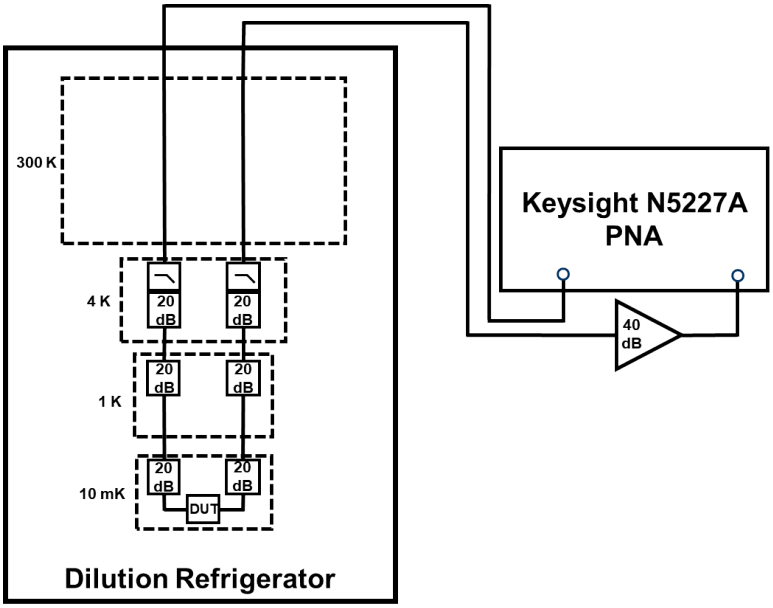

Figure 4.11: Block diagram of the measurement set-up showing dilution refrigerator and the components in the signal input-output paths. A 60 dB attenuation was applied to both the input and output signal paths, resulting in a total attenuation of 120 dB.

important to note that the attenuation was applied to both the input and output signal paths, resulting in a total attenuation of 120 dB. This extensive attenuation helped ensure that the measurements were performed at extremely low powers, which is crucial for qubit measurements and to prevent unwanted effects such as nonlinear behavior or heating of the samples.

By employing such a high level of attenuation, the measurements were conducted in a regime where the resonators were effectively probed without introducing excessive power or perturbations that could potentially affect their behavior. This allowed for precise characterization of the resonance frequencies, quality factors, and other electrical properties of the fabricated resonators.

4.6 Results

The resonators fabricated with Nb and Al superconducting material were subjected to measurements at a temperature of 4.2 K and 20 mK to investigate their performance

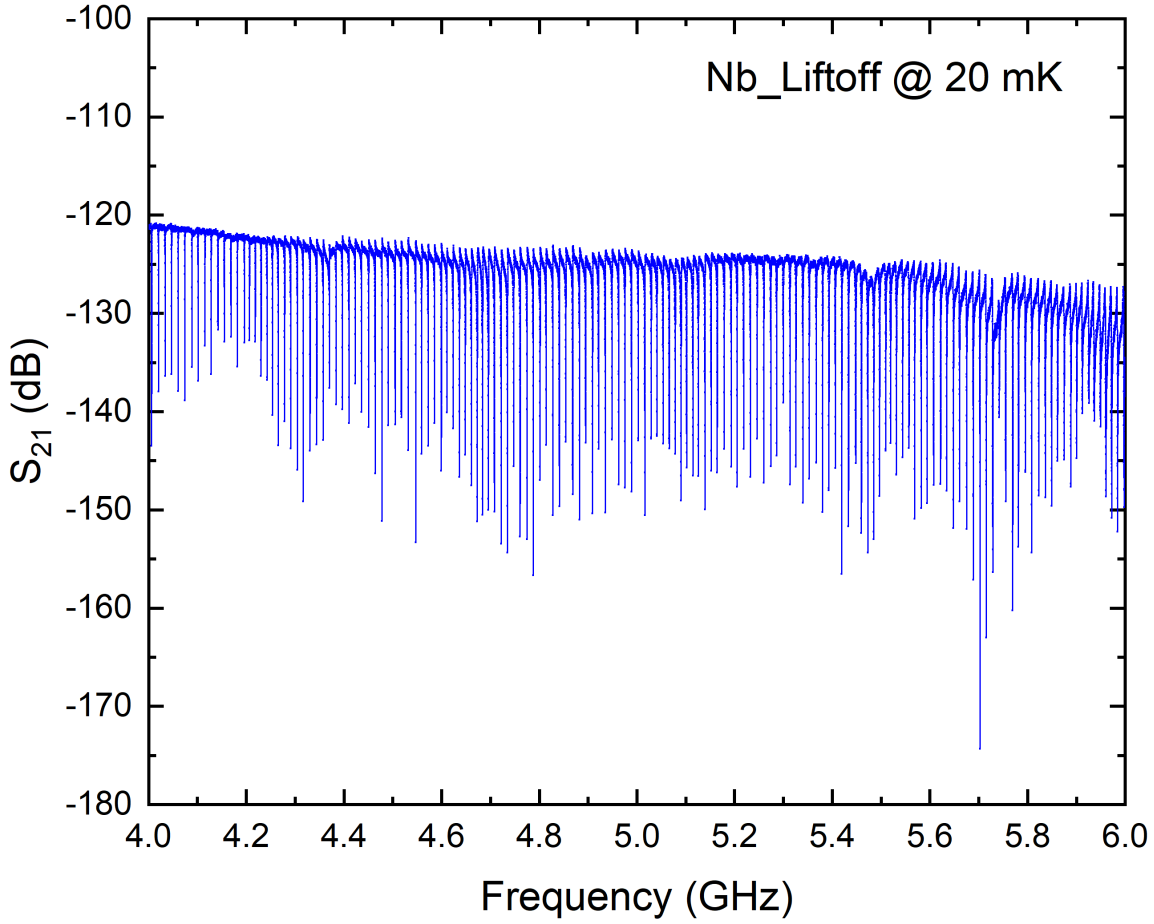

Figure 4.12: S_{21} response of the Nb resonator sample fabricated using the liftoff process. The plot shows a frequency spectrum between 4-6 GHz, the usual operating frequency of the qubit in a quantum system. The response is without any amplification at the output end. The individual resonance frequency data was obtained with the amplifier to reduce the averaging number, which reduces the measurement time of each resonance frequency. It can be observed that the resonators exhibit distinct resonance peaks at different frequencies.

characteristics. The S_{21} response, which represents the transmission coefficient, was measured for each resonator sample. The results obtained from these measurements provide valuable insights into the resonance behavior and performance of the Nb resonators at cryogenic temperatures. The resonance frequencies of the Nb resonators were determined by analyzing the S_{21} response. Fig. 4.12 and Fig. 4.13 show the frequency spectrum obtained from the measurements at 4.2 K and 20 mK, respectively. It can be observed that the resonators exhibit distinct resonance peaks at different frequencies and at different temperatures.

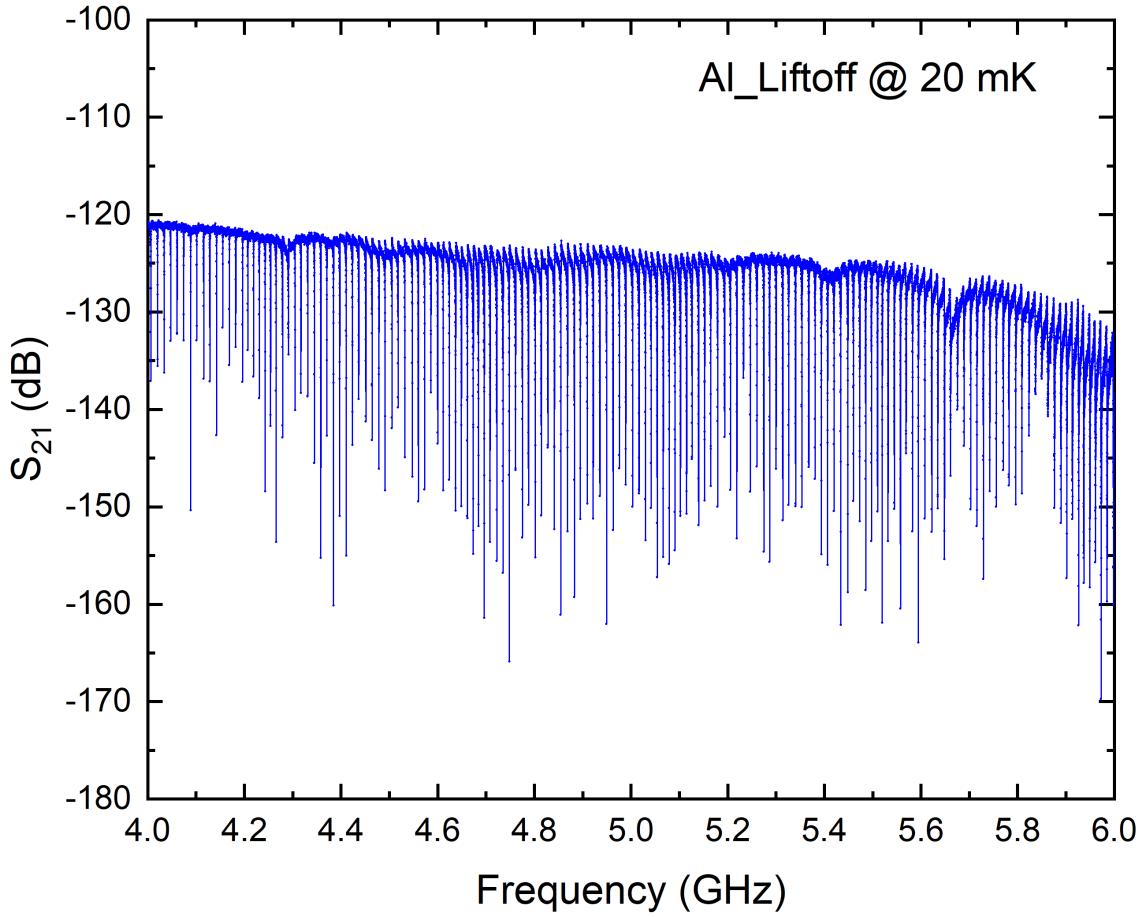

Figure 4.13: S_{21} response of the Al resonator sample fabricated using the liftoff process. The plot shows resonances between 4-6 GHz, the usual operating frequency of the qubit in a quantum system. The response is without any amplification at the output end. The individual resonance frequency data was obtained with the amplifier to reduce the averaging number, which reduces the measurement time of each resonance frequency.

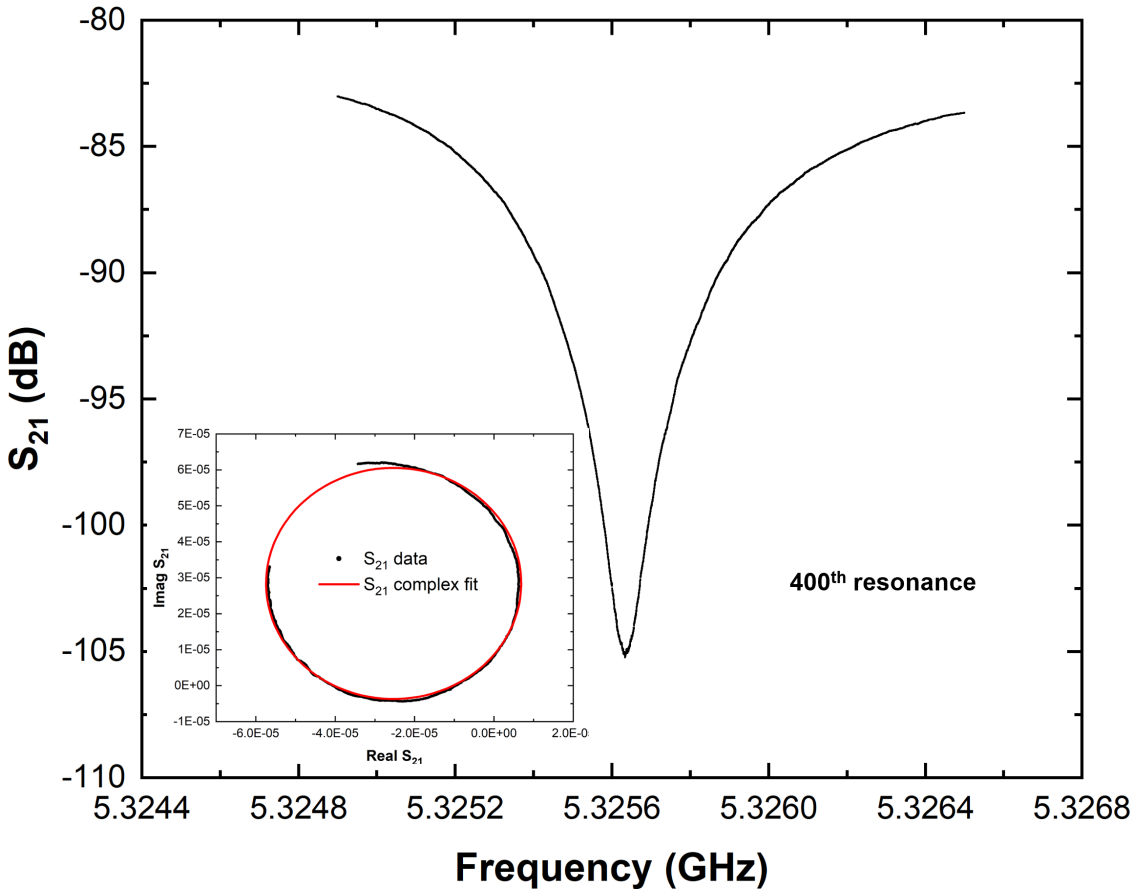

Figure 4.14: 400^{th} resonance of the Nb resonator sample measured in dilution refrigerator at 20 mK. The plotted response is through a 40 dB amplifier at the output line. The inset plot shows the resonance data projected onto the complex plane as a circle. The uncertainty on the fit was reduced by decreasing the noise level (averaging factor of 300 was used) and by increasing the number of data points of the measurement (30000 data points).

The Q of the resonators was determined by employing the circle fit algorithm as described in [91]. This algorithm offers a reliable approach for extracting accurate Q values from complex scattering data, even in the presence of noise. The application of the circle fit algorithm ensured accurate and robust determination of the Q values, even in the presence of noise or uncertainties in the measurement data. This approach significantly enhances the reliability of the Q value analysis and provides valuable insights into the loss characteristics and performance of the resonators at cryogenic temperatures. Fig. 4.15 shows the comparison of loss vs. frequency between the Nb samples fabricated using different fabrication processes at 4.2 K. The plots indicate the etching process, which provides an isotropic etch profile for defining the signal layer showed less loss compared to the liftoff process. Fig. 4.16 shows the difference in the loss vs. frequency between the Nb samples fabricated using different fabrication processes at 4.2 K.

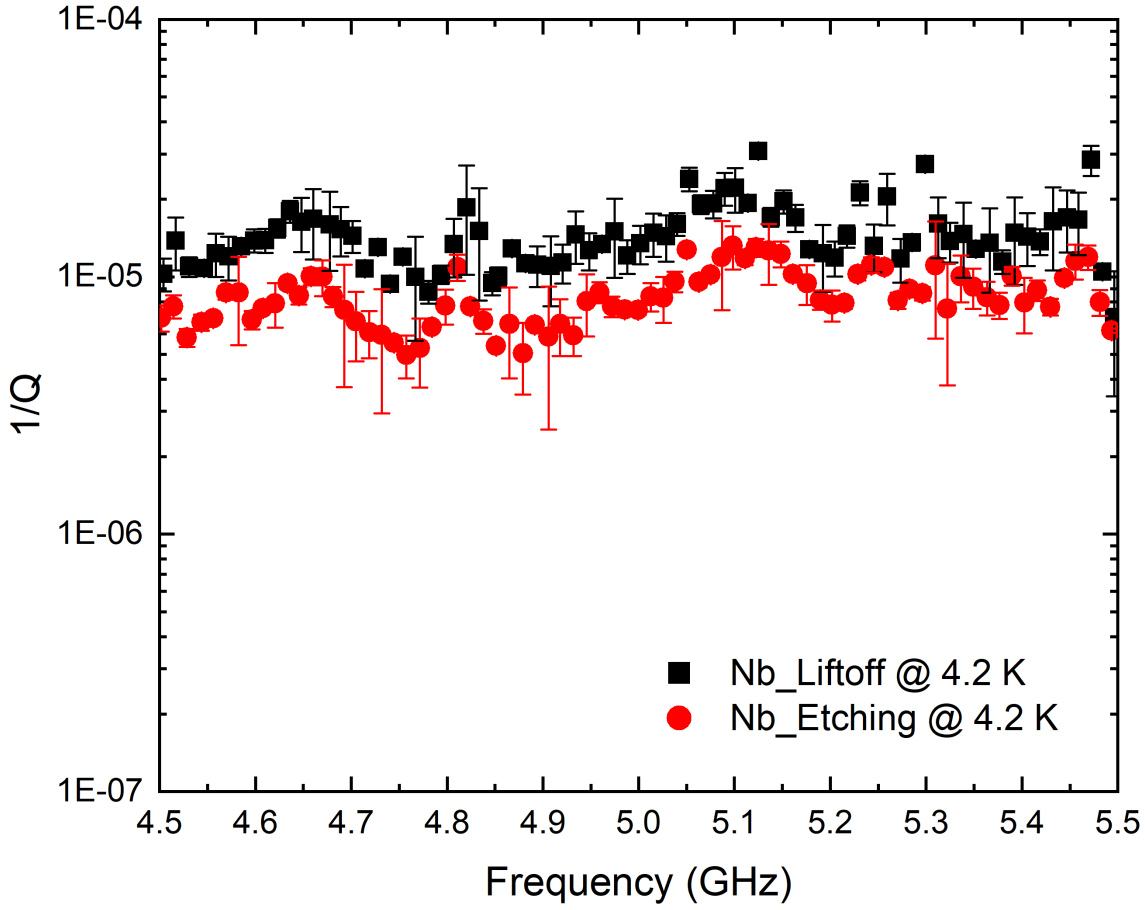

Figure 4.15: Comparison of loss vs. frequency of the Nb sample at 4.2 K fabricated using different processes.

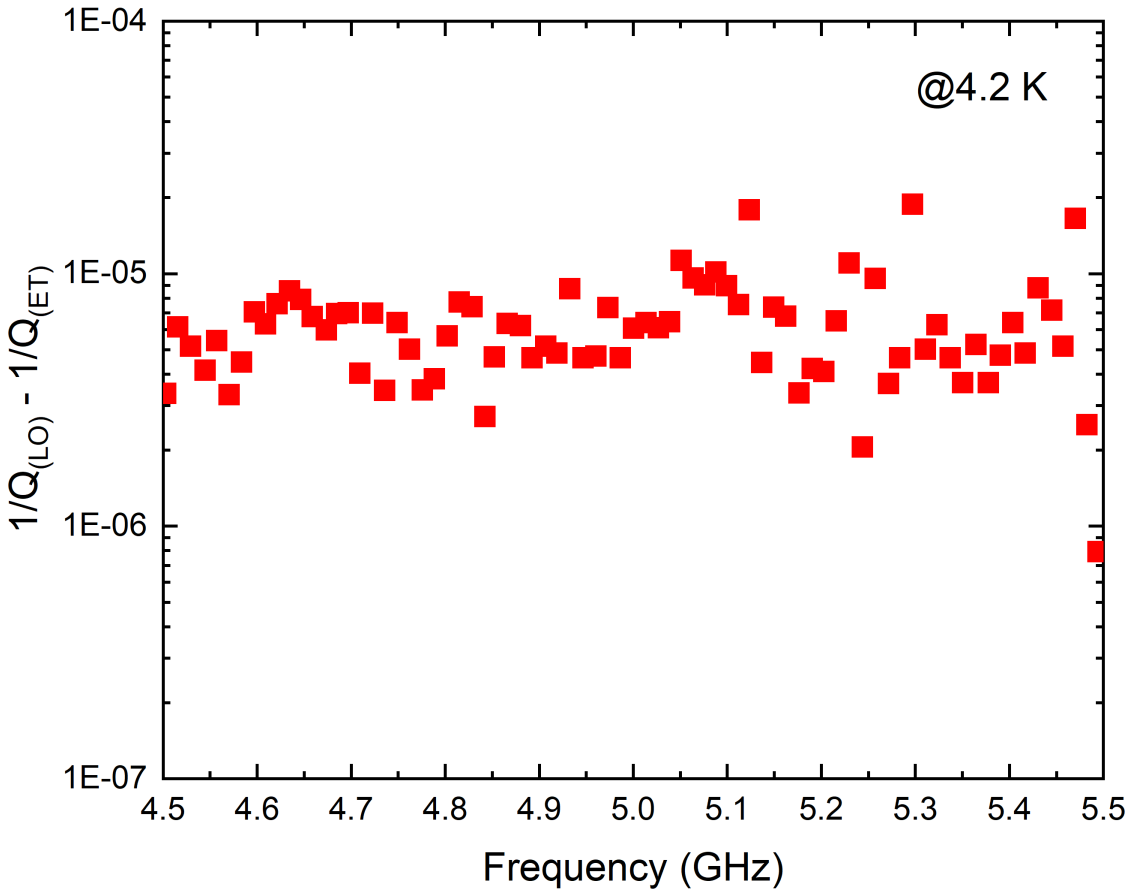

Figure 4.16: Difference in the loss vs. frequency of the Nb sample at 4.2 K fabricated using different processes. The plot indicates the increase in loss when the resonator samples were fabricated using the liftoff process. LO is the liftoff process and ET is the etching process.

After completing the measurements in the helium dewar, the Nb samples were further characterized in a dilution refrigerator. This transition allowed for investigations of the resonator properties at even lower temperatures, approaching the mK range. The dilution refrigerator provided a highly stable and controlled environment, enabling precise temperature control and minimizing thermal noise effects. By transferring the samples from the helium dewar to the dilution refrigerator, a comprehensive analysis of the resonator performance across a wider temperature range was achieved. This step provided valuable insights into the behavior of the Nb resonators at ultra-low temperatures and allowed for comparisons with the measurements conducted in the helium dewar setup. Fig. 4.17 shows the comparison of loss vs. frequency between the Nb samples fabricated using different fabrication processes at 20 mK. The plots indicate the etching process, which provides an isotropic etch profile for defining the signal layer showed less loss compared to the liftoff process. Fig. 4.18 shows the difference in the loss vs. frequency between the Nb samples fabricated using different fabrication processes at 20 mK.

Fig. 4.19 shows the comparison of loss vs. frequency between the Nb samples fabricated using different fabrication processes at 20 mK. The plots indicate the etching process, which provides an isotropic etch profile for defining the signal layer showed less loss compared to the liftoff process. Fig. 4.20 shows the difference in the loss vs. frequency between the Al samples fabricated using different fabrication processes at 20 mK.

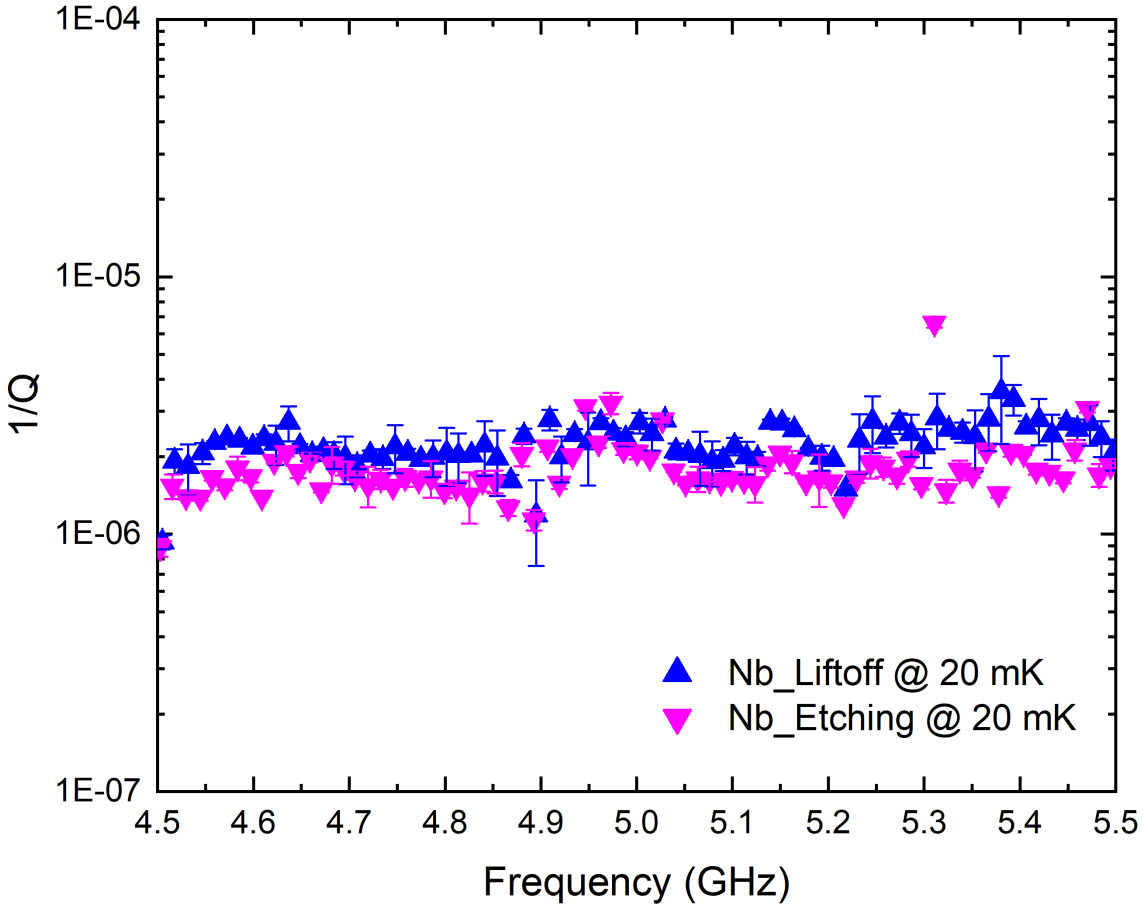

Figure 4.17: Comparison of loss vs. frequency of the Nb sample at 20 mK fabricated using different processes.

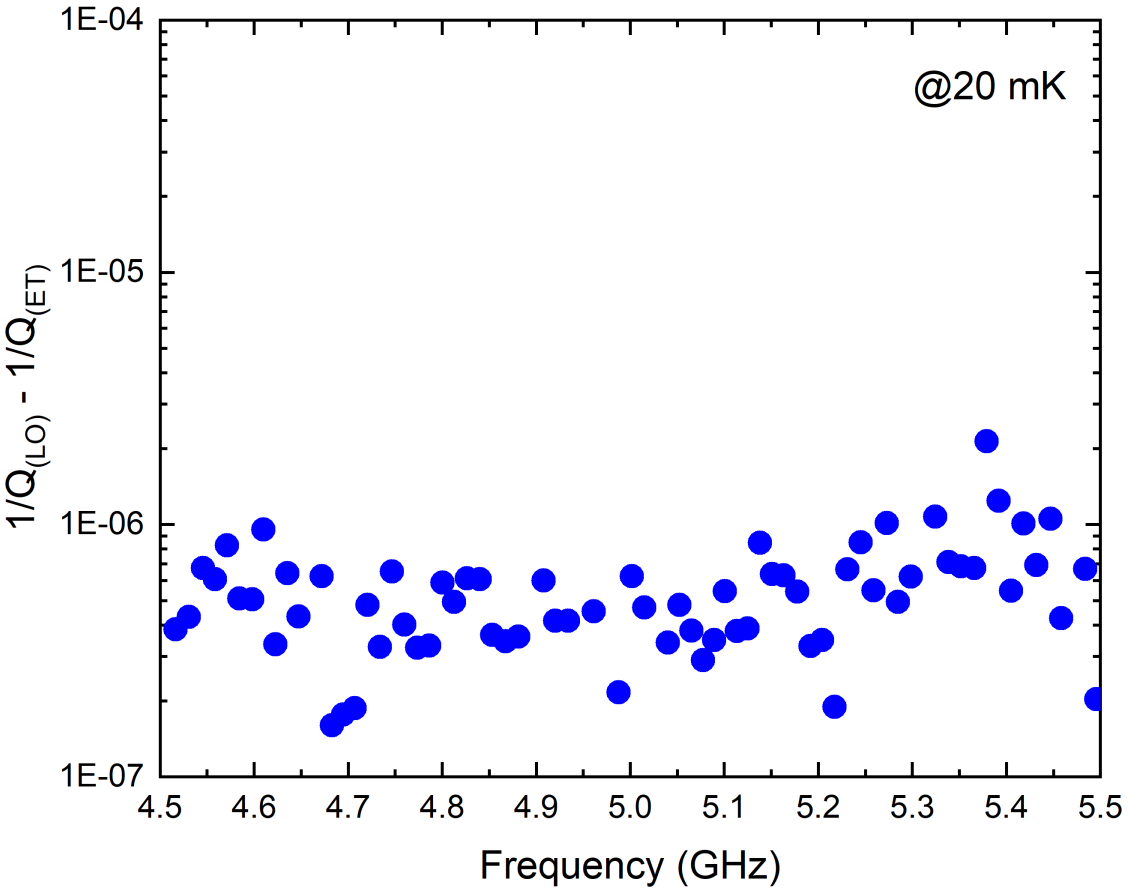

Figure 4.18: Difference in the loss vs. frequency of the Nb sample at 20 mK fabricated using different processes. LO is the liftoff process and ET is the etching process.

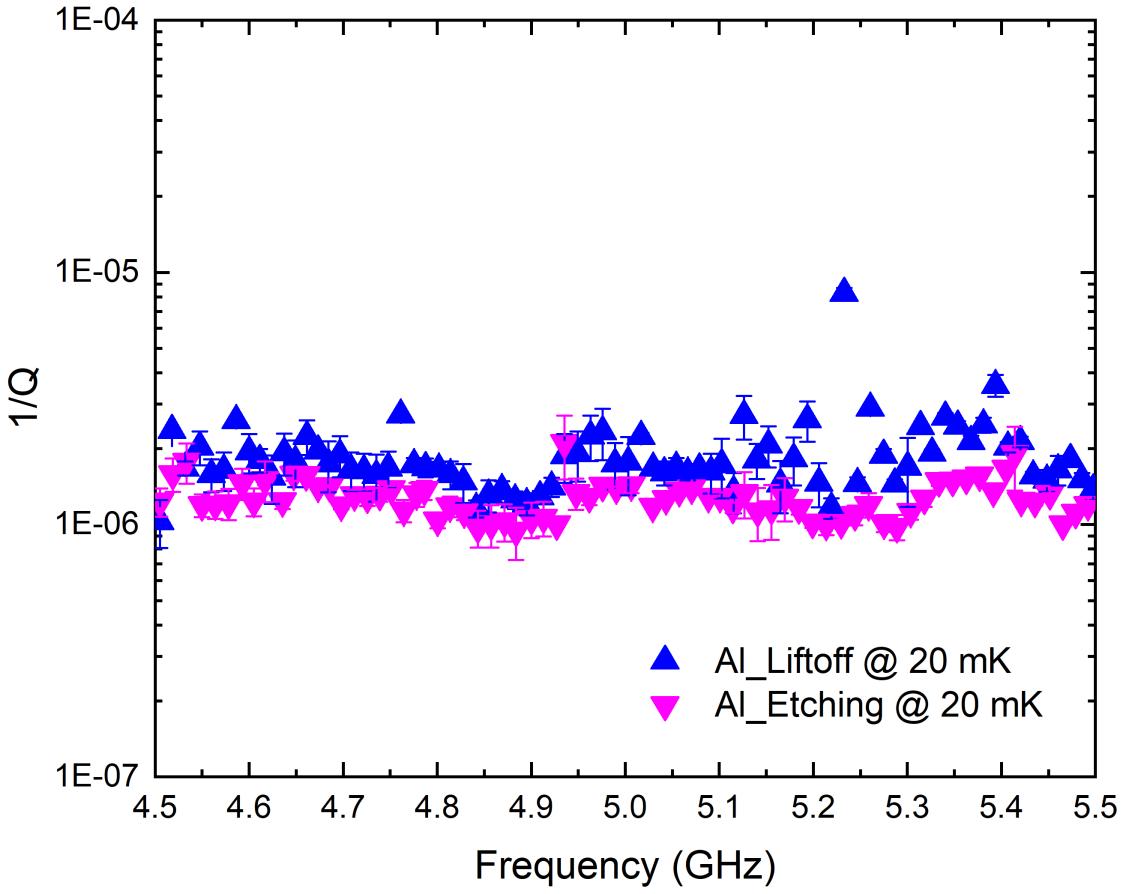

Figure 4.19: Comparison of loss vs. frequency of the Al sample at 20 mK fabricated using different processes.

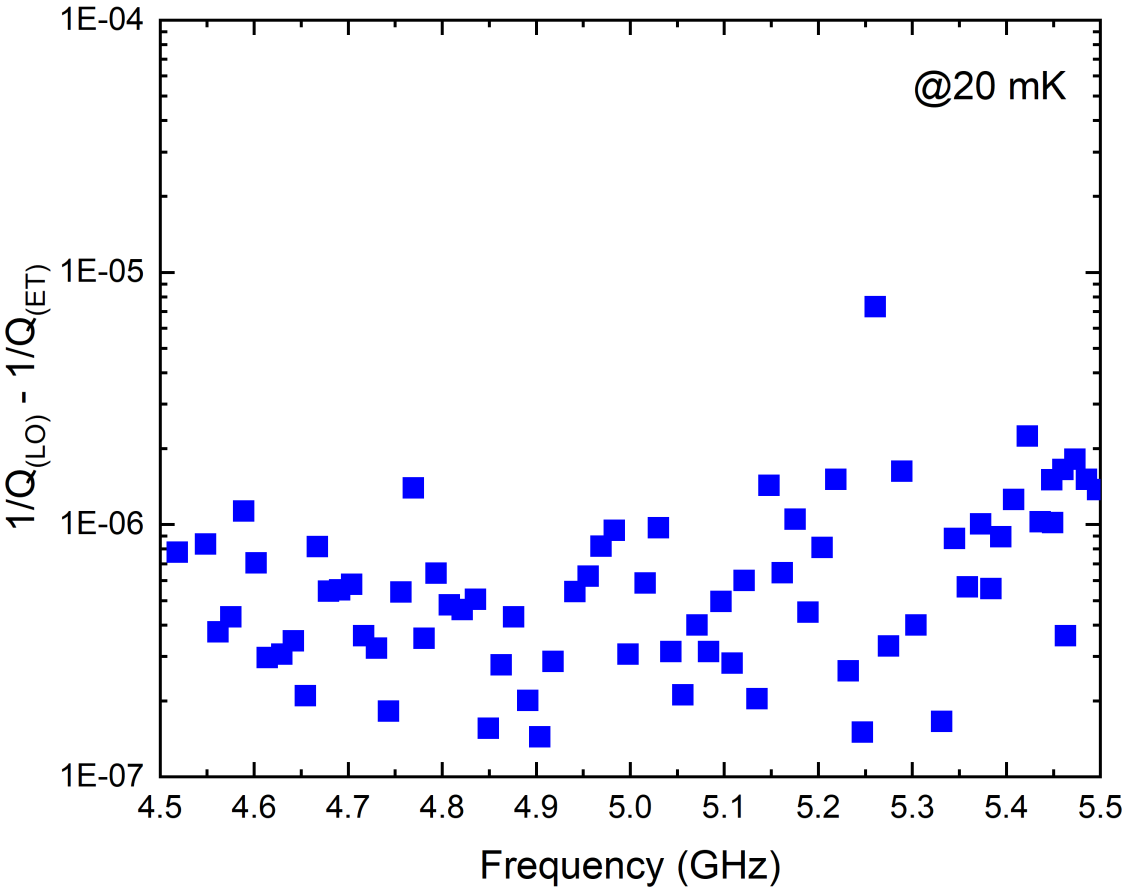

Figure 4.20: Difference in the loss vs. frequency of the Al sample at 20 mK fabricated using different processes. LO is the liftoff process and ET is the etching process.

4.7 Summary

In summary, this study focused on characterizing material losses in superconducting structures at cryogenic temperatures using very long resonators. The use of these resonators provided a fine resonance frequency spectrum, which proved to be a valuable tool for identifying material losses at various frequencies and optimizing fabrication procedures for quantum computation applications.

Structures and approaches similar to those discussed provide a means to investigate and connect deep cryogenic materials losses and relevant fabrication processes over a wide frequency range with very closely spaced measurement points. By carefully designing and fabricating resonators, we can accurately measure and analyze material losses, enabling a comprehensive understanding of the underlying mechanisms and their impact on device performance.

Through a comprehensive design and fabrication process, involving the use of intrinsic silicon wafers as the substrate material, and employing different fabrication procedures for both Nb and Al resonators, I successfully created resonator structures suitable for low-temperature measurements. The liftoff process and etching process were employed, and detailed steps were taken to ensure the precise deposition and patterning of the resonator structures. Measurements were conducted at different temperatures, including 4.2 K and 20 mK, utilizing both helium dewar and dilution refrigerator setups. The resonator performance was characterized through S_{21} response measurements, providing valuable insights into the quality factors and resonance frequencies of the Nb and Al resonators. The results obtained from this study contribute to the understanding of material losses in superconducting structures and offer valuable insights for the design and fabrication of high-performance resonators in the field of quantum computation. By optimizing fabrication procedures and identifying the best materials and processes, we can enhance the performance of superconducting structures and improve the reliability and efficiency of quantum computation systems.

Future work could involve further refining the fabrication processes, exploring different materials, and investigating the impact of different design parameters on the resonator performance. Additionally, exploring the effects of material losses on qubit coherence and implementing these resonators within quantum computing architectures would be crucial for advancing the field.

Overall, this research provides valuable contributions to the field of superconducting resonator design and fabrication, shedding light on the material losses at cryogenic temperatures and paving the way for the development of high-performance superconducting structures for quantum computation applications. Structures and approaches similar to those discussed provide a means to investigate and connect deep cryogenic materials losses and relevant fabrication processes over a wide frequency range with very closely spaced measurement points, enabling comprehensive studies in the field of superconducting devices and quantum computation.

Chapter 5

Conclusion

In conclusion, this dissertation has addressed the signal integrity challenges faced by electronic systems operating in cryogenic environments and has explored solutions to mitigate these challenges. The research has provided valuable insights into the unique physical properties of materials at cryogenic temperatures, including changes in conductivity, dielectric loss tangent, and quality factor of the resonators. Through theoretical analysis, simulation, and experimental investigation, this study has made significant contributions to our understanding of signal propagation and degradation in extreme low-temperature conditions and extremely harsh environments, such as gamma radiation.

The proposed solutions presented in this dissertation have practical implications for the design and development of electronic systems in cryogenic applications. Special low-temperature cables and connectors have been identified as effective means to minimize signal attenuation and noise. The selection of materials with low loss tangent and high thermal conductivity has proven crucial in maintaining signal integrity at cryogenic temperatures. Additionally, the optimization of thermal management techniques, such as the use of cryogenic cooling systems and insulation, has been shown to reduce thermal gradients and minimize the degradation of signal quality.

The face-to-face cable connection scheme using flexible thin-film superconducting stripline cables focused on mitigating impedance discontinuities, crosstalk, signal loss, and power dependency. All the traces on the flex cables in the assembly transitioned to a superconducting state with a critical transition temperature over a range of 8.6-9.0 K and the measurements for critical current showed an average value in the range of 10-10.5 mA for all 12 face-to-face signal contacts with loop-backs resulting in six testable signal lines in the assembly.

Through time domain reflectometry measurements, impedance jumps at the signal contact points were identified and minimized, ensuring minimal signal reflections and preserving signal integrity. The design and optimization of the assembly effectively reduced crosstalk, resulting in reliable signal transmission. Moreover, the measurements demonstrated minimal signal loss and stable signal characteristics, even with varying power levels. By successfully resolving these signal integrity challenges, this work provides valuable contributions to the development of robust and high-performance signal pathways for cryogenic and quantum technology applications.

The investigation into the impact of gamma radiation on superconducting microstrip resonators has provided valuable insights into signal integrity challenges at cryogenic temperatures. The observed minimal changes in the quality factors of the Nb embedded resonators and Al/Nb/Al embedded resonators following radiation exposure up to 564 kGy indicate the inherent resilience of these devices to gamma radiation. While some minor degradation was observed, it is noteworthy that the resonators maintained their performance to a significant extent. These findings suggest that superconducting microstrip resonators exhibit promising characteristics in terms of signal integrity preservation under radiation-intensive environments. Nonetheless, continued efforts are necessary to understand the underlying mechanisms and optimize the design parameters for even greater resilience. Future research can focus on further minimizing radiation-induced changes in the Q values through advanced shielding techniques, material optimizations, and radiation-hardening strategies. By addressing these signal integrity challenges and enhancing the robustness of superconducting devices in extreme environments, we can advance the development of reliable cryogenic systems for various applications, including space missions and nuclear facilities.

The work on the very long resonators has focused on the design, fabrication, and characterization to investigate material losses in superconducting structures at cryogenic temperatures. By utilizing these resonators, I have been able to achieve a fine resonance frequency

spectrum, allowing us to accurately identify and characterize material losses at various frequencies. Through a meticulous design and fabrication process, involving the use of intrinsic silicon wafers as the substrate material and employing different fabrication procedures for both Nb and Al resonators, I have successfully developed resonator structures suitable for low-temperature measurements. The measurements were conducted at different temperatures, utilizing both helium dewar and dilution refrigerator setups. The obtained results, including the resonance frequencies and quality factors, have provided valuable insights into the energy storage and dissipation properties of the resonators. Furthermore, this work has demonstrated the importance of optimizing fabrication procedures and selecting appropriate materials for the development of high-performance superconducting structures for quantum computation applications. By identifying and characterizing material losses at different frequencies, it becomes possible to understand the frequency-dependent behavior of the superconducting structures. This knowledge can be utilized to mitigate frequency-dependent losses, ensuring consistent signal integrity across the desired frequency range. The findings from this research contribute to the broader field of superconducting device design and fabrication, offering a pathway towards the realization of efficient and reliable quantum computation systems.

In conclusion, this dissertation has successfully addressed the signal integrity challenges and presented effective solutions for electronic systems operating in cryogenic environments. The research outcomes have practical implications for a wide range of cryogenic applications, including quantum computing, superconducting electronics, and space exploration. By overcoming the signal integrity challenges associated with cryogenic temperatures, the reliability and performance of electronic systems in these applications can be significantly improved. This research contributes to the advancement of cryogenic electronics and serves as a stepping stone for future studies in this emerging field.

It is important to note that this dissertation has provided a comprehensive understanding of signal integrity challenges and solutions at cryogenic temperatures. However, further

research is encouraged to explore additional aspects, such as the impact of cryogenic temperatures on other electronic components and subsystems, as well as the development of novel materials and techniques specifically tailored for cryogenic signal integrity.

Overall, this dissertation contributes to the body of knowledge in the field of signal integrity in cryogenic environments and provides valuable insights and practical recommendations for the design and development of electronic systems operating in extreme low-temperature conditions. The research outcomes will serve as a guide for engineers and researchers working on cryogenic applications, fostering advancements in this exciting and rapidly evolving field.

Chapter 6

Future Work

One potential avenue for future work is the investigation of advanced signal integrity techniques and designs for even higher data rates and denser signal integration in cryogenic and quantum technology applications. This could involve exploring longer transmission line structures with multiple interconnects and optimizing their performance in extremely low-temperature environments. Additionally, further research can be conducted to study the effects of electromagnetic interference (EMI) and noise on signal integrity in cryogenic systems, with the aim of developing effective shielding and filtering techniques. Experimental studies can be conducted to characterize the performance of different materials and their suitability for high-speed signal transmission in extreme low-temperature conditions. Lastly, the scalability and reliability of the proposed face-to-face cable connection scheme can be evaluated by expanding the system to larger-scale applications and conducting long-term reliability tests. This would provide insights into the practical implementation and potential deployment of the proposed signal integrity solutions in real-world cryogenic and quantum technology environments.

The long-term effects of radiation exposure on superconducting microstrip resonators, including the stability and reliability of performance over extended operational lifetimes should be explored. Additionally, assessing the effects of other radiation sources, such as alpha particles, beta particles, or neutron radiation, would provide a comprehensive understanding of the resonators' behavior. Furthermore, exploring the integration of superconducting microstrip resonators with digital systems operating at cryogenic temperatures would shed light on their compatibility and performance in complex computing technologies.

The research work on the long superconducting resonators can be extended by exploring alternative fabrication techniques, such as atomic layer deposition or physical vapor deposition, to optimize the performance of superconducting structures. Additionally, a broader range of materials should be characterized to understand their losses and performance at cryogenic temperatures. Tantalum has been gaining importance in recent times for cryogenic and quantum applications [92, 93, 94, 95]. Integrating advanced signal integrity techniques, including impedance matching networks and cryogenic amplifiers, can further enhance signal quality. The impact of packaging and interconnects on signal integrity should be studied, and novel materials and structures, like superconducting metamaterials, should be investigated. By addressing these areas, researchers can advance the understanding of signal integrity challenges and contribute to more efficient systems for quantum computation and superconductivity applications.

Bibliography

[1] Theodore Van Duzer. Superconductor electronics, 1986-1996. *IEEE transactions on applied superconductivity*, 7(2):98–111, 1997.

[2] John M Rowell. Recommended directions of research and development in superconducting electronics. *IEEE transactions on applied superconductivity*, 9(2):2837–2848, 1999.

[3] Keith C Schwab and Michael L Roukes. Putting mechanics into quantum mechanics. *Physics Today*, 58(7):36–42, 2005.

[4] S Anders, MG Blamire, F-Im Buchholz, D-G Crété, R Cristiano, P Febvre, L Fritzsch, Anna Herr, E Il'Ichev, J Kohlmann, et al. European roadmap on superconductive electronics–status and perspectives. *Physica C: Superconductivity*, 470(23-24):2079–2126, 2010.

[5] Farzan Jazaeri, Arnout Beckers, Armin Tajalli, and Jean-Michel Sallese. A review on quantum computing: From qubits to front-end electronics and cryogenic mosfet physics. In *2019 MIXDES-26th International Conference" Mixed Design of Integrated Circuits and Systems"*, pages 15–25. IEEE, 2019.

[6] Rakshith Saligram, Suman Datta, and Arijit Raychowdhury. Design space exploration of interconnect materials for cryogenic operation: Electrical and thermal analyses. *IEEE Transactions on Circuits and Systems I: Regular Papers*, 69(11):4610–4618, 2022.

[7] Richard G Geyer and Jerzy Krupka. Microwave dielectric properties of anisotropic materials at cryogenic temperatures. *IEEE transactions on instrumentation and measurement*, 44(2):329–331, 1995.

[8] CH Wu, F Tan, MK Wu, M Feng, and N Holonyak. The effect of microcavity laser recombination lifetime on microwave bandwidth and eye-diagram signal integrity. *Journal of Applied Physics*, 109(5):053112, 2011.

[9] Kangmin Zhou, Sylvain Caroopen, Yan Delorme, Michele Batrung, Maurice Gheudin, and Shengcai Shi. Dielectric constant and loss tangent of silicon at 700–900 ghz at cryogenic temperatures. *IEEE Microwave and Wireless Components Letters*, 29(7):501–503, 2019.

[10] R Radebaugh and JD Siegwarth. Dilution refrigerator technology. *Cryogenics*, 11(5):368–384, 1971.

[11] Maowen Zheng, Jia Quan, Nailiang Wang, Chengzhan Li, Miguang Zhao, Lingjiao Wei, and Jingtao Liang. A brief review of dilution refrigerator development for space applications. *Journal of Low Temperature Physics*, 197:1–9, 2019.

[12] H Zu, W Dai, and ATAM de Waele. Development of dilution refrigerators—a review. *Cryogenics*, 121:103390, 2022.

[13] HJ Van Weers, G Kunkel, MA Lindeman, and M Leeman. Niobium flex cable for low temperature high density interconnects. *Cryogenics*, 55:1–4, 2013.

[14] Alex B Walter, Clinton Bockstiegel, Benjamin A Mazin, and Miguel Daal. Laminated nbti-on-kapton microstrip cables for flexible sub-kelvin rf electronics. *IEEE Transactions on Applied Superconductivity*, 28(1):1–5, 2017.

[15] Simin Zou, Bhargav Yelamanchili, Vaibhav Gupta, John A Sellers, Tamara Isaacs-smith, David B Tuckerman, and Michael C Hamilton. Low-loss cable-to-cable parallel connection method for thin-film superconducting flexible microwave transmission lines. *Superconductor Science and Technology*, 32(7):075006, 2019.

[16] Jennifer Pearl Smith, Benjamin A Mazin, Alex B Walter, Miguel Daal, JI Bailey III, Clinton Bockstiegel, Nicholas Zobrist, Noah Swimmer, Sarah Steiger, and Neelay Fruitwala. Flexible coaxial ribbon cable for high-density superconducting microwave device arrays. *IEEE Transactions on Applied Superconductivity*, 31(1):1–5, 2020.

[17] Charles P. Poole Jr. and Horacio A. Farach. *Introduction to Superconductivity.* Wiley-VCH, 1995.

[18] Stephen J. Blundell. *Superconductivity: A Very Short Introduction.* Oxford University Press, 2009.

[19] K.H. Bennemann and J.B. Ketterson. *Superconductivity.* Springer-Verlag, 2008.

[20] J. Robert Schrieffer. *High-Temperature Superconductors.* Addison-Wesley, 1999.

[21] Yun Zhang. *Oxide and Metallic Precursor Powders for Bi 2 Sr 2 CaCu 2 O x/Ag Round Wires.* PhD thesis, North Carolina State University, 2015.

[22] Michael Tinkham. *Introduction to Superconductivity.* Dover Publications, 2nd edition, 2004.

[23] T. H. Geballe and B. T. Matthias. Superconductivity of metals and alloys. *Physics Today*, 25(6):38, 1972.

[24] Siti Fatimah Saipuddin, Azhan Hashim, and Nurbaisyatul Ermiza Suhaimi. *Type I and Type II Superconductivity*, pages 123–146. Springer Nature Singapore, Singapore, 2022.

[25] Zahid Hussain and Asma Talib. Strengths and weaknesses of quantum computing. *International Journal of Scientific and Engineering Research*, 7, 2016.

[26] Dietrich Leibfried, Rainer Blatt, Christopher Monroe, and David Wineland. Quantum dynamics of single trapped ions. *Reviews of Modern Physics*, 75(1):281, 2003.

[27] Rainer Blatt and Christian F Roos. Quantum simulations with trapped ions. *Nature Physics*, 8(4):277–284, 2012.

[28] Philip Krantz, Morten Kjaergaard, Fei Yan, Terry P Orlando, Simon Gustavsson, and William D Oliver. A quantum engineer's guide to superconducting qubits. *Applied Physics Reviews*, 6(2):021318, 2019.

[29] Morten Kjaergaard, Mollie E Schwartz, Jochen Braumüller, Philip Krantz, Joel I-J Wang, Simon Gustavsson, and William D Oliver. Superconducting qubits: Current state of play. *Annual Review of Condensed Matter Physics*, 11:369–395, 2020.

[30] Göran Wendin. Quantum information processing with superconducting circuits: a review. *Reports on Progress in Physics*, 80(10):106001, 2017.

[31] JQ You and Franco Nori. Superconducting circuits and quantum information. *arXiv preprint quant-ph/0601121*, 2006.

[32] PD Nation, JR Johansson, MP Blencowe, and Franco Nori. Colloquium: Stimulating uncertainty: Amplifying the quantum vacuum with superconducting circuits. *Reviews of Modern Physics*, 84(1):1, 2012.

[33] Xi-Lin Wang, Yi-Han Luo, He-Liang Huang, Ming-Cheng Chen, Zu-En Su, Chang Liu, Chao Chen, Wei Li, Yu-Qiang Fang, Xiao Jiang, et al. 18-qubit entanglement with six photons' three degrees of freedom. *Physical review letters*, 120(26):260502, 2018.

[34] He-Liang Huang, Qi Zhao, Xiongfeng Ma, Chang Liu, Zu-En Su, Xi-Lin Wang, Li Li, Nai-Le Liu, Barry C Sanders, Chao-Yang Lu, et al. Experimental blind quantum computing for a classical client. *Physical review letters*, 119(5):050503, 2017.

[35] Hui Wang, Jian Qin, Xing Ding, Ming-Cheng Chen, Si Chen, Xiang You, Yu-Ming He, Xiao Jiang, L You, Z Wang, et al. Boson sampling with 20 input photons and a 60-mode interferometer in a 1 0 14-dimensional hilbert space. *Physical review letters*, 123(25):250503, 2019.

[36] Bruce E Kane. A silicon-based nuclear spin quantum computer. *nature*, 393(6681):133–137, 1998.

[37] Yu He, SK Gorman, Daniel Keith, Ludwik Kranz, JG Keizer, and MY Simmons. A two-qubit gate between phosphorus donor electrons in silicon. *Nature*, 571(7765):371–375, 2019.

[38] Yasunobu Nakamura, Yu A Pashkin, and JS Tsai. Coherent control of macroscopic quantum states in a single-cooper-pair box. *nature*, 398(6730):786–788, 1999.

[39] Saniya Deshpande, Jean-Phillip Paquette, Mehrnoosh Vahidpour, Michael Selvanayagam, Rob Lion, Michael Pelstring, Shane Caldwell, Matthew Reagor, and Damon Russell. Integrating high-density microwave signalling and packaging with superconducting qubits. In *2019 IEEE MTT-S International Microwave Symposium (IMS)*, pages 271–274. IEEE, 2019.

[40] Vaibhav Gupta, Bhargav Yelamanchili, Simin Zou, Tamara Isaacs-Smith, John A Sellers, David B Tuckerman, and Michael C Hamilton. Thin-film nb/polyimide superconducting stripline flexible cables. *IEEE Transactions on Applied Superconductivity*, 29(5):1–5, 2019.

[41] M. Mehendale and J. Wei. Interconnects for superconducting quantum computing. *Journal of Low Temperature Physics*, 189(5-6):273–285, 2017.

[42] R. Lechner, J. Sch"afer, S. Wuensch, and P. Seidel. Mechanical and electrical properties of high-frequency interconnects at cryogenic temperatures. *IEEE Transactions on Applied Superconductivity*, 25(3):1–4, 2015.

[43] C. Janke, S. Woods, and B. Kardynał. Challenges in connector and cable design for low-temperature electronics. *IEEE Transactions on Applied Superconductivity*, 26(3):1–7, 2016.

[44] Austin G Fowler, Matteo Mariantoni, John M Martinis, and Andrew N Cleland. Surface codes: Towards practical large-scale quantum computation. *Physical Review A*, 86(3):032324, 2012.

[45] Julian Kelly, Rami Barends, Austin G Fowler, Anthony Megrant, Evan Jeffrey, Theodore C White, Daniel Sank, Josh Y Mutus, Brooks Campbell, Yu Chen, et al. State preservation by repetitive error detection in a superconducting quantum circuit. *Nature*, 519(7541):66–69, 2015.

[46] Shantanu Debnath, Norbert M Linke, Caroline Figgatt, Kevin A Landsman, Kevin Wright, and Christopher Monroe. Demonstration of a small programmable quantum computer with atomic qubits. *Nature*, 536(7614):63–66, 2016.

[47] Jay M Gambetta, Jerry M Chow, and Matthias Steffen. Building logical qubits in a superconducting quantum computing system, npj quantum information 3, 2. *arXiv preprint arXiv:1510.04375*, 2017.

[48] Markus Reiher, Nathan Wiebe, Krysta M Svore, Dave Wecker, and Matthias Troyer. Elucidating reaction mechanisms on quantum computers. *Proceedings of the National Academy of Sciences*, 114(29):7555–7560, 2017.

[49] David B Tuckerman, Michael C Hamilton, David J Reilly, Rujun Bai, George A Hernandez, John M Hornibrook, John A Sellers, and Charles D Ellis. Flexible superconducting nb transmission lines on thin film polyimide for quantum computing applications. *Superconductor Science and Technology*, 29(8):084007, 2016.

[50] Simin Zou, Yang Cao, Vaibhav Gupta, Bhargav Yelamanchili, John A Sellers, Charles D Ellis, David B Tuckerman, and Michael C Hamilton. High-quality factor superconducting flexible resonators embedded in thin-film polyimide hd-4110. *IEEE Transactions on Applied Superconductivity*, 27(7):1–5, 2017.

[51] Chris S Yung and Brian H Moeckly. Magnesium diboride flexible flat cables for cryogenic electronics. *IEEE transactions on applied superconductivity*, 21(3):107–110, 2010.

[52] AI Harris, M Sieth, JM Lau, SE Church, LA Samoska, and K Cleary. Note: Cryogenic microstripline-on-kapton microwave interconnects. *Review of Scientific Instruments*, 83(8):086105, 2012.

[53] Patrick McGarey, Hamdi Mani, Caleb Wheeler, and Christopher Groppi. A 16-channel flex circuit for cryogenic microwave signal transmission. In *Millimeter, Submillimeter, and Far-Infrared Detectors and Instrumentation for Astronomy VII*, volume 9153, page 91532F. International Society for Optics and Photonics, 2014.

[54] George A Hernandez, Rujun Bai, Yang Cao, John A Sellers, Charles D Ellis, David B Tuckerman, and Michael C Hamilton. Microwave performance of niobium/kapton superconducting flexible cables. *IEEE Transactions on Applied Superconductivity*, 27(4):1–4, 2016.

[55] Emma R Schmidgall, Flavio Griggio, George H Thiel, Sherman E Peek, Bhargav Yelamanchili, Archit Shah, Vaibhav Gupta, John A Sellers, Michael C Hamilton, David B Tuckerman, et al. Reliability characterization of a flexible interconnect for cryogenic and quantum applications. In *2021 IEEE International Reliability Physics Symposium (IRPS)*, pages 1–7. IEEE, 2021.

[56] Vyacheslav Solovyov, Olli-Pentti Saira, Zachary Mendleson, and Ilya Drozdov. Ybco-on-kapton: Material for high-density quantum computer interconnects with ultra-low thermal loss. *IEEE Transactions on Applied Superconductivity*, 31(5):1–5, 2021.

[57] Sherman Peek, Vaibhav Gupta, Bhargav Yelamanchili, Archit Shah, John Sellers, David Tuckerman, and Michael Hamilton. Fabrication and flip-chip assembly processes for cryogenic applications using indium-indium and sac-indium bump connections on flexible interconnects. 04 2021.

[58] Archit Shah, Vaibhav Gupta, Bhargav Yelamanchili, Sherman E Peek, Md Fahim F Chowdhury, Asmaul Smitha Rashid, Uday S Goteti, John A Sellers, David B Tuckerman, and Michael C Hamilton. Towards cable-to-cable connectors for flexible thin-film superconducting transmission lines. *IEEE Transactions on Applied Superconductivity*, 31(5):1–6, 2021.

[59] R. J. Schoelkopf and S. M. Girvin. Wiring up quantum systems. *Nature*, 451:664–669, 2008.

[60] B. Abdo, K. Sliwa, L. Frunzio, and M. Devoret. Low impedance measurement of superconducting resonators. *Applied Physics Letters*, 97(16), 2010.

[61] JR Cost, JO Willis, JD Thompson, and DE Peterson. Fast-neutron irradiation of $YBa_2Cu_3O_x$. *Physical Review B*, 37(4):1563, 1988.

[62] A Wisniewski, M Baran, P Przysłupski, H Szymczak, A Pajaczkowska, B Pytel, and K Pytel. Magnetization studies of $YBa_2Cu_3O_{7-x}$ irradiated by fast neutrons. *Solid state communications*, 65(7):577–580, 1988.

[63] A Umezawa, GW Crabtree, JZ Liu, HW Weber, WK Kwok, LH Nunez, TJ Moran, CH Sowers, and H Claus. Enhanced critical magnetization currents due to fast neutron irradiation in single-crystal $YBa_2Cu_3O_{7-\delta}$. *Physical Review B*, 36(13):7151, 1987.

[64] J Bohandy, J Suter, BF Kim, K Moorjani, and FJ Adrian. Gamma radiation resistance of the high t_c superconductor $YBa_2Cu_3O_{7-\delta}$. *Applied physics letters*, 51(25):2161–2163, 1987.

[65] L Luo, YH Zhang, SH Hu, WH Liu, GL Zhang, and WX Hu. Gamma radiation effects on some properties of YBCO. *Physica C: Superconductivity*, 178(1-3):11–14, 1991.

[66] JA Cooksey, WD Brown, SS Ang, HA Naseem, RK Ulrich, and L West. Gamma-ray and fast neutron radiation effects on thin film superconductors. *IEEE transactions on nuclear science*, 41(6):2521–2524, 1994.

[67] MK Ghosh and KL Mittal. Polyimides: fundamentals and applications marcel dekker. *Inc., New York*, 1996.

[68] EIDPD Nemours. Summary of properties for kapton polyimide films. `http://www.dupont.com/content/dam/assets/products-and-services/membranes-films/assets/DECKapton-summary-of-properties.pdf`. accessed December 2015.

[69] Kaushik A Iyer, Douglas S Mehoke, and Romesh C Batra. Interplanetary dust particle shielding capability of spacecraft multi-layer insulation. In *2014 IEEE Aerospace Conference*, pages 1–14. IEEE, 2014.

[70] Eric L Christiansen and Dana M Lear. Toughened thermal blanket for micrometeoroid and orbital debris protection. *Procedia Engineering*, 103:73–80, 2015.

[71] A Mazzinghi, M Sabbadini, and A Freni. Enhanced RF behavior multi-layer thermal insulation. *Scientific reports*, 8(1):1–10, 2018.

[72] Małgorzata Hołyńska, Adrian Tighe, and Christopher Semprimoschnig. Coatings and thin films for spacecraft thermo-optical and related functional applications. *Advanced Materials Interfaces*, 5(11):1701644, 2018.

[73] Simin Zou, Yang Cao, Vaibhav Gupta, Bhargav Yelamanchili, John A. Sellers, Charles D. Ellis, David B. Tuckerman, and Michael C. Hamilton. High-quality factor superconducting flexible resonators embedded in thin-film polyimide HD-4110. *Applied Superconductivity*, 27(07):1–5, 2017.

[74] Simin Zou, Yang Cao, George Hernandez, Rujun Bai, Vaibhav Gupta, John A. Sellers, Charles D. Ellis, David B. Tuckerman, and Michael C. Hamilton. Embedded niobium using PI-2611 for superconducting flexible cables. *MRS Advances*, 2(41):2199–2204, 2017.

[75] Bhargav Yelamanchili, Vaibhav Gupta, Simin Zou, Robert Christiansen, Max C. Cichon, John A. Sellers, Minseo Park, Masoud Mahjouri-Samani, David B. Tuckerman, and Michael C. Hamilton. Radiation effects on thin flexible superconducting cables. *IEEE Transactions on Applied Superconductivity*, 31(5):1–5, 2021.

[76] Vaibhav Gupta, John A Sellers, Charles D Ellis, Simin Zou, George A Hernandez, Rujun Bai, Yang Cao, David B Tuckerman, and Michael C Hamilton. Preserving niobium superconductivity in thin-film superconducting flexible cables. In *Proc. IMAPS 12th Int. Conf. Exhib. Device Packag.*, pages 002075–002094, 2016.

[77] Vaibhav Gupta, John A Sellers, Charles D Ellis, Bhargav Yelamanchili, Simin Zou, Yang Cao, David B Tuckerman, and Michael C Hamilton. Minimizing film stress and degradation in thin-film Nb superconducting cables. In *Proc. IMAPS 13th Int. Conf. Exhib. Device Packag.*, volume 2017, pages 1–25, 2017.

[78] Rujun Bai. *Superconducting resonators on thin film flexible substrates*. PhD dissertation, Auburn University, 2016.

[79] X-ray mass attenuation coefficients. https://www.nist.gov/pml/x-ray-mass-attenuation-coefficients. accessed January 2021.

[80] John D Cressler and H Alan Mantooth. *Extreme environment electronics*. CRC Press, 2017.

[81] PS Winokur, KG Kerris, and L Harper. Predicting cmos inverter response in nuclear and space environments. *IEEE Transactions on Nuclear Science*, 30(6):4326–4332, 1983.

[82] Paul J Petersan and Steven M Anlage. Measurement of resonant frequency and quality factor of microwave resonators: Comparison of methods. *Journal of applied physics*, 84(6):3392–3402, 1998.

[83] T. M. Antonsen et al. Fabrication of superconducting microwave resonators using si substrates. *IEEE Transactions on Applied Superconductivity*, 7(2):1124–1127, 1997.

[84] G. C. Hilton et al. Characterization of superconducting resonators fabricated on intrinsic silicon wafers. *IEEE Transactions on Applied Superconductivity*, 9(2):1438–1441, 1999.

[85] A. J. Przybysz et al. Microwave measurement of intrinsic si epitaxial material for sub-micron superconducting circuit applications. *IEEE Transactions on Applied Superconductivity*, 12(1):1162–1165, 2002.

[86] D. W. Hess et al. *Clean Surfaces: Their Preparation and Characterization*. Academic Press, 1981.

[87] M. Hatzistergos et al. Rca clean: An effective surface treatment for improving adhesion of electrodeposits to silicon surfaces. *Journal of The Electrochemical Society*, 136(4):1142–1147, 1989.

[88] A. Gupta et al. Gold wire bonding for microelectronics: A review. *Journal of Microelectronics and Electronic Packaging*, 4(3):84–93, 2007.

[89] S. Y. Chou et al. Gold wire bonding process optimization for microelectronic packaging. *Journal of Applied Physics*, 68(7):3791–3799, 1990.

[90] J. Wang et al. Investigation of gold wire bonding for superconducting integrated circuits. *IEEE Transactions on Applied Superconductivity*, 18(2):1862–1865, 2008.

[91] Sebastian Probst, FB Song, Pavel A Bushev, Alexey V Ustinov, and Martin Weides. Efficient and robust analysis of complex scattering data under noise in microwave resonators. *Review of Scientific Instruments*, 86(2):024706, 2015.

[92] Martin A Wolff, Simon Vogel, Lukas Splitthoff, and Carsten Schuck. Superconducting nanowire single-photon detectors integrated with tantalum pentoxide waveguides. *Scientific Reports*, 10(1):1–9, 2020.

[93] SA Peeters, HCM Knoops, WMM Kessels, DC Leitao, and S Calero. Plasma-enhanced atomic layer deposition of superconducting tantalum carbonitride for quantum devices. 2022.

[94] Lili Shi, Tingting Guo, Runfeng Su, Tianyuan Chi, Yifan Sheng, Junliang Jiang, Chunhai Cao, Jingbo Wu, Xuecou Tu, Guozhu Sun, et al. Tantalum microwave resonators with ultra-high intrinsic quality factors. *Applied Physics Letters*, 121(24):242601, 2022.

[95] Carson Koppel, Brandon Wilfong, Allana Iwanicki, Elizabeth Hedrick, Tanya Berry, and Tyrel M McQueen. Machine-guided design of oxidation-resistant superconductors for quantum information applications. *Inorganics*, 11(3):117, 2023.

Appendix A

Psuedo Random Bit Sequence

This chapter contains a MATLAB used for generating the random bits for use in face-to-face connector transient simulations in Chapter 2

```
% Code to generate PRBS data files for use in ADS %
%clear prbsdata seed record
clear all


num = 1; % number of sources
O = 10; % order of PRBS sources ... change this to make length of sequence longer
% 4 is really short, 32 is too long
N = 2^O-1; % length of PRBS sequences
extrazeros = 79; % number of extra zeros to pad between pulses
length = (extrazeros + 1) * N; % total length of pulse sequence with padded zeros


%seed = zeros(1,O-1); % uncomment these two lines to NOT start from a
%random seed
%seed(1,O) = 1; % uncomment these two lines to NOT start from a
%random seed
rng('shuffle') % use the shuffled (more random) version of random
seed = round(rand(1,O)); % comment this line to NOT start from a random seed
prbsdata = zeros(num,length); % initialize the prbs data location
allonesdata = zeros(num,length); % initialize the allones data location
prbsdata(1) = 0 ; % make first one a zero
```

```
allonesdata(1) = 0; % make first one a zero
for ii = 1:N-1
    jj = ii * (extrazeros + 1) + 1; % index to proper location in files for potential 'o
    [prbsdata(jj),seed] = prbs(0,1,seed); % determine if a 'one' should be in this locat
    allonesdata(jj) = 1; % for all ones data case, make this position a one
    %if prbsdata(jj) == 1 % if loop for troubleshooting
        %record(ii) = jj;
    %else
    %end
    %seed
end

allonesdatastr = strrep(num2str(allonesdata),' ',''); % get rid of the extra spaces in t
prbsdatastr = strrep(num2str(prbsdata),' ',''); % get rid of the extra spaces in the str

basename='prbsdatain_';
basenameall='prbsdataallin_';
k = 0;
filename=[basename,num2str(0),'_',num2str(k),'.txt']; % first number in filename is orde
filenameall=[basenameall,num2str(0),'.txt'];
stoploop = 0;
dl = strcat('''%',num2str(length),'s\n''');
while ~stoploop
    if ~isfile(fullfile(cd, filename))
        stoploop = 1;
    else
        k = k + 1;
```

```
        filename=[basename,num2str(0),'_',num2str(k),'.txt'];
    end
    if ~isfile(fullfile(cd, filenameall))
        fileIDall = fopen(filenameall,'w');
        fprintf(fileIDall,'%c\n','!');
        fprintf(fileIDall,'%20s\n','! PRBS all ones data'); % this writes to the file th
        fprintf(fileIDall,dl,allonesdatastr);
        fclose(fileIDall);
    else
    end
end

fileID = fopen(filename,'w');
fprintf(fileID,'%c\n','!');
fprintf(fileID,'%11s\n','! PRBS data'); % this writes to the PRBS data file
fprintf(fileID,dl,prbsdatastr); % this is still causing there to be single quotes around
fclose(fileID);
```